Safe Flutter Determination for Wings Undergoing Large Deflections

Experimental Application of the Parametric Flutter Margin Method to a Highly Flexible Wing

Stefan de Boer

Technische Universiteit Delft

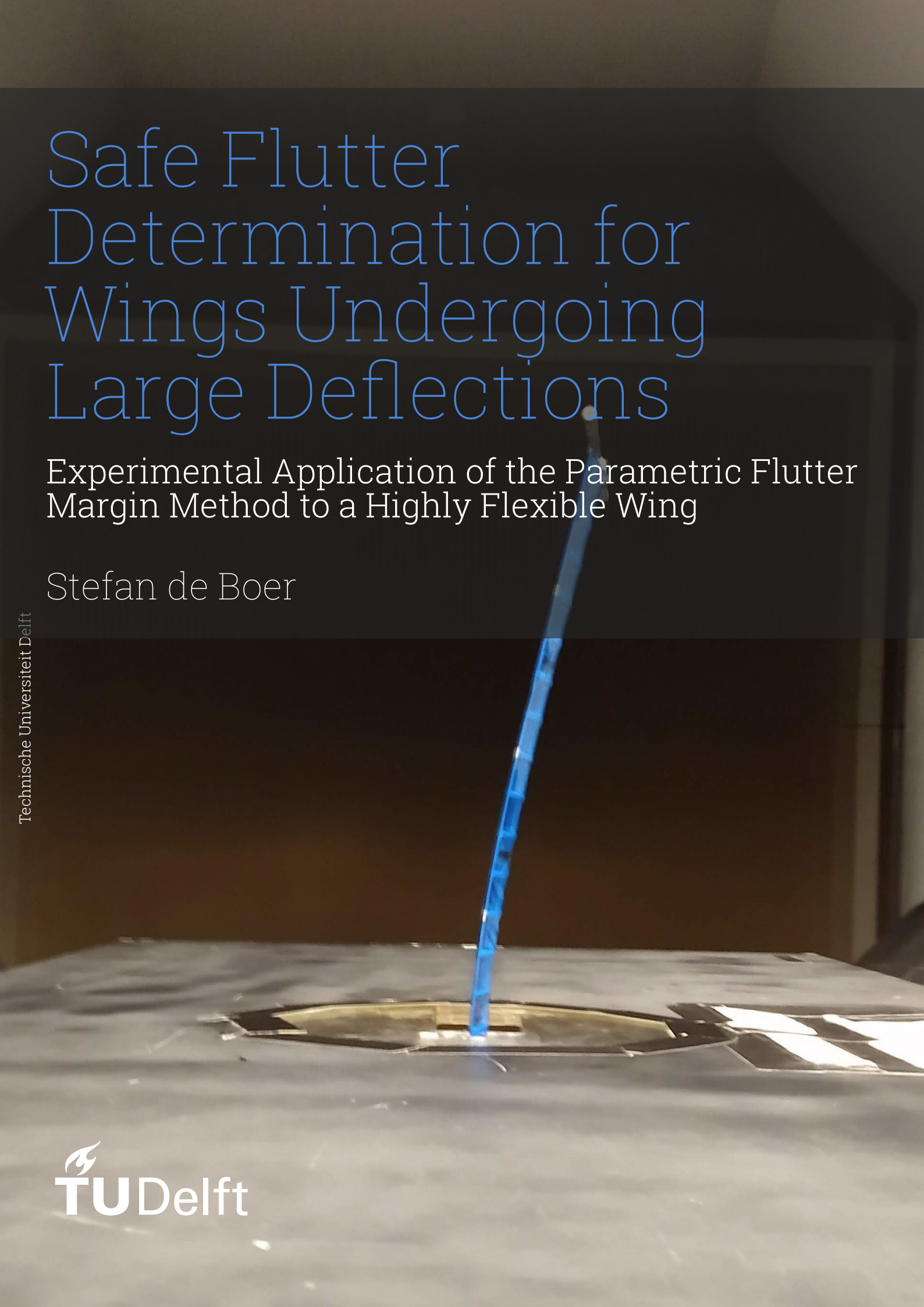

TU Delft

Safe Flutter Determination for Wings Undergoing Large Deflections

Experimental Application of the Parametric Flutter Margin Method to a Highly Flexible Wing

by

Stefan de Boer

to obtain the degree of Master of Science
at the Delft University of Technology,
to be defended publicly on Thursday January 12, 2023 at 12:30.

Student number:	4652673	
Project duration:	February 2022 – January 2023	
Thesis committee:	Dr.ir. R. De Breuker	TU Delft ASM, Chair
	Dr. J. Sodja,	TU Delft ASM, Supervisor
	Prof. Em. M. Karpel,	Technion — Israel Institute of Technology, Supervisor
	Dr.-Ing. S.G.P. Castro	TU Delft ASM, Examiner
	Dr. A. Sciacchitano	TU Delft FPT, Examiner

TU Delft

Preface

The document you're about to read represents my work performed as the last part of my MSc in Aerospace Engineering, which I hope will be a source of inspiration for future work related to aeroelasticity and flutter detection.

First of all, I'm grateful for the opportunity given by my supervisors Jurij Sodja and Moti Karpel to work on a research subject which is at the cutting edge of technology. Even though the first experimental application of the MIMO PFM method was challenging at times as it encompassed numerical modelling, manufacturing and testing of the experimental method, resulting in a truly all-encompassing project. I can highly recommend doing such a thesis to all future students.

Of course, without the help of others, this thesis could not have been completed. First, I would like to thank Jurij for his daily supervision, time and enthusiasm, and I'm looking forward to working with you and Roeland in the near future. Secondly, I would like to thank Moti for his patience, explanations about the PFM method, and research ideas within the field of aeroelasticity itself. Just the ideas he presented during the meetings provided enough research topics for at least the next 30 years. Furthermore, I would like to thank my committee members, Roeland De Breuker, Saullo Castro and Andrea Sciacchitano for taking the time to read my thesis, and I'm looking forward to your questions.

Finally, I would like to thank my parents and brother, Adam, for their continued support throughout my time in Delft and with all activities, I decide to undertake.

Stefan de Boer
Delft, December 2022

Abstract

The flight tests which are part of the certification procedure that prove that no flutter occurs within the flight envelope are fraught with risk. To reduce the risk, numerous numerical analyses, wind tunnel and ground tests are performed, which together with the flight tests result in a long and costly test programme.

To reduce the risks associated with flutter flight testing, a new flutter test version of the Parametric Flutter Margin (PFM) method, specifically applied to wings undergoing large deflections is presented. The PFM method adds a stabilising parameter, such as a stabilising mass, to the model such that the flutter velocity is increased. By exciting the stabilising mass in one of the primary (i.e., x, y and z) directions while simultaneously measuring the response in these directions and repeating the excitation in other directions, the flutter margins that are associated with the original model can be determined. To demonstrate the method a wind tunnel test campaign was performed at TU Delft using the Delft Pazy Wing which can exhibit large nonlinear deflection. The wing was equipped with a flutter pod consisting of a shaker and stabilising mass that was placed at the mid-span position at the leading edge of the wing.

During the test campaign, three test series were performed. The first identified the flutter boundary through direct flutter tests, with the flutter onset and offset velocities being determined by actually hitting flutter that turned into an LCO. The second and third test series were the PFM measurements, where both SISO and MIMO PFM were applied to obtain the nominal flutter boundaries without actually hitting flutter. The different PFM results showed a maximum difference of 4.4 % between each other at an angle of attack, α, of 6°, with the difference found to be minimal at $\alpha = 0°$ and increasing with increasing angle of attack, which was as expected.

Compared to the directly measured flutter tests, the MIMO PFM results identified a flutter velocity of 4.8 % lower than the directly measured flutter offset velocity at an angle of attack of 4°, and the SISO PFM results identified the flutter velocity to be 8.2 % lower than the offset velocity at 4° angle of attack. The PFM-identified flutter frequencies showed a difference of less than 2 % compared to the direct flutter test, with the difference in identified flutter frequency between the SISO and MIMO PFM reaching a maximum of 2 %, which was also increasing with increasing angle of attack.

However, even with the successful application, several research areas remain open, and several points of improvement for the performed test campaign have been found. Although besides the points of improvement, the acquired data shows the potential of the PFM method for performing safer, shorter and consequently cheaper flight tests for the certification procedure of new aircraft configurations.

Contents

List of Figures

List of Tables

Nomenclature

Abbreviations

AoA	Angle of Attack
ARMA	Autoregressive Moving Average
DLM	Doublet-Lattice Method
DOF	Degree of Freedom
FM	Flutter Margin
FRF	Frequency Response Function
GVT	Ground Vibration Test
LCO	Limit Cycle Oscillation
LE	Leading Edge
MAC	Modal Assurance Criterion
MAC_{ODS}	Modal Assurance Criterion of the Operational Deflected Shape
MIMO	Multiple Input Multiple Output
ODS	Operational Deflected Shape
PCO	Phase Cross-Over
PFM	Parametric Flutter Margin
SISO	Single Input Single Output
TE	Trailing Edge

Greek Symbols

α	Angle of attack	°
Δp_f	Stabilising mass needed to bring Nominal configuration to flutter boundary	gram
λ	Eigenvalue	
λ_f	Eigenvalue at flutter boundary	
μ	Stabilising to moving mass ratio	
ω	Frequency	Hz
ω_{pco}	Phase crossover frequency	Hz
ω_f	Flutter/Limit-cycle oscillation frequency	Hz
$\Phi(i\omega)$	Phase	°, rad

Roman Symbols

$[A(i\omega)]$	Aeroelastic system matrix

$a_{s,c}$	Averaged moving mass acceleration	m/s^2
$a_{\text{mv}}, \{a_{\text{mv}}\}$	Acceleration of shaking mass	m/s^2
$a_{\text{st}}, \{a_{\text{st}}\}$	Acceleration (Stabilising) stationary mass	m/s^2
$\{B_f\}$	Flutter margin input distribution vector	
$[B_f]$	Flutter margin input distribution matrix	
$[C_f\,(i\omega)]$	Flutter margin row-plant output matrix	
$\{C_f\,(i\omega)\}$	Flutter margin row-plant output vector	
c_l	2D lift coefficient	
F	Force	N
F_{ip}	Averaged impedance head force	N
F_{ij}	Force correction factor	
$\{f(\{x\})\}$	Discontinuous function	
f	Frequency	Hz
$G\,(i\omega)$	Gain	
g	Aeroelastic damping coefficient	
m_{mv}	Mass of shaking mass	gram
m_{st}	Mass of (Stabilising) stationary mass	gram
P_f	Stabilising parameter	
p_f	Stabilising mass	gram
Q_{ij}	Mass corrected acceleration transfer function	
S	Span	m
t	Thickness	mm
$[T\,(i\omega)]$	Parametric flutter margin multiple-input/multiple output matrix	
$T\,(i\omega)$	Parametric flutter margin transfer function	
T_{ij}	PFM transfer function	
$u_f, \{u_f\}$	Excitation input	
V	Velocity	m/s
$\{x\}$	State vector	
$\{x(i\omega)\}$	Vector of DOFs	
$y_f, \{y_f\}$	Response stabilising parameter	

Subscripts

L	Local coordinate system

1

Introduction

As part of the certification procedure, flight testing which proves that the flight envelope of the aircraft is flutter free is fraught with risk [1], [2]. During the flight tests, the flutter boundary is carefully approached up until the point that the damping coefficient reaches the 3 % threshold, or that the flight envelope boundary is reached [3]. However, it is in some cases possible for the damping to decrease rapidly, which can lead to a sudden explosive flutter. Therefore, numerous numerical analyses, wind tunnel and ground tests are performed to make sure that the test aircraft is not accidentally brought too close to the flutter boundary.

To reduce the cost and dangers of opening the flight envelope, the presented research presents a new flutter test version of the Parametric Flutter Margin (PFM) method, which allows for the safe and more time-effective opening of the flight envelope without actually experiencing flutter itself.

Nevertheless, before the PFM method is addressed and the experimental results are presented, the following sections within this chapter introduce the concepts of aeroelasticity and flutter, after which a state-of-the-art review of flutter flight testing methods is presented. This is followed by the research objectives and challenges addressed by the presented research. To conclude this chapter, the document outline is presented

1.1. Aeroelasticity

The field of aeroelasticity is highly relevant and needs to be considered such that the desired performance and operation characteristics, as well as the safety of aircraft designs, are ensured. It studies the interaction between the structure and the surrounding airflow, with a popular representation of the interactions being the Collar's triangle [4], shown in Figure 1.1.

Besides the interaction of forces, Collar's triangle also describes how the different types of static and dynamic aeroelasticity phenomena are connected to those forces. The three forces within aeroelasticity described by Collar's triangle are the aerodynamic (A), elastic (E) and interial (I) forces. The aerodynamic forces are caused by the interaction of the structure with the flow, with the inertial forces being related to the mass and acceleration of the object. Finally, the elastic forces come from the structural properties and appear when the studied object is deformed.

As can be seen in Collar's triangle, flutter (F) involves all different forces, and as can be seen in the following section, it is a dynamic aeroelastic phenomenon that can lead to the exceedance of the design limits leading to failure. Furthermore, as shown in many recent works, the control-system discipline may be added as a major participant in the diagram.

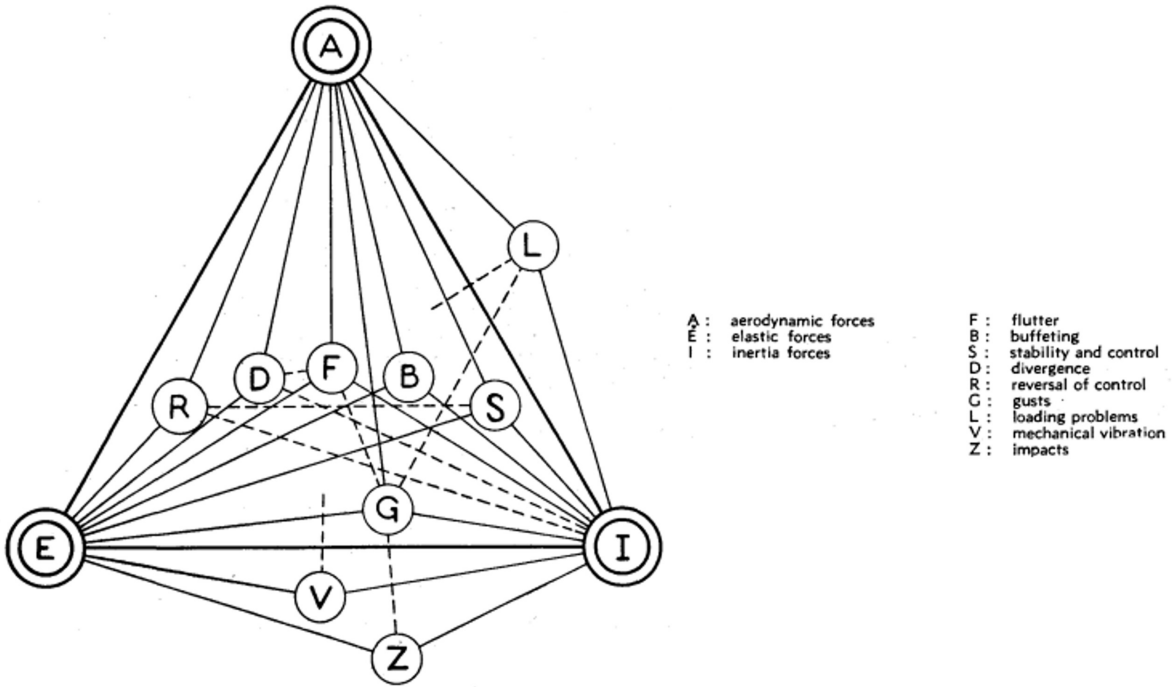

Figure 1.1: Collar's triangle, depiction of load interactions in aeroelasticity. Retrieved from [4]

1.2. Flutter

As can be seen in Collar's triangle, flutter is a dynamic aeroelastic phenomenon that is created by the interaction between the structural dynamics and the aerodynamic forces interacting with the structure and occurs when the structure can extract energy from the flow to which it is subjected. Below the flutter boundary, the aeroelastic system will dampen the oscillations caused by any external excitation, whereas the aeroelastic system is neutrally stable at the flutter boundary. The flutter boundary is governed by multiple flight and structural conditions. However, the flight conditions that influence the flutter boundary are mainly influenced by the velocity of the flow through which the structure is moving [3].

1.2.1. Flutter Types

Above the flutter boundary, two types of flutter exist [3]. The first type is linear flutter, in which an infinitesimally small excitation leads to a harmonic response in which the amplitude grows to infinity, which causes the forces on the structure to exceed the design values leading to the occurrence of structural failure.

The second type is nonlinear flutter in which the amplitude of the harmonic response to excitation is bounded by a stabilising non-linear structural or aerodynamic property [5], with the limited harmonic response leading to a so-called limit cycle oscillation (LCO) [6].

The mathematical representation of the LCO behaviour present within a test vehicle is difficult, as rarely all nonlinearities present within the test vehicle are known beforehand and implemented in a numerical model [6]. The nonlinearity present within the test vehicle is more often than not unanticipated.

Therefore, the exact LCO behaviour can only be detected during flight testing or wind tunnel tests. The occurrence of an LCO during testing can be beneficial in some cases, as instead of experiencing linear flutter, which can lead to the destruction of the test model of the flight vehicle, a nondestructive LCO is experienced [6]. This LCO needs to have an oscillation amplitude that is small enough such that the maximum allowable structural loads are not exceeded. As can be seen in Figure 1.2, a supercritical LCO, where the LCO amplitude increases with an increasing velocity above the flutter speed is beneficial for the safety of the test object, as the amplitude of the flutter is limited [6]. Also shown in Figure 1.2 is the subcritical LCO, and just as with the supercritical LCO, it starts with a Hopf bifurcation, which is

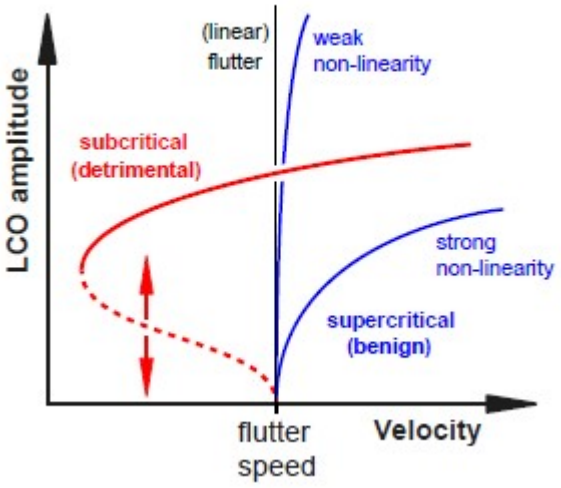

Figure 1.2: Types of LCOs as described by Dowell et al. [7]. Obtained from van Rooij [8]

an intersection between a periodic and static solution accompanied by a change in the stability of the fixed point [5], at the flutter speed. The subcritical LCO shows both a stable and unstable (indicated by the dashed lines) branch that exists below the flutter boundary of the underlying linear system.

The behaviour of the subcritical LCO will depend on the nonlinearities present within the aeroelastic system. The initial conditions provided to the aeroelastic system will cause the oscillation to grow to a stable LCO, or decay to an oscillation-free condition. In case the initial conditions provide an excitation amplitude smaller than the amplitude of the unstable LCO branch, the system will return to an oscillation-free condition, with the amplitude of the harmonic oscillation growing to the stable LCO branch if the initial excitation has an amplitude greater than the unstable branch [7].

As can be seen in Figure 1.2, an increasing initial amplitude is necessary for the subcritical LCO to become stable with decreasing velocity. It can also be seen that the subcritical LCO branch experiences fold bifurcation, which in this case is supercritical fold bifurcation. Fold bifurcation is the point when the local slope of the LCO amplitude versus velocity goes to infinity, after which the LCO branch changes direction. Even though Figure 1.2 only shows fold bifurcation for a subcritical LCO branch, fold bifurcation can also occur for a supercritical LCO branch, as only the direction of the LCO branch needs to change for bifurcation to occur [5].

1.2.2. Influences on LCOs

For LCOs to occur, the amplitude of the harmonic response needs to be bounded. However, it is possible for unstable LCOs to exist, as the magnitude of the bounded amplitude can change dependent on nonlinearities present within the aeroelastic system. As stated previously, this can be done through either a structural or aerodynamic nonlinearity present within the aeroelastic system.

Examples of structural nonlinearities are hardening and softening stiffness within a structure. A hardening stiffness is a nonlinearity whose stiffness increases with increasing deformation, which causes the frequency of the oscillation to increase with the oscillation amplitude [5], and therefore, the instantaneous LCO frequency is dependent on the instantaneous LCO amplitude.

The softening stiffness nonlinearity is a nonlinearity where the stiffness is decreasing with increasing deformation, with the nonlinear responses of aeroelastic systems containing a softening nonlinearity being able to be classified into two categories. In the first category, the nonlinear responses take the form of divergent flutter far below the linear flutter boundary [9]. This response is dependent on the initial conditions to which the aeroelastic system is subjected. The second category allows for the existence of stable, semistable and unstable LCOs at or above the linear flutter boundary [5], [9]. Wei and Mottershead [9] found that the behaviour of aeroelastic systems containing a softening nonlinearity

can be described by Hopf, fold, pitchfork and period-doubling bifurcations, with the behaviour strongly depending on the initial conditions. Furthermore, it was also found that regions, where the predicted stable LCOs can be free from the destabilising effect of the softening nonlinearity dependent on the wing characteristics, can occur [9].

Another form of structural nonlinearity is a discontinuous nonlinearity such as freeplay. Within a discontinuous nonlinearity the stiffness of the aeroelastic system can be described as a discontinuous function $\{f(\{x\})\}$ [5].

$$\{f(\{x\})\} = \begin{cases} \{f_0(\{x\})\} & \{x\} \in \Delta_0 \\ \{f_1(\{x\})\} & \{x\} \in \Delta_2 \\ \quad \vdots & \\ \{f_n(\{x\})\} & \{x\} \in \Delta_n \end{cases} \tag{1.1}$$

Where $\{x\}$ is a n x 1 state vector [5]. In the case of freeplay, $\{f(\{x\})\}$ can be written as a piecewise linear stiffness, where the stiffness within the freeplay zone is equal to zero. The LCO caused by freeplay can have a significantly larger amplitude than the freeplay zone [10], with the aeroelastic system containing freeplay having multiple flutter velocities because it can be described using an underlying and overlying system. The overlying linear system is the aeroelastic system is the nominal system without freeplay, whereas the underlying system contains the freeplay causing the lower flutter velocity because of the lower stiffness [5].

Besides the structural nonlinearities causing the LCO to occur, aerodynamic nonlinearities can also limit the amplitude growth of the flutter, causing an LCO. Depending on the flow conditions different types of aerodynamic nonlinearities exist [5]. Weak aerodynamic nonlinearities are present within an attached flow because of the motion of the wake and the presence of trigonometric functions of the angle of attack, with an example of the trigonometric functions for a 2D flat plate aerofoil in an incompressible, inviscid flow being [5]

$$c_l = 2\pi \sin \alpha \tag{1.2}$$

where the 2D lift coefficient is given by c_l and α is the angle of attack. Besides the weak aerodynamic nonlinearities, strong aerodynamic nonlinearities also exist within the flow and are caused by flow separation, which can either be periodic or permanent [5].

For low-speed subsonic flows, strong aerodynamic nonlinearity occurs in separated flow regions. The fact that the flow separates from the body, due to either stall or vortex shedding, limits the amplitude growth and therefore causes an LCO. The LCO continues because of the reattachment of the flow to the structure, which means that once more the structure can extract energy from the flow [5].

Several aerodynamic nonlinearities also exist for high-speed flows. However, as the presented research focuses on low-speed subsonic flows, these nonlinearities are outside of the scope of the work. Therefore, for more information on high-speed aerodynamic nonlinearities, readers are referred to *Introduction to Nonlinear Aeroelasticity* by Dimitriadis [5].

A final type of nonlinearity that can influence the LCO behaviour of an aeroelastic system is geometric nonlinearity. Geometric nonlinearity is one of the most common forms of nonlinearity to appear within structures [5], with an example being large deflections. Looking at the results obtained by Tang and Dowell [11], in which the first and second bending modes have a lower frequency than the first torsion mode, it can be stated that the flutter velocity and flutter frequency decrease when the tip deflection increases. The reduction in flutter velocity is because of the geometric non-linearity caused by the tip deflection. When the wing experiences a tip deflection, the frequency of the first torsion mode decreases, whereas the bending frequencies remain close to the undeformed values [11]–[13]. From the results from Tang and Dowell [11], it can be stated that the larger the tip deflection, the lower the first torsion mode frequency becomes. Because of the frequency reduction of the first torsion mode, the interaction between the first torsion mode and the bending modes happens at a lower velocity, which in turn leads to a lower flutter velocity. The same reduction of the frequency of the first torsion mode also leads to the reduction of the flutter frequency for larger deflections [11].

With the analyses by Tang and Dowell [11] and Patil et al. [12], [13], having been performed on a flexible wing, it is expected that the effects on the flutter velocity, flutter frequency, and reduction of the first torsion mode frequency will also be present within a highly flexible wing as long as the first or

second bending modes have a lower frequency than the first torsion mode. Therefore, it is expected that when a deflection is applied to the wing by changing the angle of attack, the flutter speed is reduced in comparison with the condition at a smaller deflection.

It is expected that the flutter velocity of the wing will continue to decrease with increasing deflection up to a point where the wing will either stall or immediately experience divergence. Conversely, the increase in deflection can cause the first torsion frequency to become lower than the frequency of the second bending mode. This leads to the occurrence of a hump flutter mechanism, where the flutter mechanism starts as a second bending – first torsion flutter mechanism that stops at increasing velocity, which in turn means a larger deflection. By further increasing the deflection, a different flutter mechanism, the first bending – first torsion flutter mechanism, is formed resulting in a jump in flutter velocity [11]–[13].

1.3. State-of-the-Art

With the principles of flutter and the specifics related to highly flexible wings undergoing large deflections discussed, the state-of-the-art in flutter boundary prediction and detection will be reviewed.

To be able to predict the flutter boundary during flight tests, several different data-analysis methods exist, such as the Zimmerman-Weissenburger flutter margin [14], damping extrapolation [15], the envelope function [16] and the Autoregressive Moving Average (ARMA) method [17]. All of these methods use the data obtained at velocities below the flutter speed to extrapolate the flutter boundary, which in turn leads to long, risky and expensive tests [18].

On the contrary, the numerical Parametric Flutter Margin (PFM) method developed by Roizner and Karpel [19], [20] formed a basis for an experimental method that safely determines the flutter condition by stabilising the system and analysing the frequency response functions (FRFs) of the stabilising element with respect to a co-located excitation force. A flutter margin (FM) with respect to the stabilising parameter is determined, based on which the flutter velocity can be determined through interpolation.

Two versions of the PFM method exist, single-input single-output (SISO) PFM and multiple-input multiple-output (MIMO) PFM. SISO PFM looks at the variation of the flutter characteristics with respect to a single stabilising parameter P_f [20], with the requirement being that the effects of P_f can be formulated as a SISO feedback loop, leading to an incremental system matrix of rank-1, which means that the effect of P_f can only be analysed in a single direction whilst ignoring coupling effects. The MIMO PFM method removes the SISO PFM constraint by expanding the rank-1 augmented system equation of motion to include MIMO feedback, allowing for the representation of the effect of the stabilising parameter in an incremental system matrix of any rank [21].

The PFM method has been demonstrated on aeroelastic systems both numerically and experimentally. The numerical results obtained using the PFM method were compared to the results obtained using the MSC Nastran p-k and ZAERO g methods. The results showed that the SISO PFM results were practically identical to the conventional flutter determination methods for linear aeroelastic systems. The non-linear numerical flutter results showed that the LCO amplitudes calculated using the SISO PFM method are up to 7 % larger, however, this was considered acceptable for design studies [19], [20].

The first experimental application of PFM was performed by Sodja et al. on a 2 degree-of-freedom (DOF) typical section [18], who showed that the experimental and numerical SISO PFM method has very good to excellent agreement with the direct flutter test, as differences varying from 1 % to 6 % were found. Roizner et al. applied PFM to a flexible cantilever wing with an integrated stabilising mass [22]. The results showed that the differences in the flutter velocity between the experimental PFM and numerical methods were less than 1 % and that the flutter modes and frequencies found using the PFM method were comparable with the numerical methods used in industry. The most recent experimental application of the PFM method to an aeroelastic system was performed by Karpel et al. [23]. The excitation device and stabilising parameter were integrated in this wind-tunnel experiment into a single flutter pod that consists of a shaker used to provide the excitation force, two accelerometers and a stabilising mass. The obtained result demonstrated a successful application of a shaker during the PFM tests, as a difference of 6.4 % with the numerical models was found. Since, as explained below, the PFM test positively indicates the nominal flutter boundary, the difference is more due to

modelling errors than due to testing errors.

1.4. Research Objective

As presented previously, the PFM method has been applied numerically, and experimentally to both linear and nonlinear aeroelastic systems. However, as an experimental flutter detection method, PFM has only been applied in SISO form. Using a stabilising mass, the SISO approach is limited to cases where the effect of the added mass on flutter is significant only in one direction, normal to the lifting surface in the previously tested cases. Therefore, to be able to expand the understanding and application of PFM, the main objective of the presented work is to

> *Safely determine the flutter boundary of a wing undergoing large static deflections by the use of the PFM method.*

This leads to the experimental application of MIMO PFM, as the effects of the stabilising mass added to a nonlinear aeroelastic system undergoing large aeroelastic deflections are significant in both the out-of-plane and the fore-and-aft directions, because of the coupling of the out-of-plane torsion mode with the fore-and-aft motion of the wing.

To achieve the stated objective, several challenges are addressed by this research. First of all, two types of nonlinearities are considered. They are a geometric nonlinearity because of the large static deflections, and an aerodynamic nonlinearity caused by the stall of the wing. Both these nonlinearities cause the occurrence of a limit cycle oscillation (LCO) that is formed by the unconventional second bending-first torsion flutter mechanism. The stall of the wing governs the occurrence of the LCO within the wing caused by flow separation. The geometric nonlinearity causes a reduction in flutter velocity with increasing angle of attack.

Because of the occurrence of an LCO, the question arises what the flutter boundary of such a nonlinear aeroelastic system is, as the wing can experience both subcritical Hopf bifurcation and fold bifurcation throughout the LCO amplitude range. Finally, the full nonlinear flutter response is measured to capture the effect of the large deformations on the flutter mode.

Furthermore, by achieving the research objective, this thesis contributes to the state-of-the-art of safe flutter determination through the extension of the PFM method to a nonlinear aeroelastic problem by applying the MIMO PFM method to a highly flexible wing undergoing large aeroelastic deflections. This application of PFM allows for the experimental investigation of stability boundary with respect to velocity and angle of attack and the experimental identification of LCO parameters.

1.5. Structure

To be able to present challenges and contributions to the state-of-the-art, the rest of the thesis has the following structure. First, the SISO PFM method and the extension to MIMO PFM are presented in chapter 2, after which the numerical model used to design the PFM experiment is shown in chapter 3. chapter 4 presents the steps taken to design the experiment and also shows the used experimental setup, after which the required data analysis is presented in chapter 5. This is followed by chapter 6 in which the experimental flutter results are presented. Finally, concluding remarks are given in chapter 7.

2

Parametric Flutter Margin Method

The formulation of the PFM method that has been implemented in this work for the identification of the flutter-onset boundary of a clamped highly flexible wing under large initial deflections is presented in this section. First, the SISO PFM method is presented in Section 2.1, after which the modifications necessary to extend the PFM method to MIMO PFM are presented in Section 2.2. Finally, Section 2.3 presents several methods available to excite the stabilising parameter and shows the selected excitation method.

2.1. SISO PFM

The formulation of the PFM method starts with the homogeneous aeroelastic equation given by

$$[A(i\omega)]\{x(i\omega)\} = \{0\} \tag{2.1}$$

To be able to apply the SISO-PFM method, the stabilising parameter, P_f, must be such that the incremental system matrix can be expressed as [19]

$$[\Delta A] = P_f\{B_f\}\{C_f(i\omega)\}^{\mathsf{T}} \tag{2.2}$$

with the constraint that the effect of the stabilising parameter can be removed using a SISO control feedback loop, leading to an incremental system matrix shown in equation (2.2) of rank-1. Because of this constraint, the effect of P_f can only be analysed in a single direction. Therefore, the augmented aeroelastic equation becomes

$$\begin{aligned}[A(i\omega) + P_f\{B_f\}\{C_f(i\omega)\}^{\mathsf{T}}]\{x(i\omega)\} &= \{B_f\}u_f(i\omega)\\ y_f(i\omega) &= \{C_f(i\omega)\}^{\mathsf{T}}\{x(i\omega)\}\end{aligned} \tag{2.3}$$

With the vectors $\{B_f\}$ and $\{C_f(i\omega)\}$ depending on the characteristics of the stabilising parameter, and u_f and y_f being the scalar input and output variables of the augmented aeroelastic equation. Using any $u_f(i\omega)$ that has a significant content over the frequency range of interest, equation (2.3) can be solved for $\{x(i\omega)\}$ and $y_f(i\omega)$.

At the flutter boundary, the input-output relation needs to satisfy

$$u_f(i\omega_f) = P_f y_f(i\omega_f) \tag{2.4}$$

such that the effect of P_f can be removed using a SISO feedback loop, with ω_f being the flutter frequency. Substituting equation (2.4) into equation (2.3), it can be shown that at the flutter boundary of the nominal system the effect of the stabilising parameter is removed by closing the SISO feedback loop, as the substitution removes the $P_f\{B_f\}\{C_f(i\omega)\}$ term which was added to form equation (2.3). Therefore, the flight conditions and excitation input that satisfy equation (2.4) indicate flutter. The resulting $\{x_f(i\omega)\}$ found using equation (2.3) is the complex flutter mode, as it is also a non-trivial solution to equation (2.1) [19], [20].

The conditions at which equation (2.4) is satisfied are determined by evaluating the following transfer function at different frequencies at selected velocities.

$$T\left(i\omega\right) = \frac{P_f y_f(i\omega)}{u_f(i\omega)} \tag{2.5}$$

Which can be expressed as gain and phase variations with frequency using the following equations [19], [20].

$$\begin{aligned} G\left(\omega\right) &= \left| \frac{P_f y_f(i\omega)}{u_f(i\omega)} \right| \\ \Phi\left(\omega\right) &= \angle \frac{P_f y_f(i\omega)}{u_f(i\omega)} \text{rad} \end{aligned} \tag{2.6}$$

Using the phase cross-over (PCO) frequencies (ω_{pco}), found at $\Phi\left(\omega_{\text{pco}}\right) = 0$, and the corresponding gain ($G\left(\omega_{\text{pco}}\right)$) the stability of the aeroelastic system can be determined. The nominal system will be stable, if $G\left(\omega_{\text{pco}}\right) < 1$, however, when $G\left(\omega_{\text{pco}}\right) > 1$ the nominal system will experience flutter [20]. Determining ω_{pco} and gain for multiple velocities, the point where $G\left(\omega_{\text{pco}}\right) = 1$, which is the flutter boundary, can be found. The corresponding ω_{pco} indicates the flutter frequency of the aeroelastic system.

2.2. MIMO PFM

As stated above, the SISO PFM method places a constraint on P_f that its effects can be removed using a SISO feedback loop, limiting the incremental system matrix to rank-1, which means that the effect of P_f can only be analysed in a single direction. In cases where the effect of P_f needs to be analysed in multiple directions, the rank-1 limitation of the representation of the stabilising parameter needs to be removed, with the removal of the rank-1 limitation leading to the MIMO PFM method.

A specific example of the requirement of the removal of the rank-1 limitation is presented in this research as the modes that form the flutter mechanism will have a significant motion at the added mass point in both the normal and fore-and-aft directions (local z and x) with the local inertial effects in the spanwise and rotational directions still negligible, because of the large deflections experienced by the wing.

To be able to remove the rank-1 limitation, the SISO PFM method shown in equation (2.3) needs to be adapted to allow for a MIMO stabilising parameter. Following the steps presented in [21], the SISO PFM equation, shown in equation (2.3), is adapted to the following MIMO form.

$$\begin{aligned} \left[A(i\omega) + P_f\left[B_f\right]\left[C_f(i\omega)\right]\right]\left\{x(i\omega)\right\} &= \left[B_f\right]\left\{u_f(i\omega)\right\} \\ \left\{y_f(i\omega)\right\} &= \left[C_f(i\omega)\right]\left\{x(i\omega)\right\} \end{aligned} \tag{2.7}$$

Where $\{u_f\}$ and $\{y_f\}$ are now the input and output vectors, the $[B_f]$ and $[C_f(i\omega)]$ matrices are now able to be of any rank, up to the smaller number of variables in $\{y_f\}$ or $\{u_f\}$, leading to the ability to rewrite equation (2.7) to

$$\left\{y_f\right\} = \left[T(i\omega)\right]\left\{u_f\right\} \tag{2.8}$$

with $\left[T(i\omega)\right] = \left[C_f(i\omega)\right]\left[A\left(i\omega, U\right) + P_f\left[B_f(i\omega)\right]\left[C_f(i\omega)\right]\right]^{-1}\left[B_f(i\omega)\right]$ being the transfer function matrix. At the flutter boundary, the input-output relation now needs to satisfy

$$\left\{u_f(i\omega)\right\} = P_f\left\{y_f(i\omega)\right\} \tag{2.9}$$

Substituting equation (2.9) into equation (2.8) and replacing the real-valued P_f used in the right side of equation (2.9) with the complex valued λ^{-1}, the following eigenvalue problem is created.

$$\left[T(i\omega)\right]\left\{u_f(i\omega)\right\} = \lambda\left\{u_f(i\omega)\right\} \tag{2.10}$$

Solving for the eigenvalues of equation (2.10) for every frequency and velocity, the flutter boundary can be found at the flight conditions for which the eigenvalue is real and satisfies [21]

$$\lambda_f = \frac{1}{P_f} \tag{2.11}$$

Using the eigenvalues and the known stabilising parameter, the transfer functions can be converted into gain and phase using the following equations [24].

$$\begin{aligned} G(\omega) &= \left| \frac{\lambda_i(i\omega)}{P_f} \right| \\ \Phi(\omega) &= \angle \frac{\lambda_i(i\omega)}{P_f} \text{rad} \end{aligned} \tag{2.12}$$

To be able to determine the flutter margin, the $[T(i\omega)]$ matrix needs to be created for every velocity and every frequency from the measured FRFs, and its creation requires multiple steps. By exciting the stabilising parameter in one of the primary (i.e., x, y or z) directions and measuring the response of the stabilising parameter in all these directions, one column of the $[T(i\omega)]$ matrix, can be created.

After the $[T(i\omega)]$ matrix has been created, the eigenvalue λ in equation (2.10) needs to be found. The process of creating the $[T(i\omega)]$ matrix and finding the corresponding λ needs to be repeated for every measured frequency within a single velocity, and is repeated for every velocity. Using the λ's found for all velocities and frequencies, the interpolated λ which satisfies equation (2.11) and $\lambda \in \mathbb{R}$ needs to be found, which is the eigenvalue at the flutter boundary λ_f. The velocity corresponding to λ_f, therefore, indicates the flutter boundary, with the associated eigenvector being the flutter mode at the location of the stabilising parameter. Using the eigenvector $\{u_f\}$ at the flutter velocity and flutter frequency, and the numerically known matrices $[A(i\omega)]$, $[B_f]$ and $[C_f]$, equation (2.7) can be solved for $\{x(i\omega_f)\}$, which represent the full flutter mode of the aeroelastic system.

2.3. Excitation of the Stabilising Parameter

As part of the application of the PFM method, the aeroelastic system needs to be excited to be able to measure the FRFs and search for the flutter condition. The previous experiments used a mass as a stabilising parameter which was excited in different ways. The experiment performed by Sodja et al. [18] used a modal hammer to provide an impulsive force to the stabilising mass. The application of PFM on a cantilever wing by Roizner et al. [22] used a string with an external weight attached. The input was provided by cutting the string, and from the known mass of the external weight, the step input on the stabilising mass could be found. As has been shown by Karpel et al. [23], the use of a shaker allows for the creation of a self-contained system that can be used during flight tests. The shaker also allows for controlled excitation levels, which means that the same excitation can be applied during multiple tests.

For this experiment, the aeroelastic system is excited using a shaker, which requires a modification to the input and output vectors. The vectors can be derived from Newton's laws. The input force vector on the shaker's static mass that serves as the stabilizing parameter is

$$\{u_f(i\omega)\} = -m_{\text{mv}} \{a_{\text{mv}}(i\omega)\} \tag{2.13}$$

where m_{mv} is the shaker's moving mass, and $\{a_{\text{mv}}(i\omega)\}$ the corresponding acceleration vector. The acceleration response of the stabilising mass m_{st} is given by

$$P_f \{y_f(i\omega)\} = m_{\text{st}} \{a_{\text{st}}(i\omega)\} \tag{2.14}$$

leading to the following input-output relation that needs to be satisfied at the flutter boundary

$$-m_{\text{mv}} \{a_{\text{mv}}(i\omega)\} = m_{\text{st}} \{a_{\text{st}}(i\omega)\} \tag{2.15}$$

The moving mass acceleration $\{a_{\text{mv}}(i\omega)\}$ and the stabilising mass acceleration $\{a_{\text{st}}(i\omega)\}$ are determined using accelerometers placed on the moving mass m_{mv} and on the stabilising mass m_{st}. As both m_{mv} and m_{st} are known, and the accelerations are measured, the matrix $[T(i\omega)]$ can be created for every velocity.

3

Nonlinear Aeroelastic Modelling

Within this chapter, the numerical model developed to calculate the flutter behaviour of the test wing is discussed. The flutter behaviour of the wing needs to be modelled to be able to determine the position and amount of stabilising mass needed for the PFM method. The numerical model is discussed in section 3.1, and the model validation is discussed in section 3.2. Section 3.3 shows the numerical flutter results of the wing using the validated model, with section 3.4 presenting the limitations of the numerical model presented in this work.

3.1. Numerical Model

To design the PFM experiment the anticipated flutter behaviour of the wing needs to be modelled such that the position and amount of stabilising mass can be determined. The modelling approach follows the method presented by Howcroft et al. [25], which utilised the linear aeroelastic deformation solver (SOL 144) within NASTRAN to calculate the aerodynamic loads on the structure, assuming linear deformations. The aerodynamic loads are then applied to the structure, and a nonlinear static analysis (SOL 106) is performed on the original structure to determine the nonlinear static deflections. To converge to the correct static nonlinear aeroelastic solution, the method iterates between SOL 144 and SOL 106 until the solution is converged [25].

The procedure to calculate the static aeroelastic deflection is shown in Figure 3.1 and was implemented using a Python and MSC Nastran coupling. The starting point of the procedure is the Nastran model of the Delft Pazy wing without the wing skin, with an aerodynamic mesh split into 5 sections along the span. Each section contains 7 spanwise panels and 8 chordwise panels, resulting in a total of 280 panels used for the Doublet-Lattice method (DLM) implemented in Nastran. The DLM panels are all splined to the leading and trailing edges of the model, leading to the loads being applied along the leading and trailing edges. An example of the splining of the loads is shown in Figure 3.2. To account for the deflection of the wing, each spanwise section is coupled to a local coordinate system that rotates along the global x and y-axes and has its origin at the leading edge. The rotation along the global x-axis updates the orientation of the aerodynamic mesh due to the out-of-plane deformation and the rotation along the global y-axis accounts for the changes in twist due to the deformation of the wing. The orientation of each local coordinate system is calculated using the deformed positions of the nodes at the corners of each section. Examples of local coordinate systems under a deformed condition are shown in Figure 3.3, with the local coordinate system being indicated with the subscript L, and the global coordinate system having its origin at the root leading edge of the wing.

Just as with the method presented by Howcroft et al. [25], the aerodynamic loads are calculated using SOL 144 after which the loads are extracted and implemented as point follower loads in the nonlinear SOL 400 solver with which the nonlinear deflections are calculated. Using the deformations the orientation of each local coordinate system is updated, resulting in an updated aerodynamic mesh, and the new structural shape is created. To account for the effect of the loads that cause the initial deformation

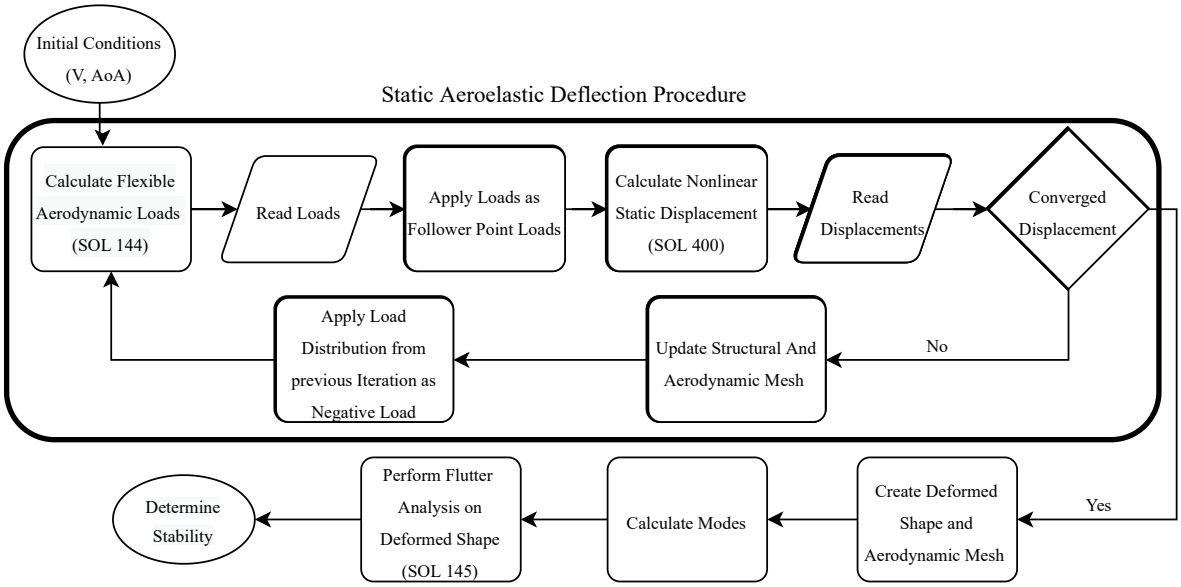

Figure 3.1: Aeroelastic deflection and flutter procedure

a) Aeromesh, indicated with red squares

b) Location of aerodynamic loads, indicated with red dots

Figure 3.2: Aerodynamic mesh and location of load application after splining

in SOL 144, the lift distribution from the previous iterations is added as a follower force acting in the opposite direction to provide the incremental loads necessary. For the SOL 400 solver, an undeformed wing with the loads added from all previous iterations is used to calculate the deformed shape.

The SOL 144 and SOL 400 procedure is performed iteratively until the static convergence criterion for the out-of-plane (z) displacement and the spanwise (y) displacement is reached. The static convergence criterion is an incremental displacement in the out-of-plane (z) and the spanwise (y) directions of less than 1 %. Using the converged static displacements, the structural modes and corresponding eigenfrequencies are determined which serve as the input for the linear flutter analysis (SOL 145) on the static nonlinear shape, using which the aeroelastic stability of the wing in the deformed configuration is assessed.

As stated above, the presented numerical model starts with a no-skin model of the Delft Pazy wing. This means that the starting point of the numerical model has a lower overall stiffness when compared to the physical wing model. Therefore, to account for the stiffness added to the physical wing model by

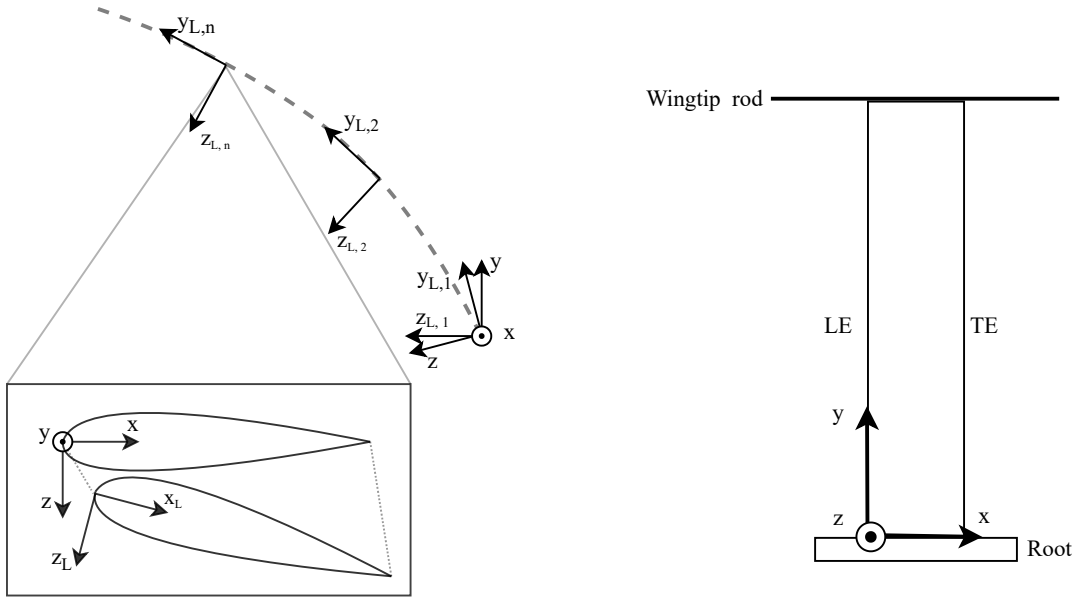

Figure 3.3: Coordinate systems used by numerical model

the Oralight skin, the thickness of the plate was increased, and the stiffness of both the aluminium plate and Nylon-12 wing structure was tuned to match the experimentally determined aeroelastic stiffness.

3.2. Model Validation

As part of the process used to validate the static nonlinear aeroelastic model, the numerical results are compared to experimental deflection results obtained by Mertens et al. [26]. For the validation of the dynamic component of the numerical model used to determine the stability of the wing, GVT results are used.

3.2.1. Static Aeroelastic Deflection

For the validation of the aeroelastic deflection, two cases are compared. The cases are the out-of-plane deflections of the Delft Pazy Wing at a free stream velocity of 18 m/s, and angles of attack $\alpha = 5°$ and $\alpha = 10°$. The comparison between the experimental results and the numerical results is shown in Figure 3.4. The comparison between numerical and experimental displacement is compared at 15 different points that correspond to the positions of the ribs and the tip rod. For the angle of attack $\alpha = 5°$ the difference in tip displacement in z (out-of-plane) is over-predicted by 2.8 %. The tip displacement in y (spanwise) is under-predicted by 0.15 %. For $\alpha = 10°$ the difference in tip displacement is under-predicted by 1.5 % in z (out-of-plane), and in y (spanwise) the numerical displacement is equal to the experimentally determined displacement. Because of the small differences between the numerical model and the experimentally obtained deflections, it can be stated that the numerical model shows good agreement with the experimental results.

Span Validation As part of the validation procedure, the span as calculated using the numerical framework needs to remain constant under all deflected positions. This is achieved through the span-wise shortening and out-of-plane displacement shown in Figures 3.4 and 3.5. The deflection for $\alpha =$ 20° is shown in Figure 3.5 and is used to determine the effects of calculating very large deflections with the presented numerical model.

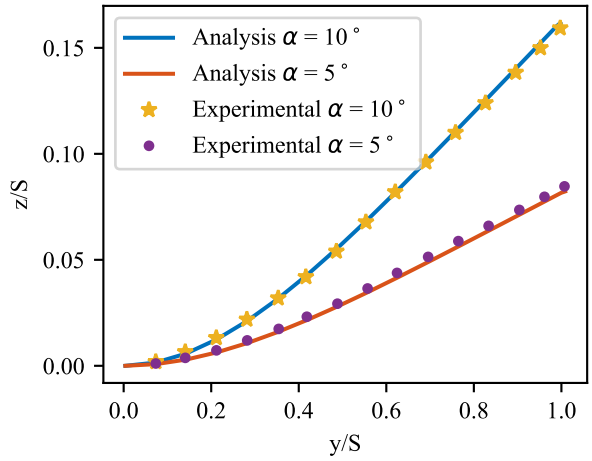

Figure 3.4: Numerical model vs. experimental results. Experimental results obtained from Mertens et al. [26]

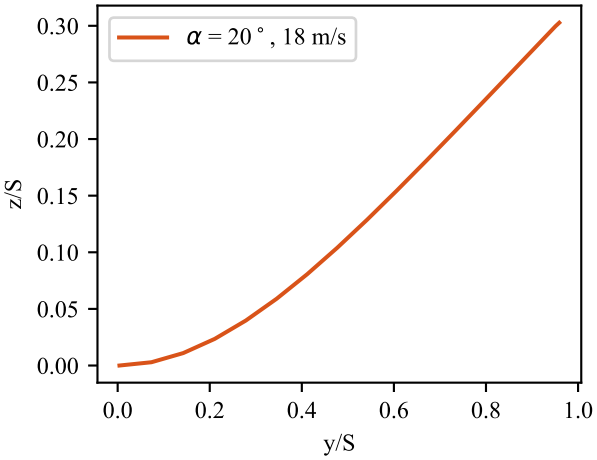

Figure 3.5: Numerical model deflection for $\alpha = 20°$

To determine the span of the deformed wing, and determine if the numerical model shows the expected static deflection behaviour, the distance between two measurement points is calculated using the following equation.

$$d_i = \sqrt{(y_i - y_{i-1})^2 + (z_i - z_{i-1})^2} \tag{3.1}$$

And the distance between all measurement points is summed to get the total span. The span of the undeformed wing model is 0.554 m, and the span of the deflected model at 18 m/s, as calculated using the static aeroelastic deflection framework, is presented in Table 3.1

Table 3.1: Span comparison calculated with numerical model

α (°)	Numerical span (m)	Difference (%)
5	0.555	0.12
10	0.555	0.13
20	0.554	0.12

As can be seen from the calculated spans, a small difference of maximum 0.7 mm, equal to 0.13 % difference in span, is found between the span of the undeformed shape and the deformed shape, which is most likely caused by the numerical rounding error inherent in the Nastran solver and Python implementation used to write the input .bdf files.

3.2.2. Ground Vibration Testing

The comparison between the GVT results, obtained using the experimental procedure described in Appendix A, and the corresponding setup shown in section 4.2.2, and the analysis model is shown in Table 3.2, the differences for the first five eigenmodes are on average less than 7 %.

It is interesting to note that the out-of-plane and torsional modes are captured well, whereas the in-plane mode is not. The difference in the in-plane direction is most likely caused by the difference in the clamping of the main spar in the numerical model and the experiment, as the main spar is clamped using two aluminium blocks at its root which allows for more freedom of movement in the for-and-aft direction when compared to the numerical model. However, the large difference for the 1st in-plane bending mode does not cause a detrimental effect on the predicted flutter velocity because its natural frequency is still well above the 1st torsion frequency and the expected flutter frequency.

Table 3.2: Comparison between the Analysis Model and the GVT results

	Clean Configuration		
Mode Type	f_{FEM} [Hz]	f_{GVT} [Hz]	Δf [%]
1st Bending	3.1	3.3	-6.0
2nd Bending	21.6	22.8	-5.3
1st Torsion	27.5	29.5	-6.8
3th Bending	64.0	67.4	-5.0
2nd Torsion	111.7	124.0	-9.9
1st In-Plane Bending	102.6	62.9	63.1

3.3. Numerical Flutter Results

Using the presented numerical model, the flutter behaviour of the Delft Pazy Wing can be determined. Figure 3.6 shows the stability region of the wing as used by Mertens et al. [26]. Looking at the V-g and V-f plots in Figures 3.7 - 3.10 the evolution of the damping and frequency with velocity is shown, with each point representing a different V-α combination.

As the frequencies of the second bending and first torsion modes start to become closer to each other and the first torsion mode becomes unstable, indicated by the positive damping (g) value, it can be concluded that the first unstable region in Figure 3.6, is caused by 2nd bending - 1st torsion flutter mechanism and is a hump mode. The hump mode is caused by the first torsion mode becoming stable at higher velocities. An effect that is seen in Figures 3.7 - 3.10 is that the region of the hump flutter mode becomes smaller and that the maximum value of the damping g becomes smaller with increasing α.

Looking at the frequencies and damping values of the eigenmodes at velocities above the first unstable region, it can be seen that the frequency of the first torsion mode becomes lower than the frequency of the second bending mode. Combined with the first torsion mode becoming unstable again at higher velocities, it can be concluded that the second unstable region in Figure 3.6, seen for $\alpha = 2°$ to $8°$ is caused by 1st bending - 1st torsion flutter mechanism.

Looking at previously obtained results by Drachnisky et al. [27] for the Pazy Wing, it can be concluded that the results obtained using the presented numerical model show the same kind of behaviour as the Pazy Wing, albeit with the flutter onset velocity obtained for the Delft Pazy Wing being lower, as the

spar thickness of the Delft Pazy Wing is thinner than in the original Pazy Wing [26], [28].

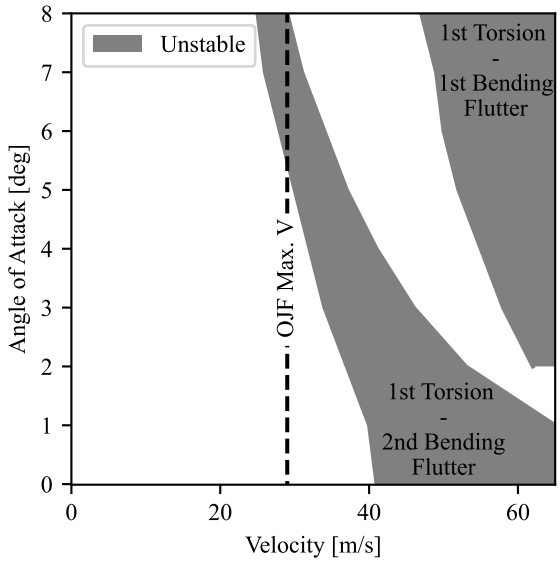

Figure 3.6: Stability Region Clean Delft Pazy Wing

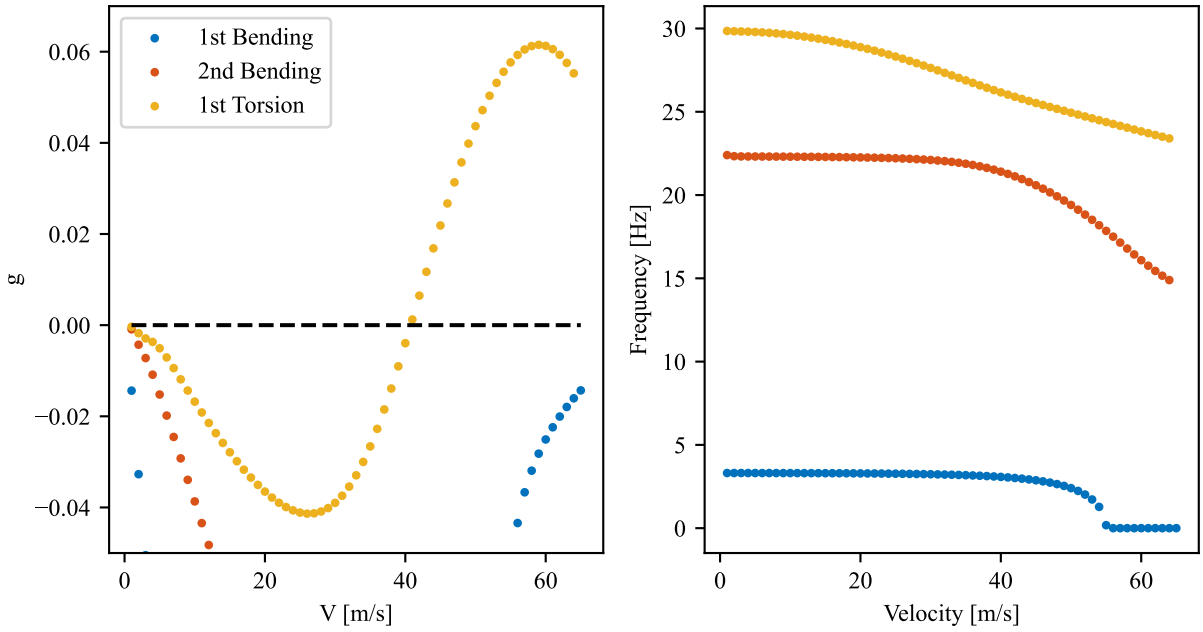

Figure 3.7: Vg-Vf plot baseline configuration $\alpha = 0°$

3.4. Numerical Model Limitations

The currently presented numerical model allows for the determination of the aeroelastic stability of a wing under deflected conditions caused by a selected $V - \alpha$ pair, which shows the expected reduction in flutter velocity with increasing deflection. However, the dynamic behaviour modelled using SOL 145 can only represent the linear flutter behaviour around a static nonlinear shape and cannot model the full dynamic nonlinear behaviour expected with the occurrence of an LCO.

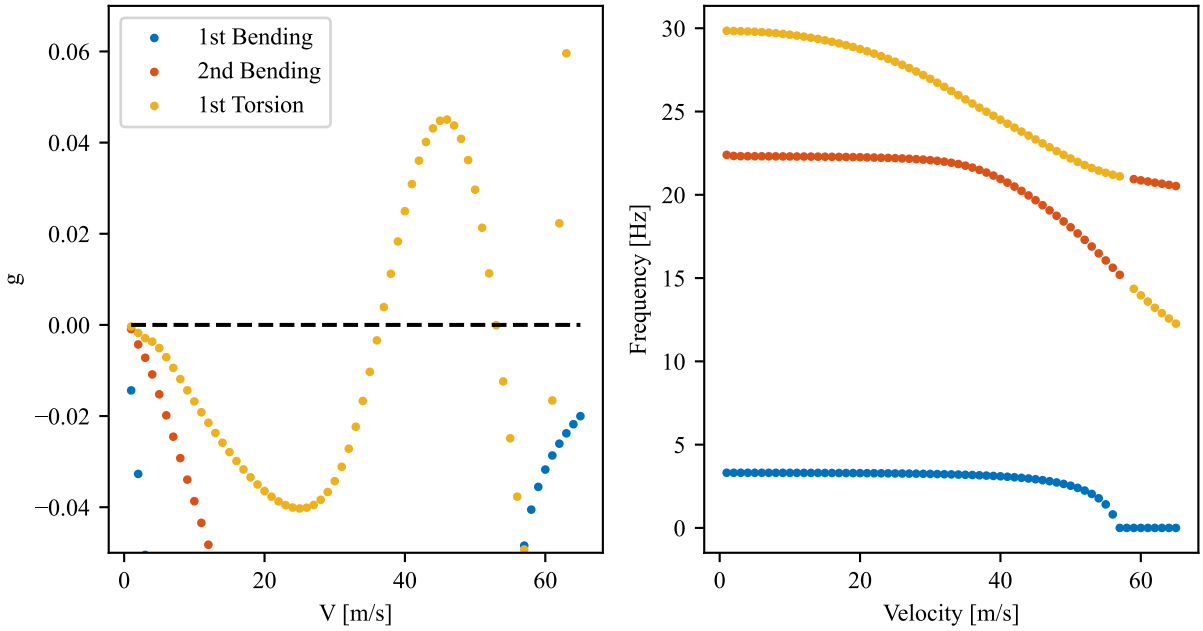

Figure 3.8: Vg-Vf plot baseline configuration $\alpha = 2°$

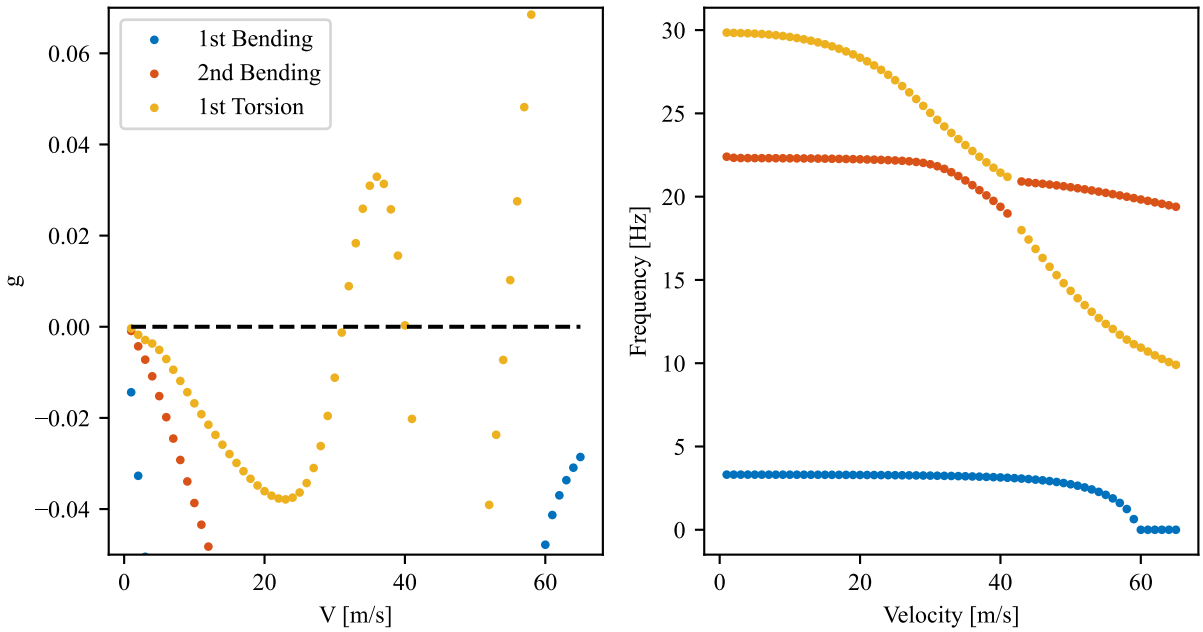

Figure 3.9: Vg-Vf plot baseline configuration $\alpha = 4°$

Another limitation of the presented numerical model is the numerically expensive static aeroelastic deflection procedure, which takes on average anywhere between 30 min to 40 min to converge to a deflected position, when running on the HPC cluster of the faculty of aerospace engineering at TU Delft, and is caused by the implementation of the nonlinear SOL 400 solver, which always starts from a straight wing with all the loads added such that a deformed iteration can be calculated. The numerical cost of this process could be reduced by using a pre-deformed model in the SOL 400 solver and applying the incremental loads just as is done within the SOL 144 solver, or by starting the model from a previous $V - \alpha$ pair such that only the velocity increment needs to be added to the model.

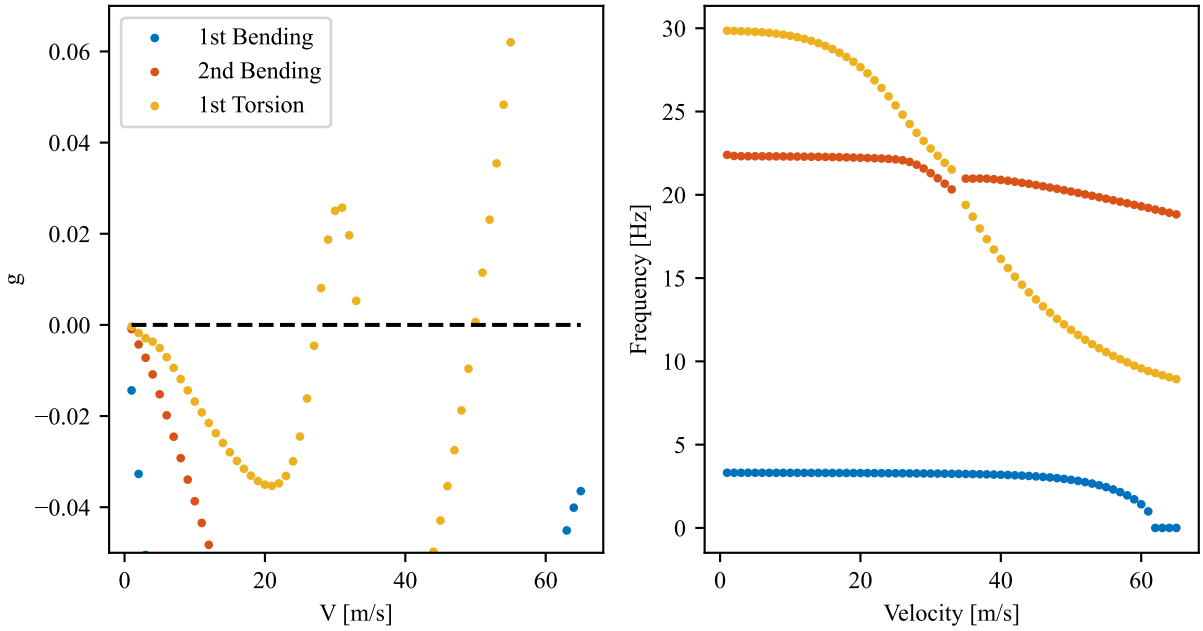

Figure 3.10: Vg-Vf plot baseline configuration $\alpha = 6°$

However, knowing the limitations of the numerical model, the stability region of the wing can be determined and the sensitivity study necessary to determine the position and mass of the stabilising mass can be performed, from which the results can be used as an input to design the experiment and the expected stability region of the wind tunnel model can also be determined.

4

Design of Experiment and Test Setup

Within this chapter, the design of the experiment and corresponding test setup are presented. First, section 4.1 describes the steps taken to design the wing such that it can be used during the PFM experiments. This is followed by section 4.2, which presents the test setup and procedures used during the experimental campaign.

4.1. Design of Experiment

For the design of the PFM experiment, the required amount of stabilising mass necessary for the PFM method needs to be determined. Furthermore, the amount of mass necessary to destabilise the wing such that flutter can occur within the wind tunnel velocity range is also determined.

To be able to determine the position and amount of mass, first, the wing model is introduced in section 4.1.1. This section is followed by section 4.1.2, where the effect on the flutter boundary caused by different mass positions and mass amounts is presented. Using the effects of different mass positions and amounts, the flutter pod was designed. The design is shown in section 4.1.3, with this section concluding with section 4.1.4 which presents the expected flutter behaviour of the wing used during the wind tunnel campaign.

4.1.1. Delft Pazy Wing

The model used during the wind tunnel test campaign consists of the flutter pod and the Delft Pazy Wing which was first used by Mertens et al. [26] and is based on the Pazy Wing designed by Avin et al. [28]. The different dimensions and parameters of the wing are shown in Table 4.1.

Table 4.1: Parameters Delft Pazy Wing [26]

Span	550 mm
Chord	100 mm
Tip Rod	272 x 10 mm
Spar	550 x 60 x 1.5 mm
Spar material	aluminium 7075
Structure material	Nylon 12
Skin material	Oracover Oralight
Aerofoil	NACA0018
Wing mass	260 gram

A full overview of the wing and the different components Figure 4.1. To measure the response of the wing during the direct flutter tests and the PFM tests, the wing was instrumented using eight single-axis

accelerometers and a tri-axis accelerometer placed at the tip leading edge position.

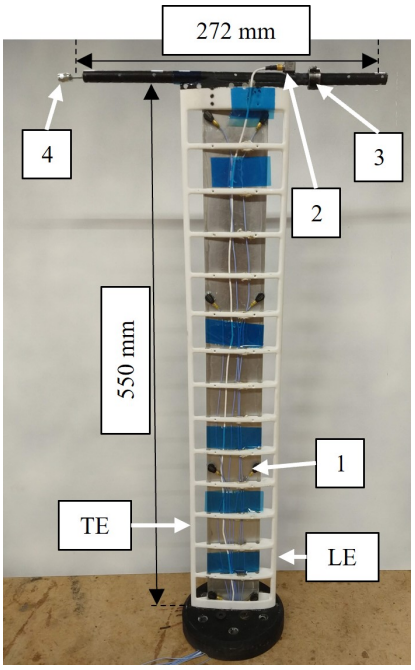

Figure 4.1: Delft Pazy Wing with instrumentation. 1: 8x Single-axis accelerometer (PCB Piezotronics 352A24), 2: Tri-axis accelerometer (Dytran 3333A2T), 3: Destabilising mass 10 gram, 4: Destabilising mass 3.26 gram

4.1.2. Required Masses

With the dimensions and parameters of the wing known, the location and amount of stabilising necessary for the PFM method can be determined by performing a sensitivity study using the numerical model presented in chapter 3, the stability region of different configurations can be studied. As part of the experiment, the SISO PFM method is also applied to the wing. Therefore, the flutter velocity of the wing in an undeformed state at $\alpha = 0°$ should also be within the wind tunnel velocity range. With the maximum velocity range of the Open Jet Facility at the TU Delft being 30 m/s[1], the flutter velocity of the wing should be less than 30 m/s. However, looking at the expected flutter behaviour of the Delft Pazy Wing is shown in Figure 3.6, it can be seen that the flutter velocity of the wing needs to be reduced.

To achieve a reduction of the flutter velocity of the second bending – first torsion flutter mechanism to within the wind tunnel velocity range for all angles of attack, a 10 gram mass is placed on the tip rod in front of the leading edge (LE). The stability region of the destabilised wing can be seen in Figure 4.2, which shows an unstable wing for all angles of attack. This model is used to determine the optimal location and amount of stabilising mass necessary to be able to perform the PFM method.

To determine the effect of the addition of mass on the tip rod at the trailing edge, 24 gram and 30 gram point masses were added to the numerical model approximately 0.5 cm in front of the TE. The comparison between the destabilised wing, seen in Figure 4.2, and the stabilised configurations is shown in Figure 4.3. As can be seen, the configuration with 24 gram stabilising mass increases the flutter velocity at lower angles of attack but decreases the flutter velocity at $\alpha \geq 5°$, which is caused by the reduction of the torsion frequency causing the second bending mode and first torsion mode to couple at a lower velocity. The configuration with 30 gram stabilising mass increases the flutter velocity of the second bending – first torsion flutter mechanism, and also reduces the size of the unstable region corresponding to this flutter mechanism. This is caused by the reduction of the first torsion frequency resulting in an earlier mode flip with second bending. In general, to further increase the expected flutter

[1] https://www.tudelft.nl/lr/organisatie/afdelingen/aerodynamics-wind-energy-flight-performance-and-propulsion/facilities/low-speed-wind-tunnels/open-jet-facility [accessed 10 May 2022]

velocity, the mass at the current tip position needs to be increased, or the mass needs to be moved further back.

The comparison in Figure 4.3 clearly shows the effect of the addition of the stabilising mass, with the size of the second bending – first torsion flutter mechanism reducing, and nearly fully disappearing with the addition of sufficient stabilising mass, as can be seen for 30 gram. Looking at the second stability region, related to the first bending – first torsion flutter mechanism, it can be seen that the size of this unstable region has become larger when compared to the destabilised wing. This effect is caused by the fact that the tip TE position is not a beneficial position to provide a stabilising effect to the first bending – first torsion flutter mechanism, as this position reduces the first torsion natural frequency, resulting in an earlier interaction with the first bending mode with unfavourable mass coupling between the two

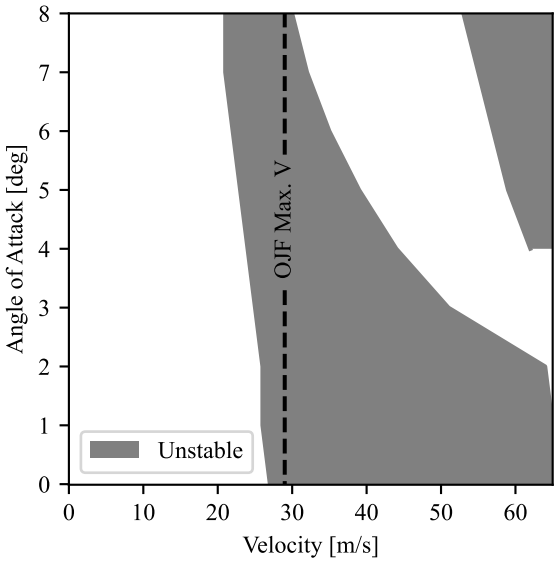

Figure 4.2: Stability region destabilised wing

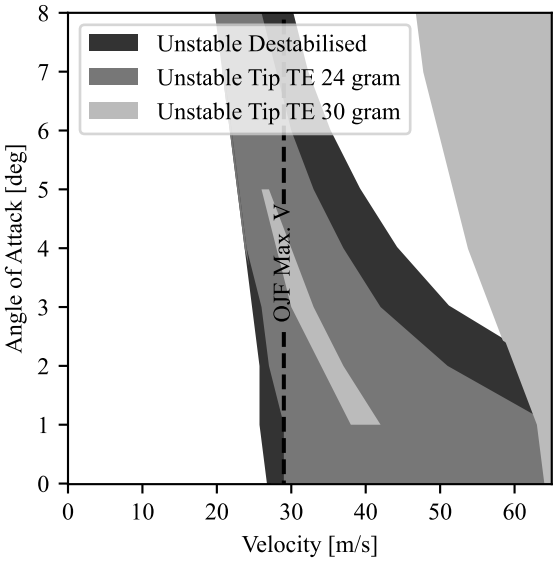

Figure 4.3: Stability region tip TE comparison

Another location that can be used to stabilise the second bending – first torsion flutter mechanism, is

to use the mid-span position at the leading edge. This position reduces the frequency of the second bending mode, resulting in a greater difference between the second bending mode and the first torsion mode. Therefore, a higher velocity is necessary for the modes to couple and the flutter mechanism to form. In addition, the effect of the chordwise location of the added mass is opposite to that in the tip section, which implies that a forward location has a stabilizing effect. Figure 4.4 shows the comparison between the destabilised configuration and two stabilised configurations with 10 gram and 16 gram added respectively. As expected, the addition of the stabilising masses increases the flutter velocity of the second bending – first torsion flutter mechanism.

Comparing the second unstable region in Figure 4.4, it can be seen that the first bending – first torsion flutter mechanism is not influenced by the addition of the stabilising mass at the mid-span LE position. In this case, the fact that the first bending – first torsion flutter mechanism is not influenced is caused by the fact that the mid-span LE position only significantly reduces the frequency of the second bending mode, leaving the first bending – first torsion flutter mechanism unaffected.

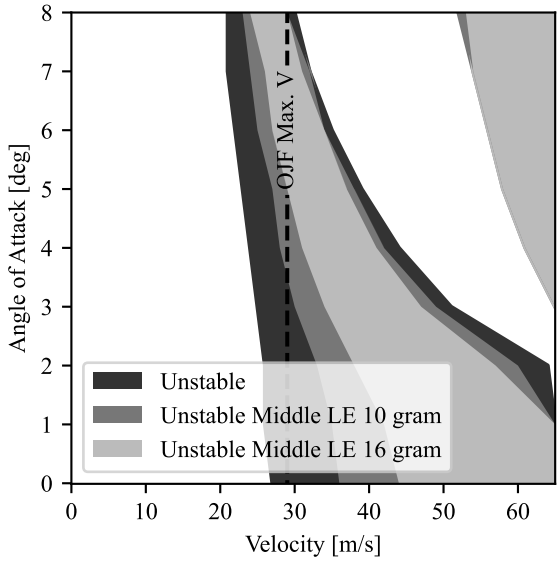

Figure 4.4: Stability region mid-span LE comparison

As can be deduced from Figure 4.4, the addition of 6 gram would result in an increase of the flutter velocity of 7 m/s at $\alpha = 0°$. Further sensitivity studies showed that the addition of small masses along the trailing edge, in the order of 1 gram to 2 gram resulted in a different flutter behaviour in the order of 1 m/s to 3 m/s, hence, all the expected masses, such as the sensor cables and destabilising masses, were included in the design of the flutter pod, such that the expected flutter behaviour can be determined.

All the destabilising masses used on the wing are also indicated in Figure 4.1, with 10 gram mass placed on the tip rod, approximately 15 mm in front of the leading edge and a 3.2 gram mass added to the rear of the tip rod.

4.1.3. Flutter Pod Design

Using the results from the sensitivity study in the previous section, a shaker carrier and shroud were designed. The shroud is necessary to be placed on the wing to make sure that the movement of the shaker is not influenced by the airflow. The shroud has been designed to be a part of the nominal configuration used during the PFM testing to not change the aerodynamics of the wing between the direct flutter tests and the PFM tests.

The first flutter pod design used the tip rod TE position to stabilise the wing. However, the inertia of the corresponding flutter pod resulted in the first torsion mode having a lower frequency than the second bending mode. This means that the second bending – first torsion flutter mechanism, with the shroud included in the nominal structure, can not form. Because of the mode flip and the sensitivity of the exact

mass location on the tip rod, the mid-span LE position was chosen. The shroud and shaker attachment designed for this configuration is presented below.

The flutter pod at the mid-span leading edge position consists of a wing clamp, an aerodynamic shroud and a micro-shaker system. The shroud is permanently installed on the wing and consists of two parts that click into each other to encase the shaker and wing clamp. The wing clamp, which constitutes part of the stabilising mass, is 3D-printed and clamps around the LE and is secured with two bolts and nuts. The bolts are also used to attach one half of the shroud to the wing, with the other half being attached through a clip mechanism.

The design of the wing clamp is shown in Figure 4.5 and contains three attachment points for the shaker to be oriented in the local x, y or z direction. The clamp also allows for the installation of a tri-axis accelerometer used to measure the response of the stabilising mass in all three directions simultaneously. The clamp is encased in the aerodynamic shroud such that it has the same aerodynamic influence on the wing regardless of the shaker's orientation, such that the shaker is not influenced by the oncoming flow. The CAD model of the two halves of the shroud assembled is shown in Figure 4.6, and the dimensions of the right half are shown in Figure 4.7, with the main dimensions of the shroud being symmetric. Because of the large size of the shroud compared to the wing chord and thickness, c = 100 mm and t_{max} =18 mm, the shroud is part of the nominal configuration used during the direct flutter and PFM tests.

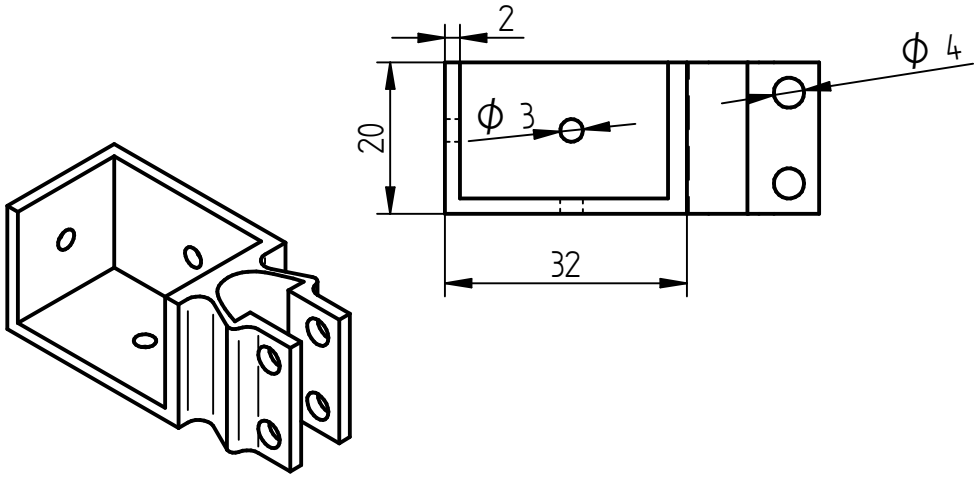

Figure 4.5: Wing clamp. Dimensions in mm

The full overview with all components that are part of the flutter pod is shown in Figure 4.8, with the shroud (1), tri-axis accelerometer (2) used to measure the response, wing clamp (3) and micro-shaker system (4) all being indicated. The installed version of the flutter pod on the wing (1) is shown in Figure 4.9, with the shroud (2) and all the stabilising mass (3) which is part of the PFM configuration. The figure also shows the permanently installed sensor cables (4) used to measure the stabilising mass acceleration as well as the moving mass acceleration.

The micro-shaker system first indicated in Figure 4.8, is shown fully assembled in Figure 4.10, and it is based on a linear voice coil of the type LVCM-013-008-02 manufactured by MotiCont[2] and consists of both moving and stationary components. The stationary components of the micro-shaker system and the 3D-printed wing clamp form the stabilising mass. The moving component of the shaker consists of a permanent magnet and a single-axis accelerometer. The moving component of the shaker weighs

[2]MotiCont lvcm-013-008-02 `http://www.moticont.com/lvcm-013-008-02.htm` [accessed 16 October 2022]

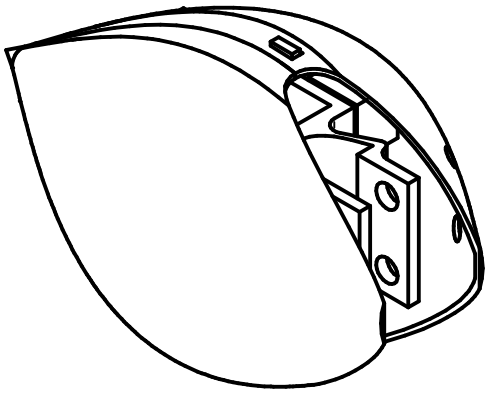

Figure 4.6: Shroud

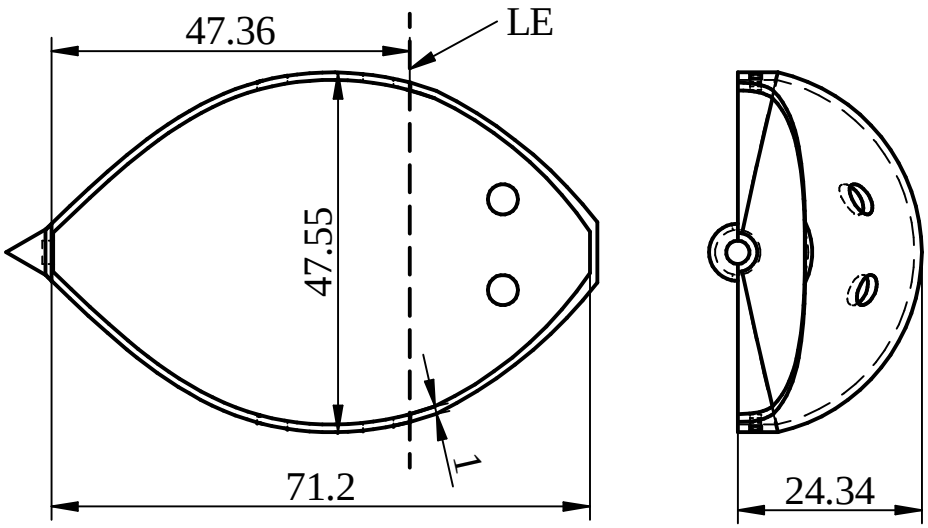

Figure 4.7: Shroud right half. Dimensions in mm

6.4 gram, with all the stationary weight used to stabilise the system weighing 9.7 gram. A full overview of all the masses constituting the flutter pod is shown in Table 4.2.

The moving mass component of the micro-shaker system also contributes to the aeroelastic stability of the wing, as it also provides a mass at the stabilising position increasing the onset velocity of the second bending – first torsion flutter mechanism.

Using the design of the flutter pod, three different configurations related to the PFM experiment and data analysis can be identified. To be able to distinguish between the different configurations, an overview of

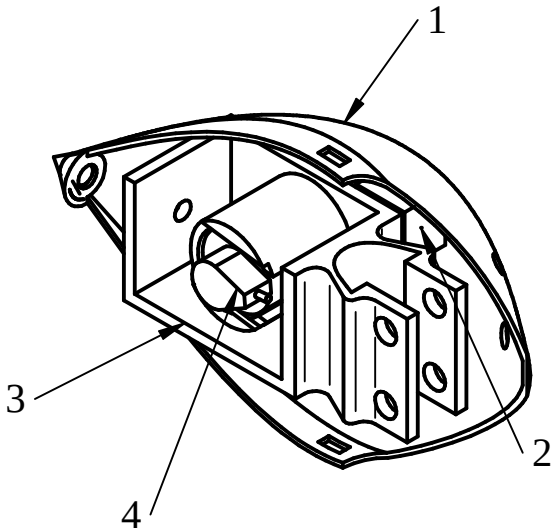

Figure 4.8: Flutter pod, 1: Shroud right half, 2: Tri-axis accelerometer (Dytran 3333A2T), 3: Wing clamp and stabilising mass, 4: Micro-shaker system

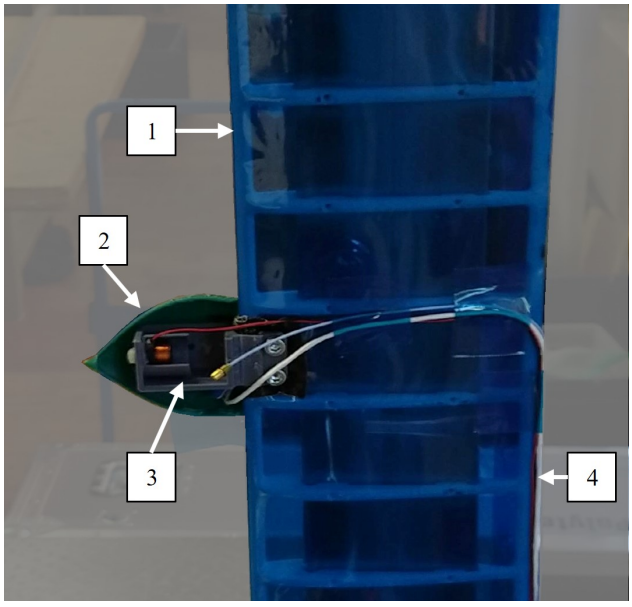

Figure 4.9: Stabilising mass installed on Delft Pazy Wing. 1: Delft Pazy Wing, 2: Shroud, 3: Stabilising mass, 4: Cables accelerometers (part of nominal configuration),

the components constituting the different configurations is shown in Table 4.3. The three configurations are called 1) Nominal, 2) PFM and 3) Full. The Nominal configuration, which includes the permanently installed stationary mass, forms the non-stabilised configuration for which the flutter conditions are identified. The PFM configuration is the nominal configuration plus the added stabilising mass. This is the configuration on which the shaker provides the excitation and from which the PFM results are determined. The final configuration is the full configuration, which adds the moving mass to the PFM configuration. In the full configuration, the moving mass does not provide excitation and is an additional stabilising mass placed on the wing.

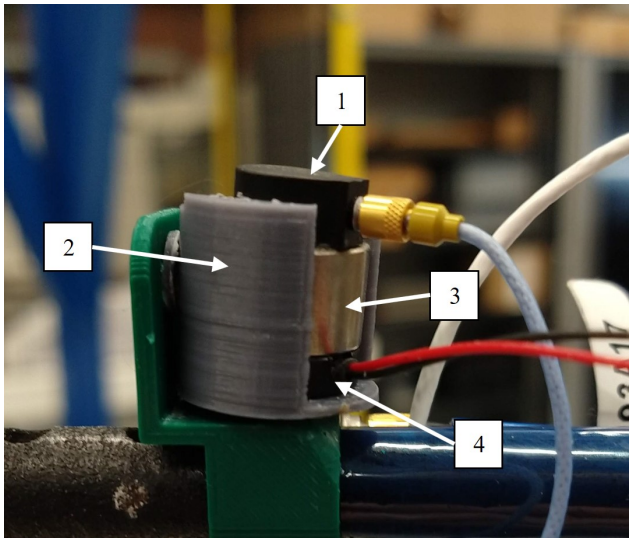

Figure 4.10: Electromagnetic shaker. 1: Single-axis accelerometer (PCB Piezotronics 352A24), 2: Shaker support with end stops, 3: Moving permanent magnet, 4: Stationary voice coil

Table 4.2: Flutter pod mass

Component	Mass (gram)
Shroud	11.2
Bolts & Nuts	9.2
Shaker Base	2
Shaker Support	1.2
Wing Clamp with 3-axis accelerometer	6.5
Total Stationary Mass	30.1
Of which permanently installed	20.4
Of which stabilising	9.7
Moving Mass with 1-axis accelerometer	6.4
Total Mass	36.5

Table 4.3: Wing configurations

Components	Nominal Configuration	PFM Configuration	Full Configuration
Shroud and Bolts	x	x	x
Sensor cables	x	x	x
Destabilising mass	x	x	x
Wing clamp and 3-axis accelerometer		x	x
Shaker stationary mass		x	x
Shaker moving mass			x

4.1.4. Numerical Flutter Results for the Wind Tunnel Test Configuration

Using the updated numerical model, which includes all the destabilising masses and sensors described above, the flutter behaviour of the nominal and PFM configurations were determined and are shown in Figure 4.11. The stability region for the nominal configuration shows the expected flutter velocity at $\alpha = 0°$ to be 25 m/s, which is decreasing with increasing α. Looking at the V-g and V-f plots corresponding to the nominal configuration in Figures 4.12 – 4.15 for $\alpha = 0°$, 2°, 4° and 6° respectively, it can be seen that the first flutter mechanism is caused by the interaction between second bending and first torsion, and the second flutter region is caused by the first bending and first torsion interaction. What is also seen in the V-g plots, is that the analyses were performed with zero structural damping. This leads to the results shown in Figure 4.11 being slightly conservative. Nevertheless, these results are still adequate, as demonstrated by the test results below.

This behaviour is similar to the one seen for the clean wing presented in section 3.3, which is as expected, as the mass distribution is only influenced by the addition of the destabilising masses, which results in a lower flutter velocity.

Returning to the V-g and V-f plots in Figures 4.12 – 4.15, several differences, besides the reduction in flutter velocities, with the V-g and V-f plots seen in section 3.3 are found. Comparing the V-g and V-f plots for $\alpha = 0°$, it can be seen that the maximum positive value of the damping g is higher for the destabilised model.

Furthermore, for the non-zero angles of attack, the width of the hump mode is larger when compared to the size of the hump mode seen in section 3.3. The unstable region for a larger velocity range is most likely caused by the inertia of the point masses representing the shroud and the destabilising masses.

Looking at the numerical flutter results for the PFM configuration, with 9.7 gram added to the mid-span LE position, shown in Figure 4.11, it can be seen that the flutter velocity is drastically increased when compared to the nominal configuration. Therefore, it is possible to apply the PFM method to safely determine the flutter boundary of the nominal wing, over the entire range of angles of attack, without experiencing excessive vibrations.

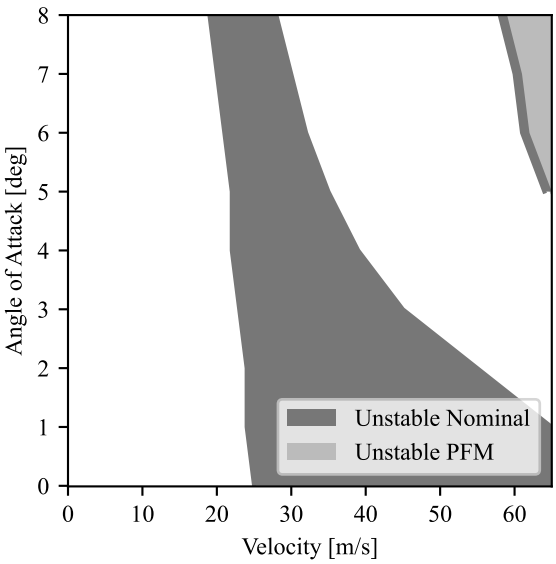

Figure 4.11: Comparison stability region nominal and PFM configurations

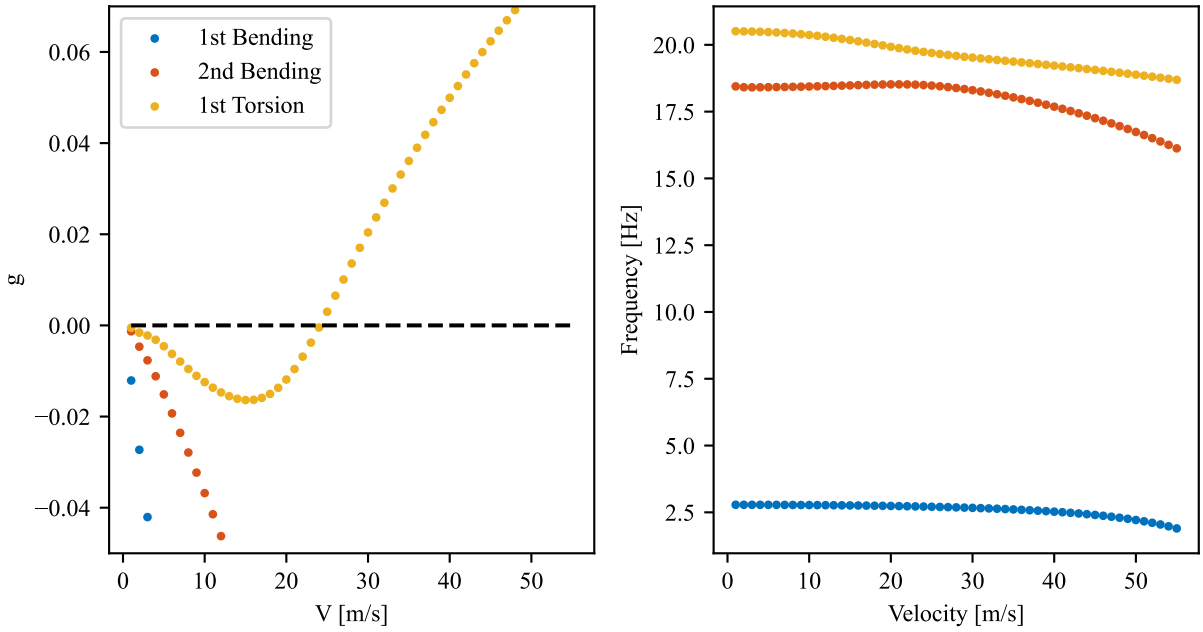

Figure 4.12: Vg-Vf plot, nominal configuration $\alpha = 0°$

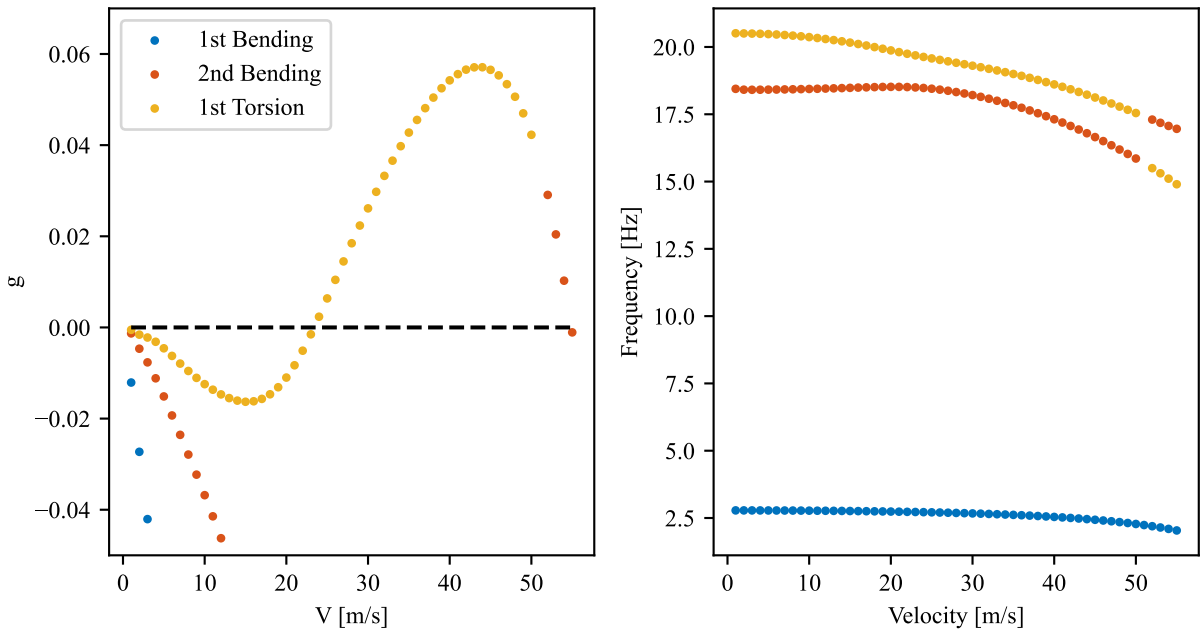

Figure 4.13: Vg-Vf plot, nominal configuration $\alpha = 2°$

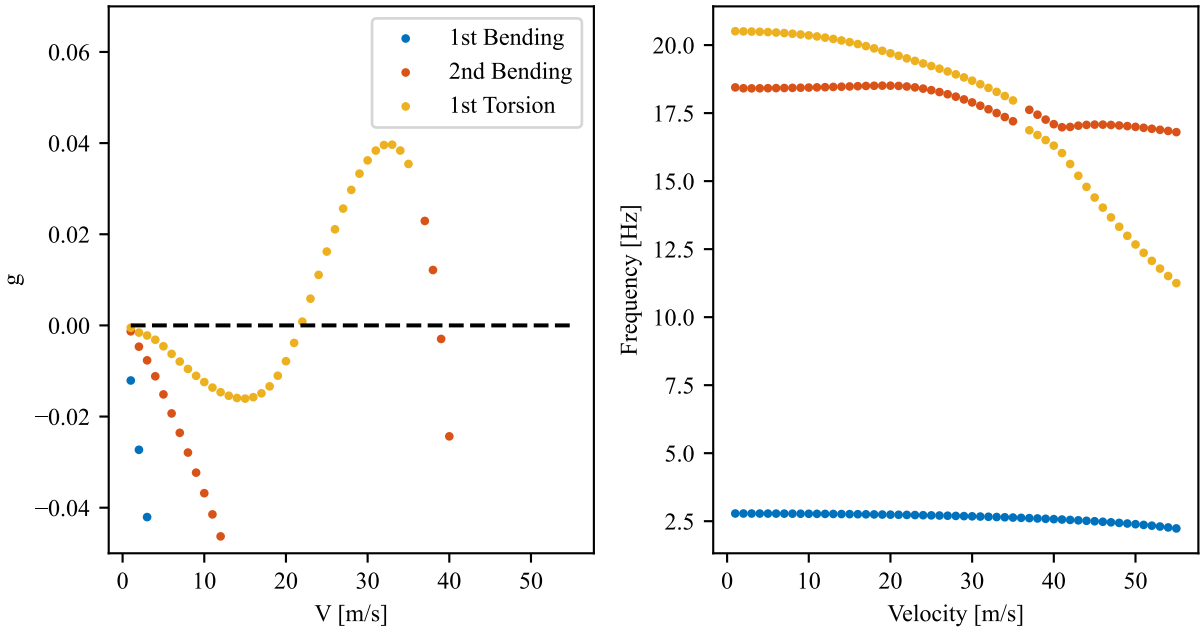

Figure 4.14: Vg-Vf plot, nominal configuration $\alpha = 4°$

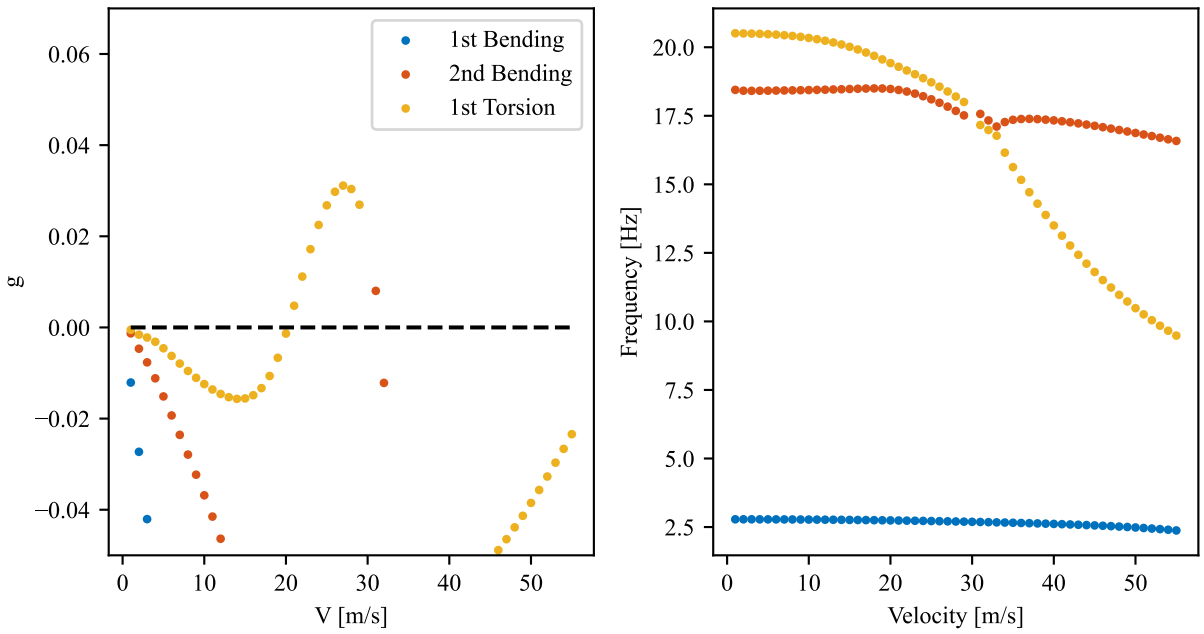

Figure 4.15: Vg-Vf plot, nominal configuration $\alpha = 6°$

4.2. Wind Tunnel Test Configuration

With the flutter pod designed and the wing characterised, the wind tunnel measurement procedures and test setups are presented in this section.

4.2.1. Data Acquisition

To be able to control the micro-shaker system and measure the response of the stabilising mass within the flutter pod a Siemens Simcenter SCADAS Mobile Recorder[3] is used, which also records the full aeroelastic system response and generates the required FRFs for the PFM method from the measured accelerations seen by the moving mass and the stabilising mass. The shaker was provided with a continuous random signal having a frequency content in the range between 1 and 30 Hz for a duration of 52 s per measurement. At every testing condition, the measurement was repeated three times to obtain an averaged FRF thereby increasing the signal-to-noise ratio.

4.2.2. Ground Vibration Tests

Using the wind tunnel model of the wing, GVTs were performed to be able to determine the modal behaviour of the wing and compare it to the numerical model, from which the modal results are used during the numerical determination of the stability regions of the wing described above. An overview of the setup used during the GVTs is shown in Figure 4.16, with the full experimental GVT procedure described in Appendix A. The GVTs have been performed both in out-of-plane and in-plane directions to be able to capture the out-of-plane bending and torsion modes as well as the first lead-lag mode and were performed on the Nominal and PFM configurations.

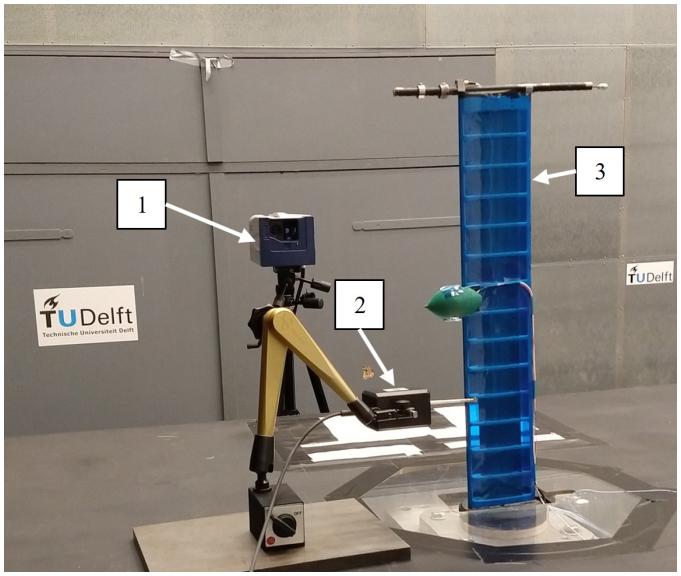

Figure 4.16: Ground vibration test experimental setup 1: Laser scanning vibrometer, 2: Modal hammer, 3: Delft Pazy wing

Even though GVT results were previously presented in section 3.2, the measurements were repeated as the previous measurements did not include all sensors, destabilising masses and the flutter pod at the mid-span leading edge position. Furthermore, the GVTs were repeated as during the wind tunnel campaign the Oracover Oralight skin was replaced as some of the embedded sensors needed to be replaced.

The GVT measurements were performed using a Polytec PSV-500 laser scanning vibrometer (LSV) with a frequency range of up to 800 Hz. The excitation of the wing was achieved using a Maul-Theet

[3] Simcenter SCADAS Mobile and SCADAS Recorder, Siemens - Community support, 2022 https://community.sw.siemens.com/s/article/simcenter-scadas-mobile-and-scadas-recorder [accessed 9 October 2022]

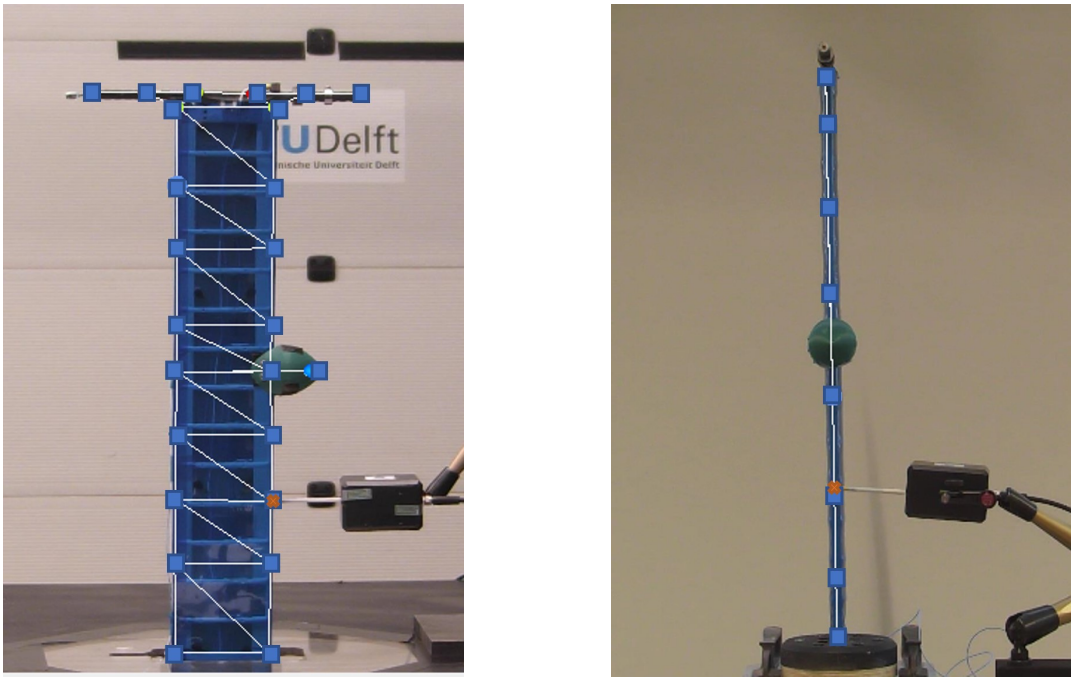

a) Out-of-plane **b)** In-plane

Figure 4.17: GVT Measurement Points (blue squares) and the driving point (red cross)

vImpact-61 automatic modal hammer[4]. The LSV data has been processed using SimCenter TestLab. For the out-of-plane GVT, the vibration data was acquired at 25 points, as shown in Figure 4.17a. Nine measurement points were placed at the leading edge, nine at the trailing edge and six on the tip rod. When running the GVTs on the configuration with the shroud at the midspan position, an extra measurement point was added to the shroud. For the in-plane GVT, the vibration data was measured at 8 points along the leading edge, and are indicated in Figure 4.17b.

The comparison between the GVT results and the analysis model is shown in Table 4.4. Just as seen in section 3.2, both the out-of-plane and torsional modes are captured well by the model, whereas the in-plane mode is not, with the reasons why this is not causing a detrimental effect on the flutter prediction having previously been discussed in section 3.2.

Table 4.4: Comparison between the analysis model and the GVT results

	Nominal Configuration			Full Configuration		
Mode Type	f_{FEM} [Hz]	f_{GVT} [Hz]	Δf [%]	f_{FEM} [Hz]	f_{GVT} [Hz]	Δf [%]
1st Bending	2.8	2.9	-3.1	2.7	2.8	-2.6
2nd Bending	18.5	19.6	-5.6	17.4	19.1	-8.6
1st Torsion	20.5	21.5	-4.4	20.3	20.5	-1.0
3th Bending	60.3	63.3	-4.8	60.2	62.5	-3.7
2nd Torsion	78.7	80.8	-2.6	72.3	70.2	2.9
1st In-Plane Bending	91.6	58.9	55.4	90.7	58.2	55.9

[4]Automatic Modal Hammer | vImpact vImpact-Serie `https://maul-theet.com/products/vibration-modal/hardware/automatic-modal-hammer/` [accessed 18 October 2022]

4.2.3. Wind Tunnel Setup

The PFM wind tunnel experiments were performed in the Open Jet Facility (OJF) at Delft University of Technology, which is a closed-loop wind tunnel with an open test section. The octagonal outlet of the OJF spans 2.85 m x 2.85 m and can reach a maximum velocity of 30 m/s[1].

The wind tunnel setup and the relevant components are indicated in Figure 4.18, with Delft Pazy Wing model (1) attached vertically in the OJF test section. The wing was placed on a six-degree-of-freedom force balance (2) which was mounted to a rotating table (3) which allows for the setting of the geometric angle of attack, α, with respect to the inflow. To reduce the wind tunnel interference effects, the balance and rotating table were placed below a splitter plate (4). The SCADAS Mobile data recorder (5) and Power amplifier (6) indicated in Figure 4.18 are used to control and measure the flutter pod excitation and system response. To measure the wing deflection and the tip oscillation during the LCO, an OptiTrack[5] motion recovery system was used.

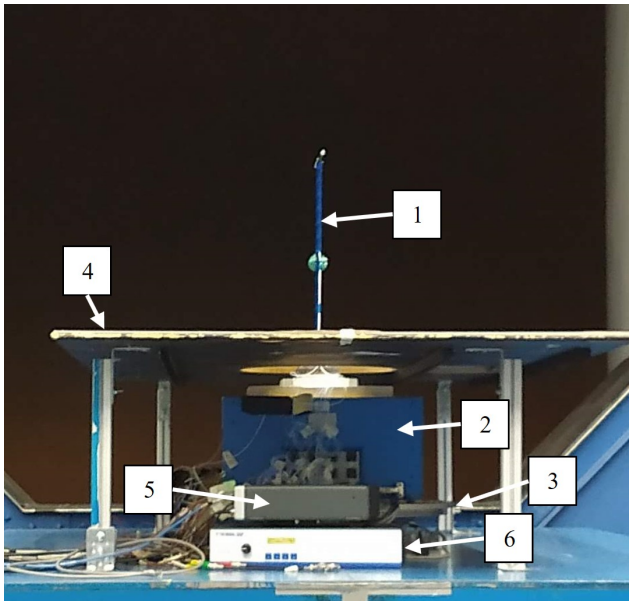

Figure 4.18: Wind tunnel setup; Looking upstream. 1: Delft Pazy Wing, 2: 6-Component Force Balance, 3: Siemens Simcenter SCADAS Mobile data recorder, 4: Power amplifier

The control setup used during the experiments is shown in Figure 4.19, with the wind tunnel control (1), force balance (2) and camera (3) being used to control the wind tunnel velocity and monitor the system response. The data acquisition PC (4) was used to send the commands to run the PFM experiment to the SCADAS Mobile Data Recorder, and read the response after a measurement. The data acquisition PC also allowed for the on-site analysis of the measured FRFs to be able to determine the functioning of the shaker and the corresponding PFM results.

[5]OptiTrack `https://optitrack.com/` [accessed 25 October 2022]

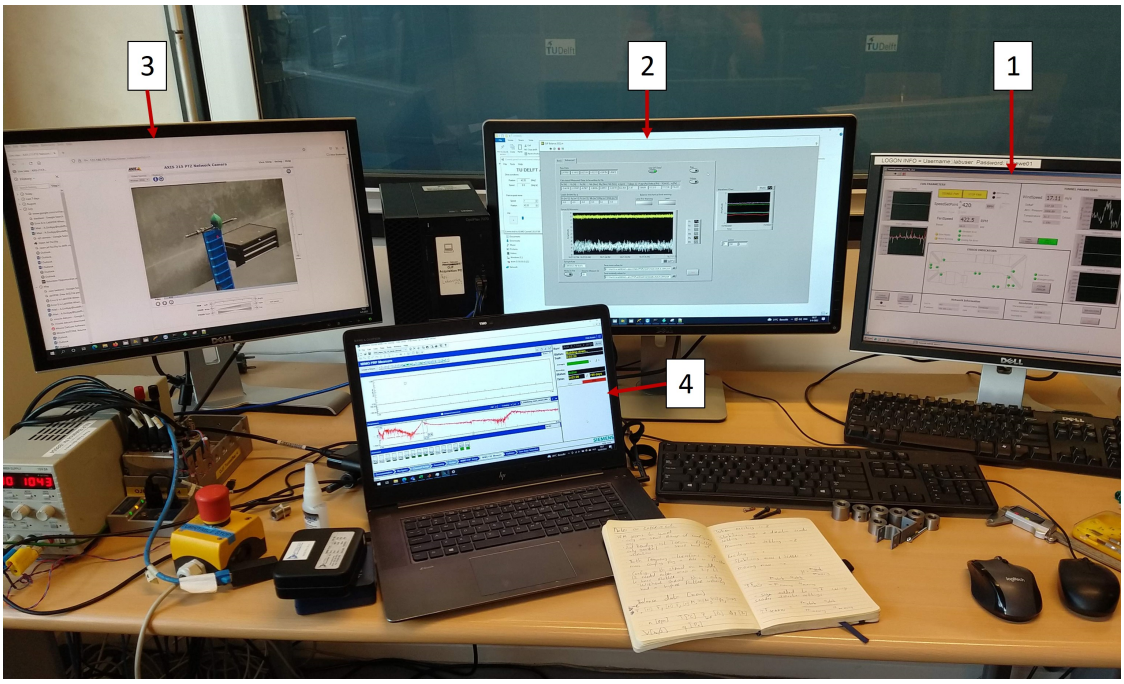

Figure 4.19: Wind tunnel control setup. 1: Wind tunnel control, 2: Force balance, 3: Camera, 4: Data acquisition PC

5

Data Analysis

Within this chapter, the data analysis steps taken to evaluate the measured FRFs and obtain the corresponding flutter margins are presented. First, the data smoothing process is described in section 5.1, after which section 5.2 presents the required correction factors. Finally, the assembly process of the MIMO PFM transfer function matrix, $[T(i\omega)]$, is described in section 5.3.

5.1. Scaling

As a first step within the data analysis, the raw acceleration FRF is scaled with the ratio of stabilising and moving masses (μ), to get the FRFs later used for the PFM analysis. The resulting FRFs are of the form

$$Q_{ij} = \mu \frac{a_{\text{st},i}}{-a_{\text{mv},j}} = \frac{m_{\text{st}} a_{\text{st},i}}{-m_{\text{mv}} a_{\text{mv},j}} \quad i,j = x,z \tag{5.1}$$

After the mass fraction μ has been applied to the measured acceleration FRFs, a force correction factor must be applied to the FRF signal. The force correction factor is an FRF that relates the force measured using the single-axis accelerometer on the moving mass to the actual force generated by the shaker and is necessary because of the mounting of the single-axis accelerometer on the moving mass. The shaker force is measured by placing the shaker and its support on a PCB Piezotronics 288D01 Impedance Head[6].

To capture the force over the whole measurement range, a sine-sweep was performed and the acceleration of the moving mass was measured using the accelerometer. During testing, it was found that the tension on the accelerometer cable influenced the shaker's behaviour. Therefore measurements using the LSV were performed to characterise the effect of the accelerometer cable on the moving mass force. An overview of the setup used to determine the FRFs of the shaker force is shown in Figure 5.1. This figure shows the shaker mounted on the impedance head, with the LSV pointed at the top of the accelerometer such that the LSV and single-axis accelerometer measure the acceleration of the moving mass at the same location. By repeating the sine-sweep measurements 3 times with and without the accelerometer cable, whilst measuring the acceleration of the moving mass with the LSV and the force from the impedance head the FRF used to determine the force correction factor could be measured.

The raw FRF measurements used to determine the correction factor are shown in Figure 5.2. Within the region of interest, 15 Hz to 30 Hz, indicated with the vertical lines, it can be seen that the effect of the cable on the shaker response is negligible, as the FRF responses with and without cable are equivalent. However, looking at the FRFs in Figure 5.2, it can be seen that the force generated by the moving mass is underestimated, which in turn means that the acceleration measured by the single-axis accelerometer and the LSV is lower than the actual acceleration assuming Newton's second law.

[6]PCB Piezotronics Model: 288D01 | Mechanical Impedance Sensor `https://www.pcb.com/products?model=288d01` [accessed 12 October 2022]

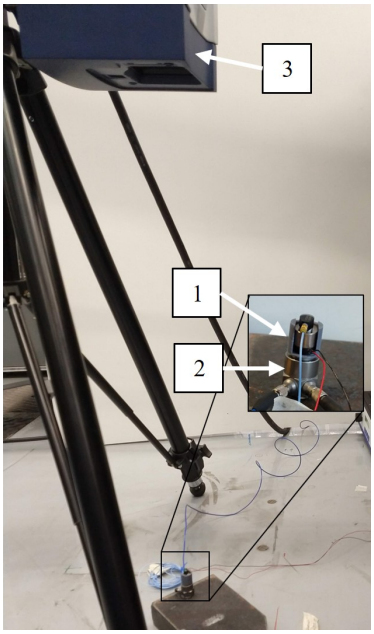

Figure 5.1: Shaker calibration setup. 1: Shaker assembly, 2: Impedance Head (PCB Piezotronics 288D01), 3: Laser scanning vibrometer

The force correction factor, F_{ij} is created by smoothing all measured FRFs using a gaussian filter. The smoothed shaker force FRFs are averaged at every frequency to create a single FRF F_{ij}, which is applied to the mass-corrected transfer function Q_{ij} to create

$$T_{ij} = Q_{ij} \cdot F_{ij} = \frac{m_{\text{st}} a_{\text{st},i}}{m_{\text{mv}} a_{\text{mv},j}} \cdot \frac{m_{\text{mv}} a_{s,c}}{F_{\text{ip}}} \quad i,j = x,z \tag{5.2}$$

which is a frequency-dependent complex value, where F_{ip} is the average of all measured impedance head forces and $a_{s,c}$ is the averaged acceleration from all performed measurements.

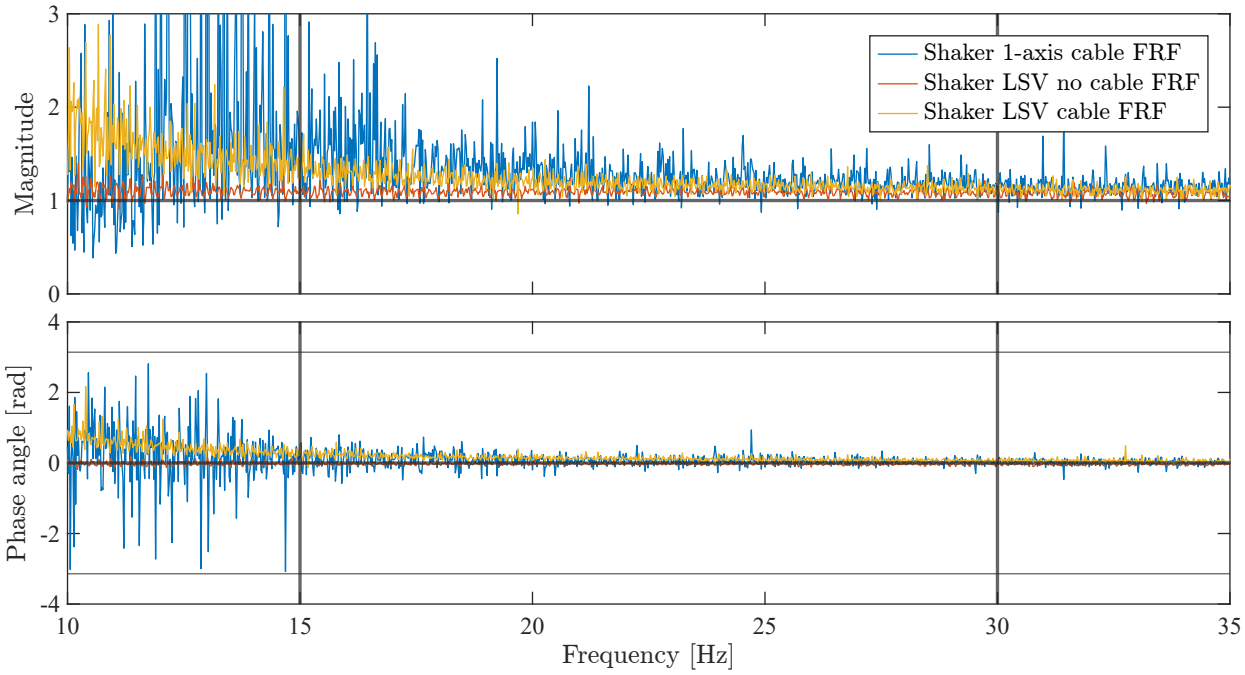

Figure 5.2: Shaker force FRF: $F_{\text{correction}}/F_{\text{impedance head}}$

5.2. Data Smoothing

To be able to use the measured FRFs in the transfer function matrix, $[T(i\omega)]$, a gaussian filter is applied directly to the complex FRF signal such that the noise in the signal is reduced, and the resulting complex number at each frequency can be used to create $[T(i\omega)]$. Examples of the performed smoothing are shown in Figure 5.3.

Specifically looking at the figures with the z-excitation, Figures 5.3a and 5.3b, it can be seen that the noise in the signal is minimal, which is supported by the high coherence values shown in Figure 5.4. Figures 5.3c and 5.3d, which show the response FRFs corresponding to an x-excitation present a response with a lot of noise as is indicated with the low coherence values in Figure 5.4b.

Because of the noisy response in the x-excitation signal, only the magnitude of these signals was smoothed, with the phase remaining as measured, such that the effect of the PCOs, as seen in Figure 5.3c, can be captured. This decision was taken as the smoothing of the complex number resulted in a constant phase and under-valued magnitude that was not able to represent the behaviour of the measured FRF.

5.3. MIMO Parametric Flutter Margin

As stated in section 2.2 the transfer function matrix, $[T(i\omega)]$, needs to be created for every velocity and frequency and is assembled as follows

$$[T(i\omega)] = \begin{bmatrix} T_{xx}(i\omega) & T_{xz}(i\omega) \\ T_{zx}(i\omega) & T_{zz}(i\omega) \end{bmatrix} \tag{5.3}$$

The transfer function matrix only includes the response and excitation in the x- and z-direction. The y-contribution in the transfer function matrix can be disregarded because, in the experimental deflection range, the local spanwise motion of the wing at the shaker's location is not coupled with the fore-and-aft and out-of-plane motion and the local inertial effects of the stabilising parameter in the spanwise and rotational directions are negligible.

Solving for the eigenvalues of the 2x2 matrix $[T(i\omega)]$, two eigenvalues, λ_1 and λ_2 are found. Using the eigenvalues calculated at every frequency, the evolution of the eigenvalues with respect to the frequency can be determined. The eigenvalue evolution, for $\alpha = 0°$ and 2°, of λ_1 is shown in Figure 5.5, and the evolution of λ_2 is shown in Figure 5.6. Figures 5.5 and 5.6 show the eigenvalue evolution for multiple velocities, with each velocity representing a different measurement. From the eigenvectors corresponding to λ_1 and λ_2 shown in **??**, it can be seen that λ_1 is dominated by the response in the x-direction and λ_2 by the response in the z-direction.

As can be seen in Figure 5.5, the λ_1 eigenvalues are very small, and far below a value that can satisfy equation (2.11), and are therefore discarded. The evolution of λ_2 shown in Figure 5.6 shows a clear path followed by the eigenvalues as well as a larger magnitude. Therefore the λ_2 evolution is used to determine the stability of the aeroelastic system.

The λ_2 evolution for α= 0° and 2° is shown in Figure 5.6. In general, three different types of eigenvalue evolutions can be found, which are an evolution with no PCO, an evolution with a PCO and an evolution with a phase flip (phase jumps from $+\pi$ to $-\pi$ or vice versa) and PCO occurring on the real and positive axis. An eigenvalue evolution experiencing a phase flip first crosses $\text{Im}(\lambda) = 0$ axis with the real component being smaller than zero. An example of which is shown in Figure 5.6 for α = 0° and 2° for 25 m/s and 20 m/s respectively. The eigenvalue evolution for $\alpha = 0°$ at 22 m/s shows a PCO with a gain greater than 1, with $\alpha = 2°$ at 20 m/s having a gain less than 1 and a gain greater than 1 for 21 m/s. Finally, 20 m/s for $\alpha = 0°$ shows an eigenvalue evolution that has no PCO, as it does not cross the $\text{Im}(\lambda) = 0$ axis.

To determine the stability of the aeroelastic system, the $\lambda_2 \in \mathbb{R}$ and $\lambda_2 > 0$ are collected for each velocity, with the $\lambda_2 \in \mathbb{R}$ indicating a PCO. By collecting $|\lambda_2| = \lambda_f P_f$ for each velocity, the stability of the aeroelastic system is determined, with $\lambda_2 < 1$ indicating a stable aeroelastic system at the corresponding velocity, and $\lambda_2 > 1$ indicating an unstable system. Using the collected $|\lambda_2|$, the velocity and frequency at which equation (2.11) is satisfied, namely $\lambda_2 = [1.0, 0.0]^\intercal$, can be found. The correspond-

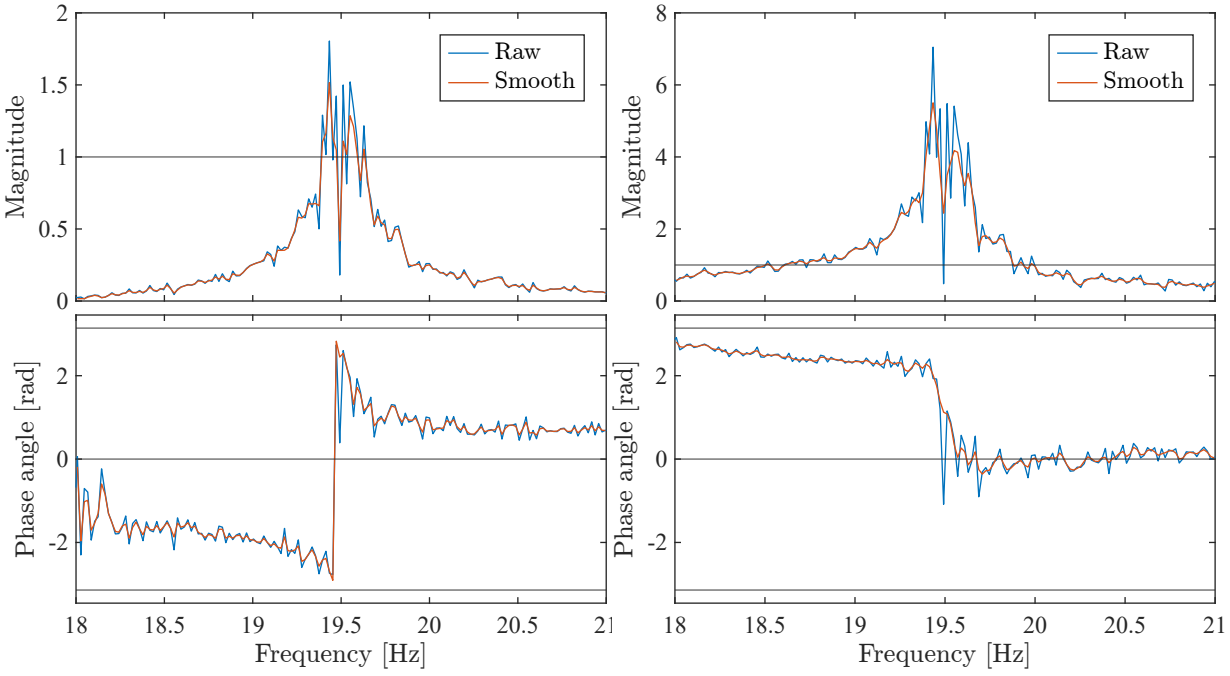

a) FRF x-response, z-excitation

b) FRF z-response, z-excitation

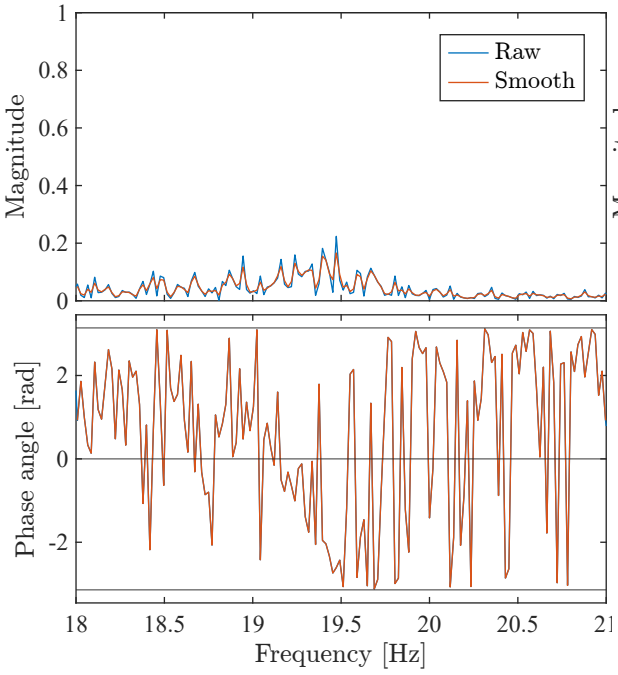

c) FRF x-response, x-excitation

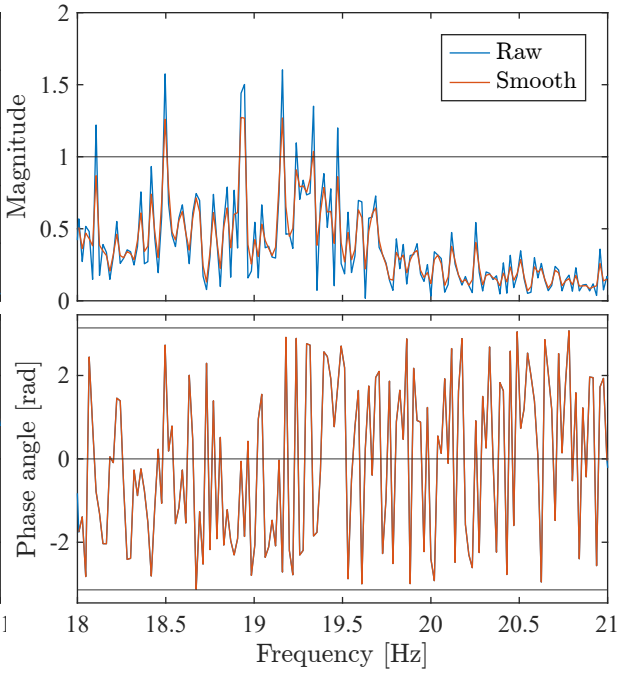

d) FRF z-response, x-excitation

Figure 5.3: FRFs $\alpha = 2°$, 21 m/s

ing z and x participation in the flutter mode can be extracted from the eigenvector plot, an example of which is shown in Figure 5.7.

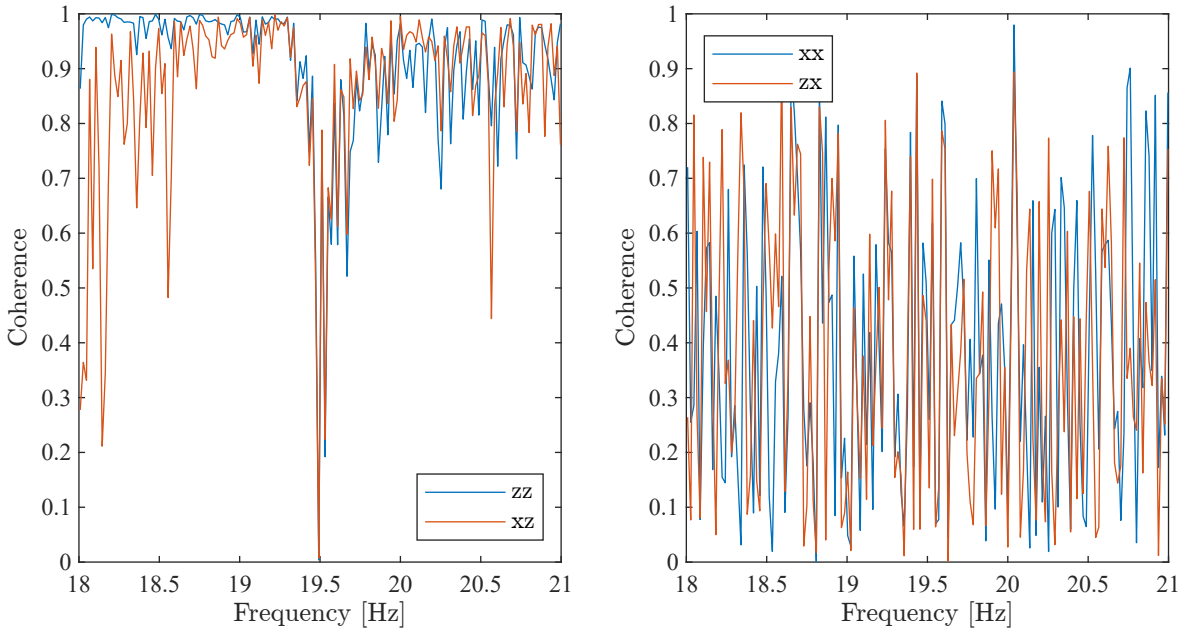

a) Coherence z-response, and x-response due to z-excitation

b) Coherence z-response, and x-response due to x-excitation

Figure 5.4: Coherence $\alpha = 2°$, 21 m/s

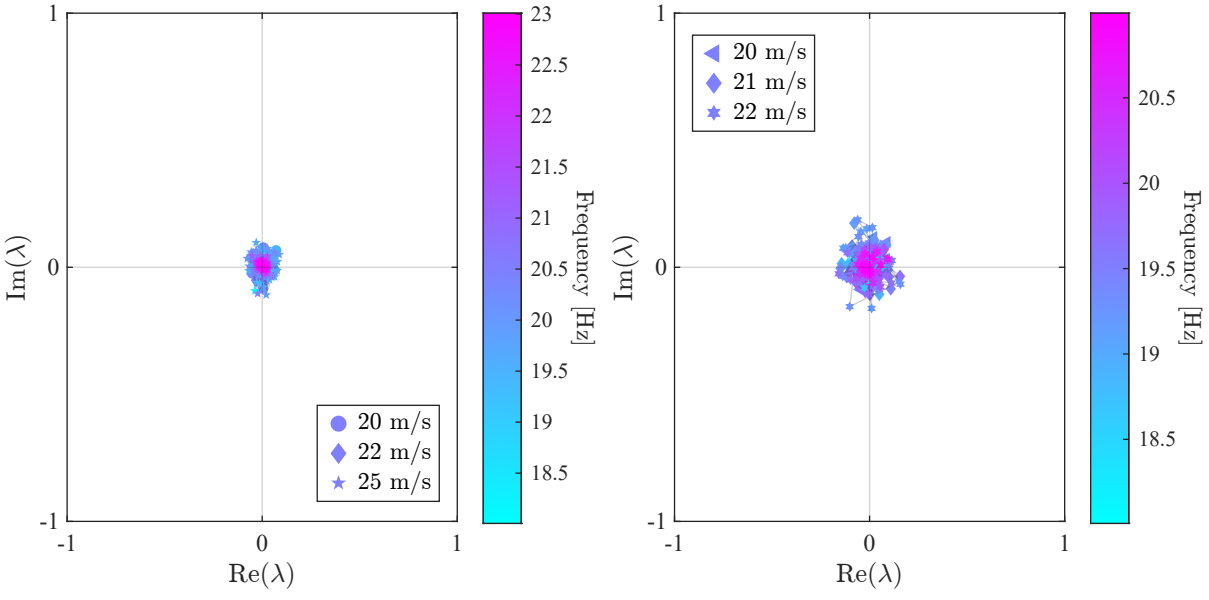

a) $\alpha = 0°$

b) $\alpha = 2°$

Figure 5.5: λ_1 evolution

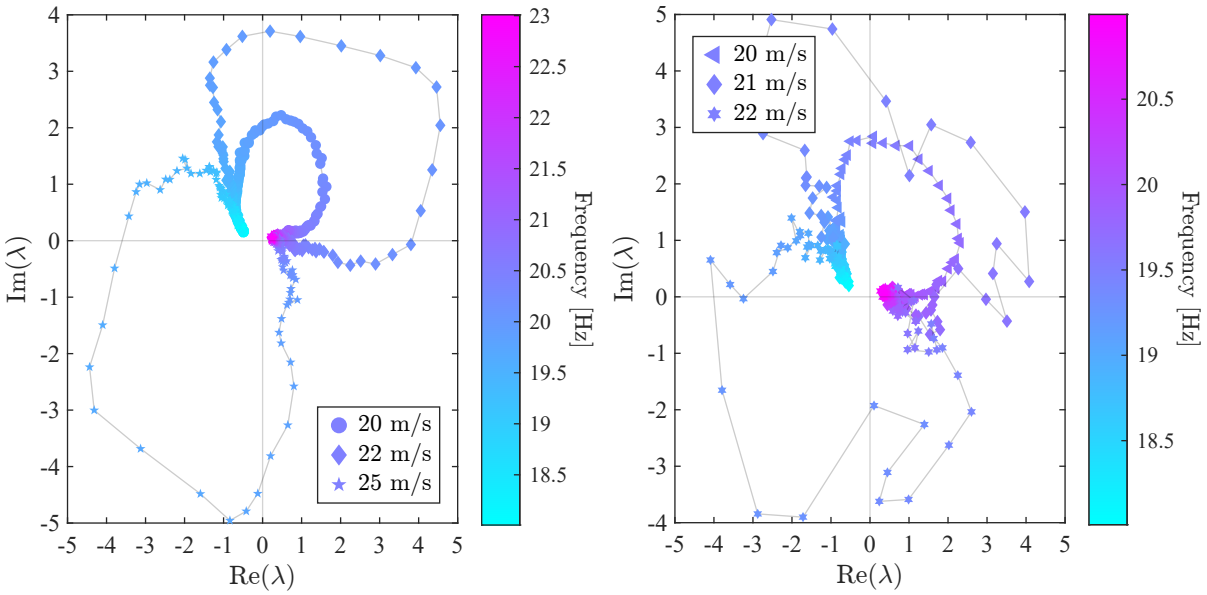

a) $\alpha = 0°$ **b)** $\alpha = 2°$

Figure 5.6: λ_2 evolution

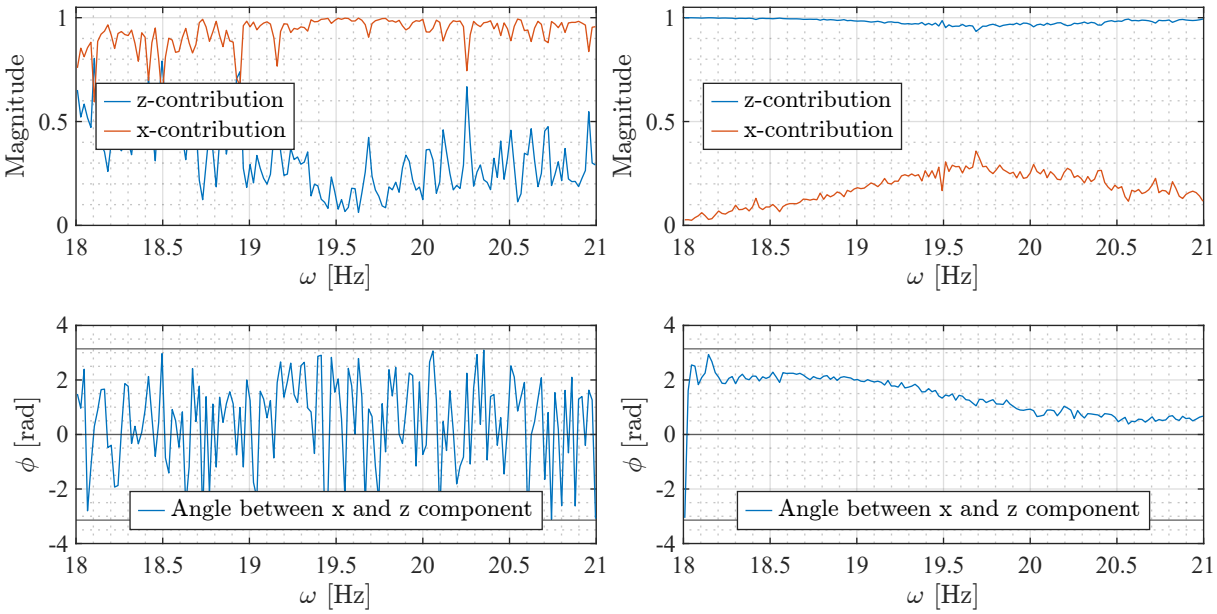

a) Eigenvector corresponding to λ_1 **b)** Eigenvector corresponding to λ_2

Figure 5.7: Eigenvector $\alpha = 2°$, 21 m/s

6

Results

The results obtained during the wind tunnel campaign using the experimental setup and analysed using the data analysis steps described in the previous chapters are presented in this chapter. First, the experimentally determined static deflections are presented in section 6.1, after which the measurement results obtained during direct flutter tests are discussed in section 6.2. This section is followed by section 6.3 which shows the results obtained during the PFM measurements. All the different experimental flutter results are then compared in section 6.4, with the chapter concluding with section 6.5. This section discusses the effect of different excitation levels on the flutter velocity identified using PFM.

6.1. Static Deflection Results

The static tip deflection results during the wind tunnel campaign were measured using the OptiTrack system installed in the OJF at TU Delft. Using reflective tape placed on the tip rod, the OptiTrack camera system can determine the position of the tip[5].

Looking at the tip deflection for an angle of attack range from 0° to 8° and 10° at 18 m/s, which is shown in Figure 6.1, it can be seen that for $\alpha \leq 4°$ the out-of-plane displacement shows differences that are less than 10 %, and above $\alpha = 4°$ the difference between the numerical model and the experimental measurement grows to a maximum of 30 %. The same kind of behaviour is also seen in the spanwise deflection.

Furthermore, looking at the displacement trends in Figure 6.1, it can be seen that the trend of the spanwise displacement follows a parabolic shape, whereas the out-of-plane displacement trend follows a more linear shape. The parabolic trends for the spanwise displacement can be explained by the parabolic shape that the wing forms when deformed. The linear trend seen for the out-of-plane displacement can be explained by the forces causing the wing to deform being dominated by the out-of-plane direction. This causes the out-of-plane displacement seen by the wing to follow a linear trend.

Looking at the deflection results measured during the PFM tests shown in Figure 6.2, it can be seen that the numerical model underestimates the deflection experienced by the wing at every velocity and angle of attack. After the PFM tests were performed, it was observed that the Oracover Oralight foil applied to the wing came loose at the root on the pressure side of the wing. This resulted in a reduction of the stiffness of the wing, resulting in a larger deflection at a given velocity and angle of attack, which explains the difference between the numerical model and the experimentally measured static deflections.

Furthermore, the reduction in the stiffness of the model also results in a reduced flutter velocity, with this effect being most prominent for non-zero angles of attack, as for $\alpha = 0°$ the stiffness of the wing is dominated by the spar, with the stiffness effects of the skin being minimal. For non-zero angles of attack, the increased deflection causes the first torsion frequency to reduce, leading to a lower flutter velocity.

However, even though the static aeroelastic deflection was larger than modelled and resulted in a

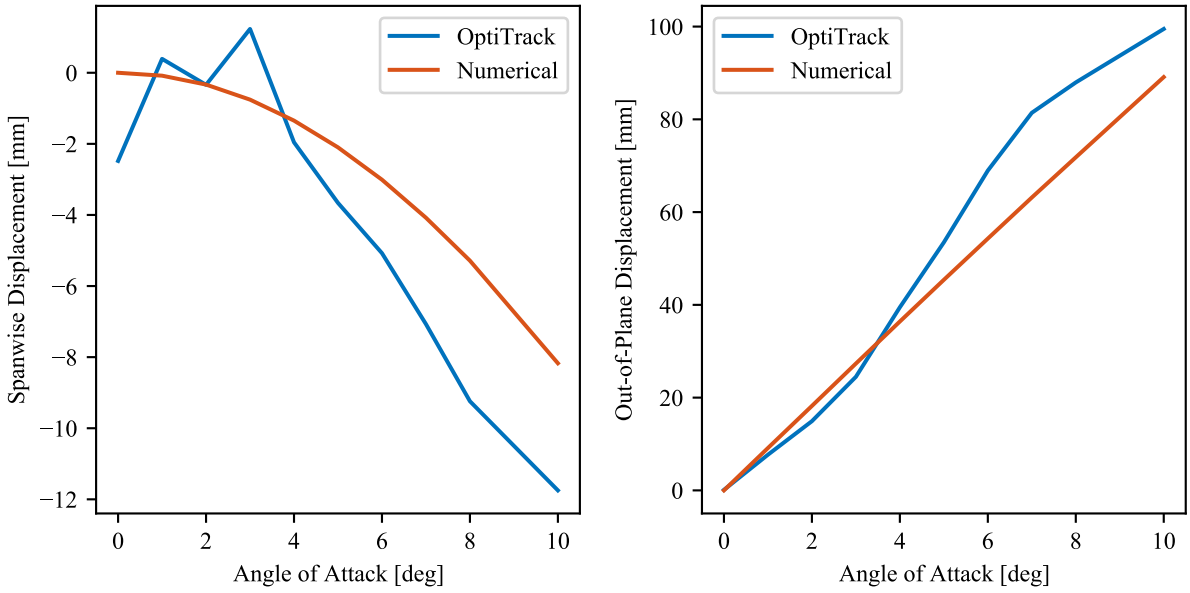

a) Spanwise deflection

b) Out-of-Plane deflection

Figure 6.1: Numerical and experimental tip deflection V = 18 m/s

reduction in flutter velocity, it provided the possibility for PFM to show its ability to positively identify the flutter boundary without the use of a numerical model.

6.2. Direct Flutter Tests

To be able to correlate the PFM results to the actual flutter velocities of the wing, direct flutter tests have been performed with the nominal configuration for $\alpha = 0°$, 2°, 4° and 6°. The direct flutter tests could be safely performed because a very flexible wing model allows for the flutter vibrations to turn into limit-cycle oscillations (LCO), due to the increasing amplitudes of the oscillatory angles of attack, without damaging the test model structure. This happened in the presented test as well as in Drachinsky et al. [27].

Two direct flutter tests were performed for each angle of attack. In the first test, the wind tunnel velocity was slowly increased until the wing would start to flutter which was recorded as the flutter onset velocity. In the second test, the wind tunnel velocity was increased beyond the flutter onset velocity. The wing was allowed to settle on a stable LCO after which the wind tunnel velocity was gradually decreased until the LCO disappeared. This velocity was recorded as the flutter offset velocity. An overview of the obtained flutter onset and offset velocities is presented in Table 6.1. Direct flutter tests were also performed on the PFM configuration, and they exhibited no flutter over the entire wind-tunnel velocity range.

Interesting to note, is that the wing at α = 6° experienced no flutter within the wind tunnel velocity range, even though this was expected based on the numerical results. This can have several reasons. A reason could be the fact that the deflections experienced by the wing could have caused the first torsion mode and second bending modes to flip and not allow the modes to interact with each other for flutter to occur. Another reason could be caused by the implementation of stability criterion within the numerical model, with the actual structural damping coefficient being larger than the assumed zero aeroelastic damping coefficient.

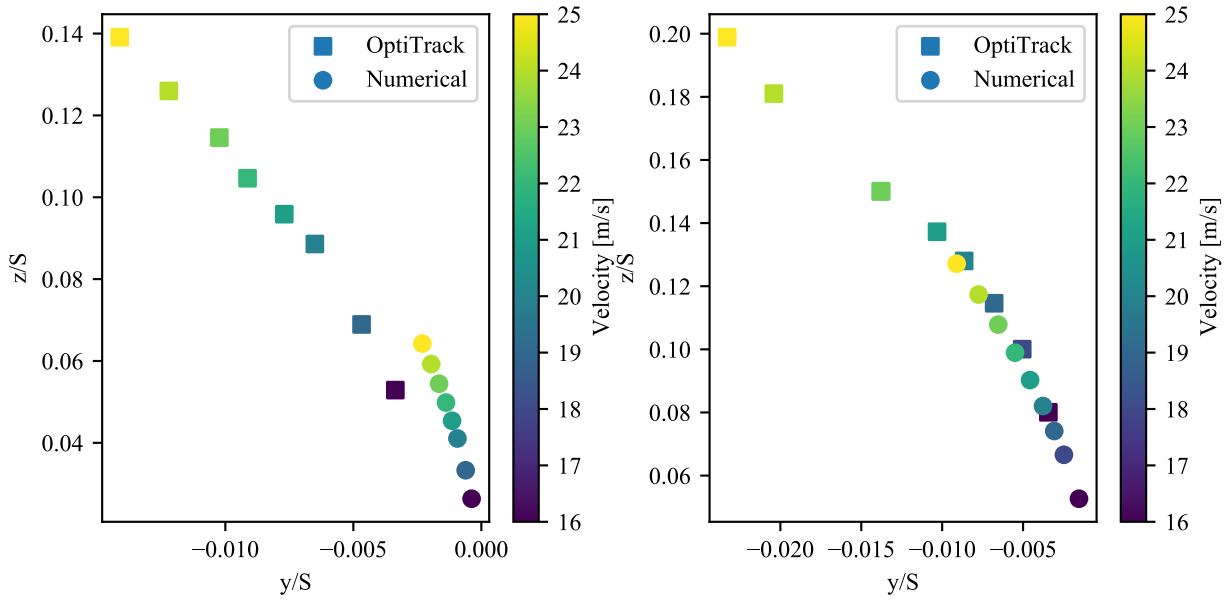

a) Comparison numerical deflection and experimental deflection $\alpha = 2°$

b) Comparison numerical deflection and experimental deflection $\alpha = 4°$

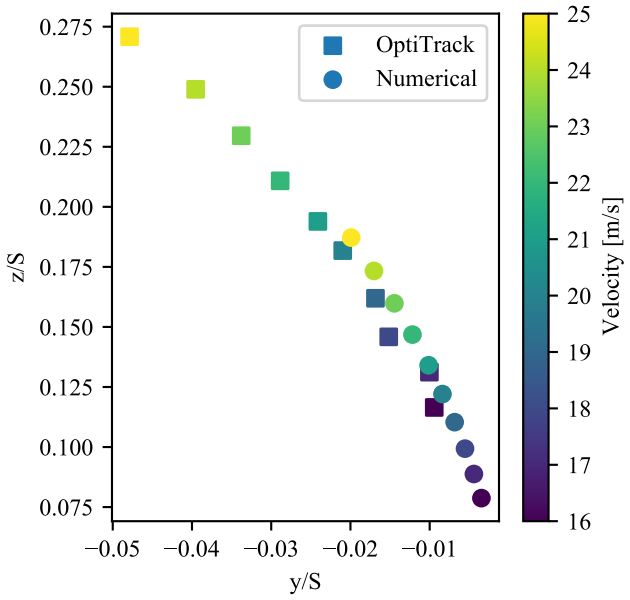

c) Comparison numerical deflection and experimental deflection $\alpha = 6°$

Figure 6.2: Numerical and experimental deflection

Table 6.1: Direct flutter test results of the nominal configuration

α (°)	Onset (m/s)	Offset (m/s)	LCO frequency (Hz)
0	24.2	21.5	20.3
2	21.6	21	19.4
4	21	19.5	19.2
6	> 29	> 29	-

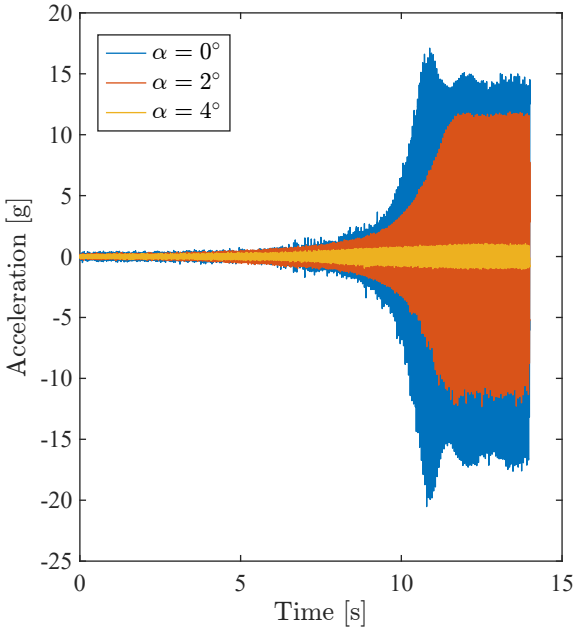

Figure 6.3: Local x-acceleration at tip LE

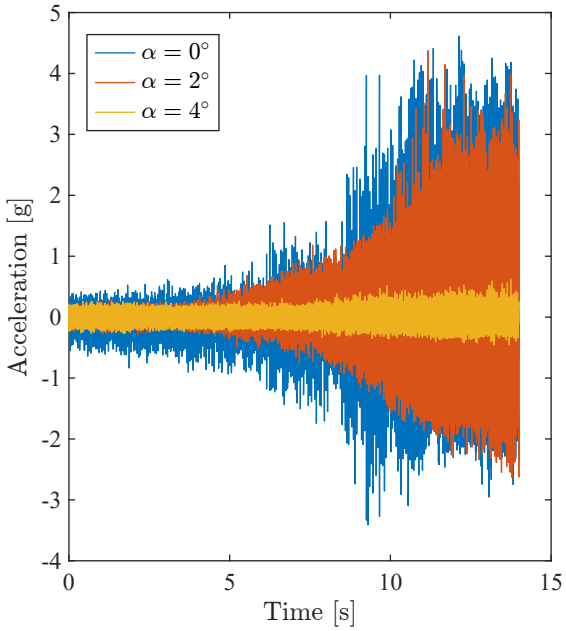

Figure 6.4: Local y-acceleration at tip LE

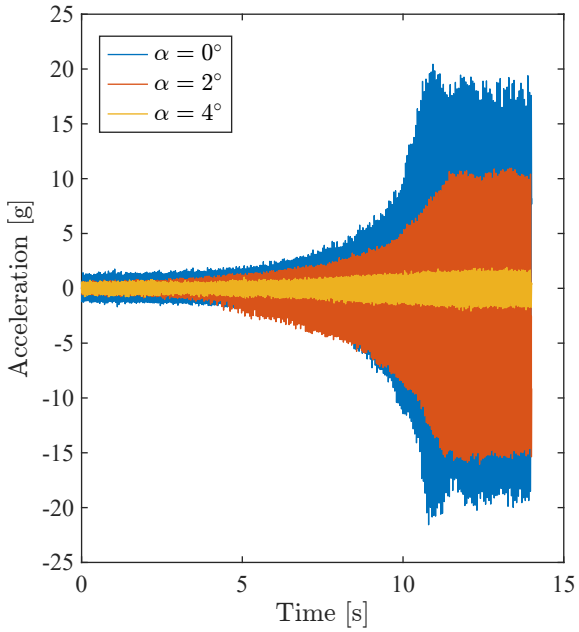

Figure 6.5: Local z-acceleration at tip LE

LCO Response During the direct flutter test, the response of the wing was measured using the accelerometers placed throughout the wing. The LCO response as measured by the three-axis accelerometer on the tip LE is presented below, with the measured response for the rest of the accelerometers shown in Appendix B. Looking at all measured accelerations, seen in Figures 6.3 – 6.5 for the x, y and z directions respectively, it can be seen that the response in the local y-direction (spanwise direction) is minimal compared to the response in the local z and x directions.

Looking specifically at the measured LCO response in the local z- and x-directions, it can be seen that an increase in α results in a reduction of the maximum measured acceleration. This behaviour is expected because the geometric nonlinearity causes the flutter frequency to reduce [11]. The amplitudes of the oscillations are reduced with increasing deflection, as the flutter mechanism becomes

more moderate at large angles of attack. This effect is indicated by the maximum value of the hump peak in Figures 4.12–4.15.

6.3. PFM Results

Within this section, the different results obtained from the PFM tests are presented. First, the gain and PCO frequencies are presented, after which the flutter modes identified using PFM are discussed. Finally, the eigenvectors, which represent the flutter mode at the location of the stabilising mass are presented.

6.3.1. Gain and Phase Cross-Over Frequency

Using the data analysis steps described in chapter 5, the phase cross-over frequency and corresponding gain at each velocity can be determined, which results in Figures 6.6 to 6.8 that show the SISO and MIMO PFM results for $\alpha = 0°$, 2° and 4° respectively. The measurement results can be split into two different datasets, with the first dataset containing a phase cross-over and the second dataset containing phases of less than 10°, but no zero phase crossing, which is indicated using a dashed line. The vertical dashed lines are used to indicate the boundaries of the different datasets. The phase cross-over dataset contains two types of results, one where only a phase cross-over is found and one where both a phase flip and a phase cross-over on the positive real axis are present within the signal. Within the phase cross-over region, the gain is first increasing, and after a certain velocity, the magnitude drops below 1 again. The drop in gain is a characteristic of an eigenvalue evolution with a phase flip and PCO and is caused by the phase flip in the $T_{zz}(i\omega)$ FRF, which leads to a higher phase cross-over frequency.

The PFM results for $\alpha = 0°$ in Figure 6.6, show that the SISO and MIMO PFM methods provide the same gain and cross-over frequency results. This is expected, as $\alpha = 0°$ is the limit case with the wing experiencing no static deflections, and therefore, no coupling between the x and z directions is expected.

Looking at the PFM results for non-zero α, shown in Table 6.2, it can be seen that the MIMO and SISO PFM methods exhibit an increasing difference in the flutter velocity V_f, up to a maximum of 4.4 % for $\alpha = 6°$. The difference in PCO frequency, ω_{pco}, between MIMO and SISO is also increasing with increasing α, and it reaches a maximum of 2 % for $\alpha = 6°$. In general, it can be stated that the MIMO PFM method provided a slightly higher flutter velocity, and lower PCO frequency.

Looking specifically at the PFM results for $\alpha = 6°$ in Figure 6.9, it can be seen that no direct flutter onset and offset velocities have been found, as indicated in the previous section. However, both the SISO and MIMO PFM results indicate that flutter is occurring around 19 m/s, with the numerical model predicting the flutter onset at 21 m/s. The identification of flutter using the PFM method, and not using direct flutter testing is most likely caused by the fact that the flutter mechanism is occurring within the aeroelastic system, however, the flow can not provide sufficient energy needed to start the flutter process, which often occurs with very moderate flutter mechanisms. Another possibility is that the flutter mechanism at $\alpha = 6°$ is so moderate that the respective LCO is hidden in the turbulence noise, leading to the detection of flutter using the PFM method but not through direct flutter testing.

Another way to present the PFM results is given in Figure 6.10, which shows the amount of mass that needs to be added to the nominal configuration to reach its flutter boundary for the MIMO PFM results. This alternative way of representing the flutter margin is valid for both SISO and MIMO PFM. At the flutter boundary of the nominal system, the value for $\Delta p_f = 0$. For MIMO PFM, the value of Δp_f can be calculated using [21]

$$\Delta p_{f,i} = p_f \left(1 - \frac{1}{\lambda\left(\omega_{\text{pco},i}\right)}\right) \tag{6.1}$$

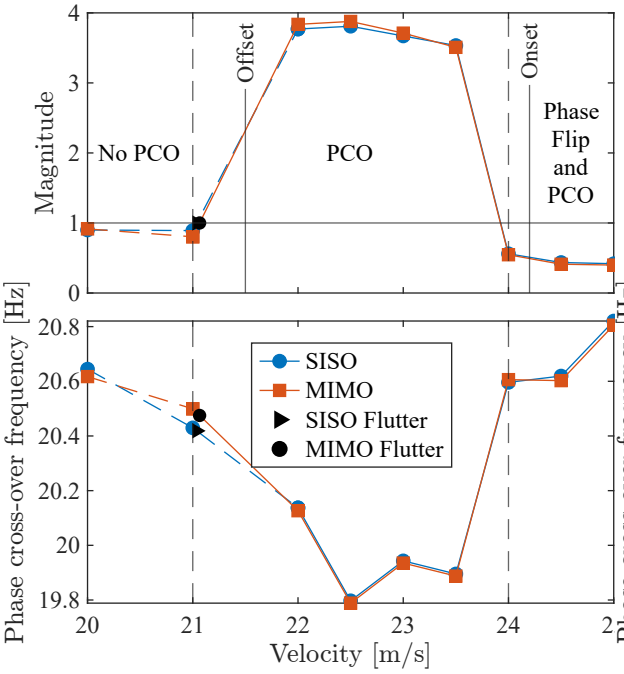

Figure 6.6: Comparison SISO vs. MIMO $\alpha = 0°$

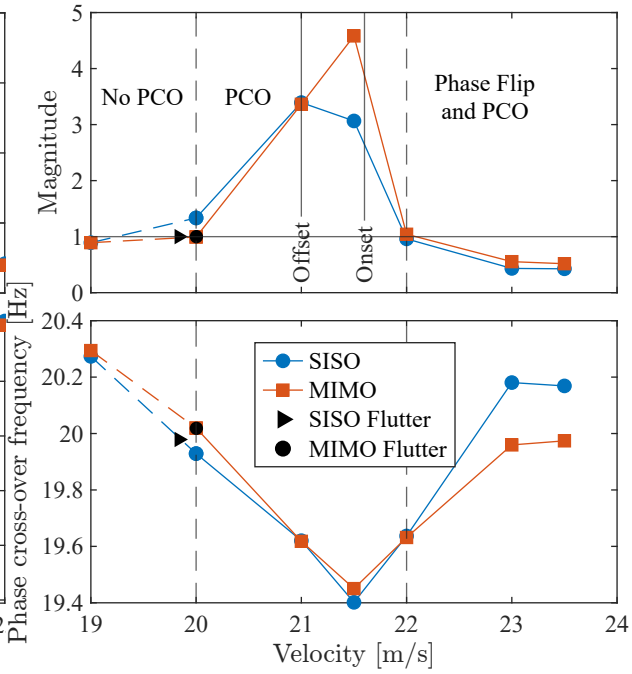

Figure 6.7: Comparison SISO vs. MIMO $\alpha = 2°$

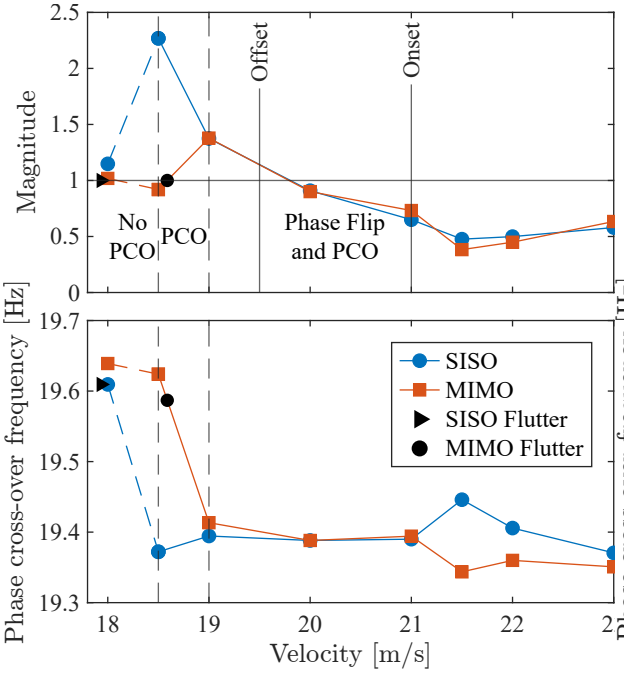

Figure 6.8: Comparison SISO vs. MIMO $\alpha = 4°$

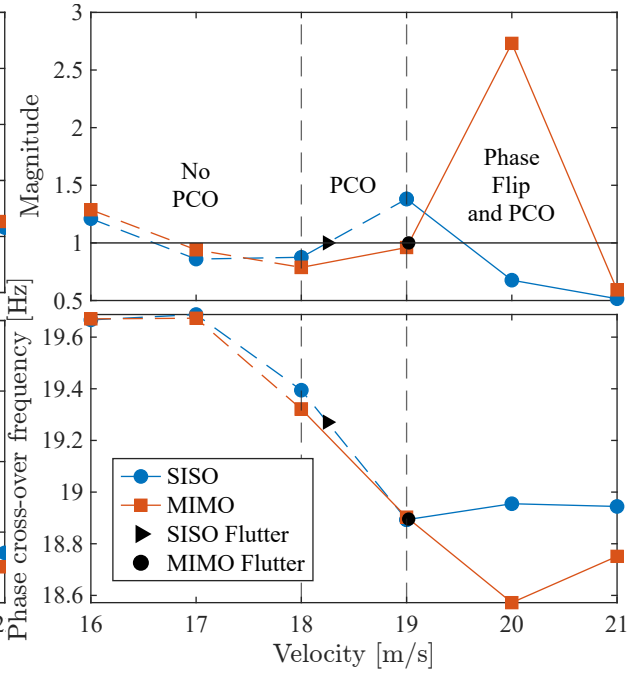

Figure 6.9: Comparison SISO vs. MIMO $\alpha = 6°$

6.3.2. Flutter Modes

Using the measured accelerations during the direct flutter tests and the FRFs measured during the PFM tests the flutter shapes as measured directly and through the PFM results can be compared. The PFM flutter modes were determined by calculating the operational deflected shape (ODS) at the PFM-identified flutter frequency using the FRFs obtained during the PFM test campaign.

The comparison for the dynamic behaviour for $\alpha = 0°, 2°, 4°$ is shown in Figures 6.11 - 6.13 for phase angles 0°, 90°, 180° and 270° along the flutter period, with the dynamically deformed structure indicated

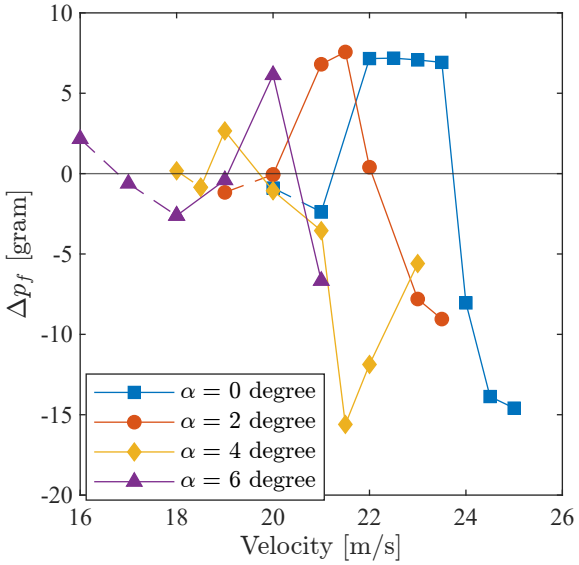

Figure 6.10: Δp_f for all α's

with the black lines and markers with the dynamically undeformed structure being indicated with the light grey lines and markers.

Looking at the full dynamic motion of the flutter shape, both the direct flutter test, MIMO PFM and SISO PFM results show a similar flutter shape, with the second bending mode and first torsion mode being identifiable. When looking at the markers closest to the tip rod, which are located on the fourth and fifth line from the root, it can be seen that the second bending mode and first torsion mode show a phase difference, as the displacement seen by these markers is influenced by both second bending and first torsion in different amounts at the phases shown. Looking further at the dynamic flutter shapes up to $\alpha = 6°$ shown in Figure 6.14, it can be seen that flutter shape is dominated by the first torsion mode, with the contribution of the second bending mode to the dynamic shape decreasing with increasing α. The decrease in the contribution of the second bending mode is caused by the increase in deflection, with the movement in the local x-direction starting to play a more important role.

Coming back to the full dynamic flutter mode, for $\alpha = 0°$ - $4°$ it can be seen that the deformed shape at 0° and 180° phase shows the main motion of the wing to be in the opposite direction, which is true for both the MIMO and SISO PFM flutter modes. To be able to quantify the comparison of the flutter modes as identified using MIMO PFM, SISO PFM and direct flutter tests, the modal assurance criterion (MAC_{ODS}) value was calculated, with the acceleration measured at each accelerometer position being used as a DOF of each shape. For the comparison between the MIMO PFM flutter modes and the direct flutter test flutter modes, the calculated MAC_{ODS} value for $\alpha = 2°$ was 0.76, with the MAC_{ODS} values for $\alpha = 0°$ and 4° being equal to 0.78 and 0.75 respectively. For the comparison between the SISO PFM flutter modes and the direct flutter test flutter modes, the MAC_{ODS} value was 0.72, 0.78, 0.67 for $\alpha = 0°$, 2° and 4° respectively. Because of the high MAC values, the dynamic flutter modes identified through MIMO and SISO PFM are in good agreement with the dynamic flutter mode measured during direct flutter testing.

6.3.3. Eigenvectors

As the gain and phase cross-over frequencies are derived from the eigenvalues of the $[T(i\omega)]$ matrix given by equation (5.3), the corresponding eigenvectors may also be found. From an eigenvector, the relative gain and phase between the directions of motion of the mass can be determined. In the case of an undeformed wing, the coupled motion found using the eigenvector corresponding to λ_2 is dominated by the z-component, with the x-component being negligible. When the angle of attack is increased, the static deflections experienced by the wing are increased, which results in an increased coupling between the in-plane motion and the torsional motion of the wing. The effect of increased

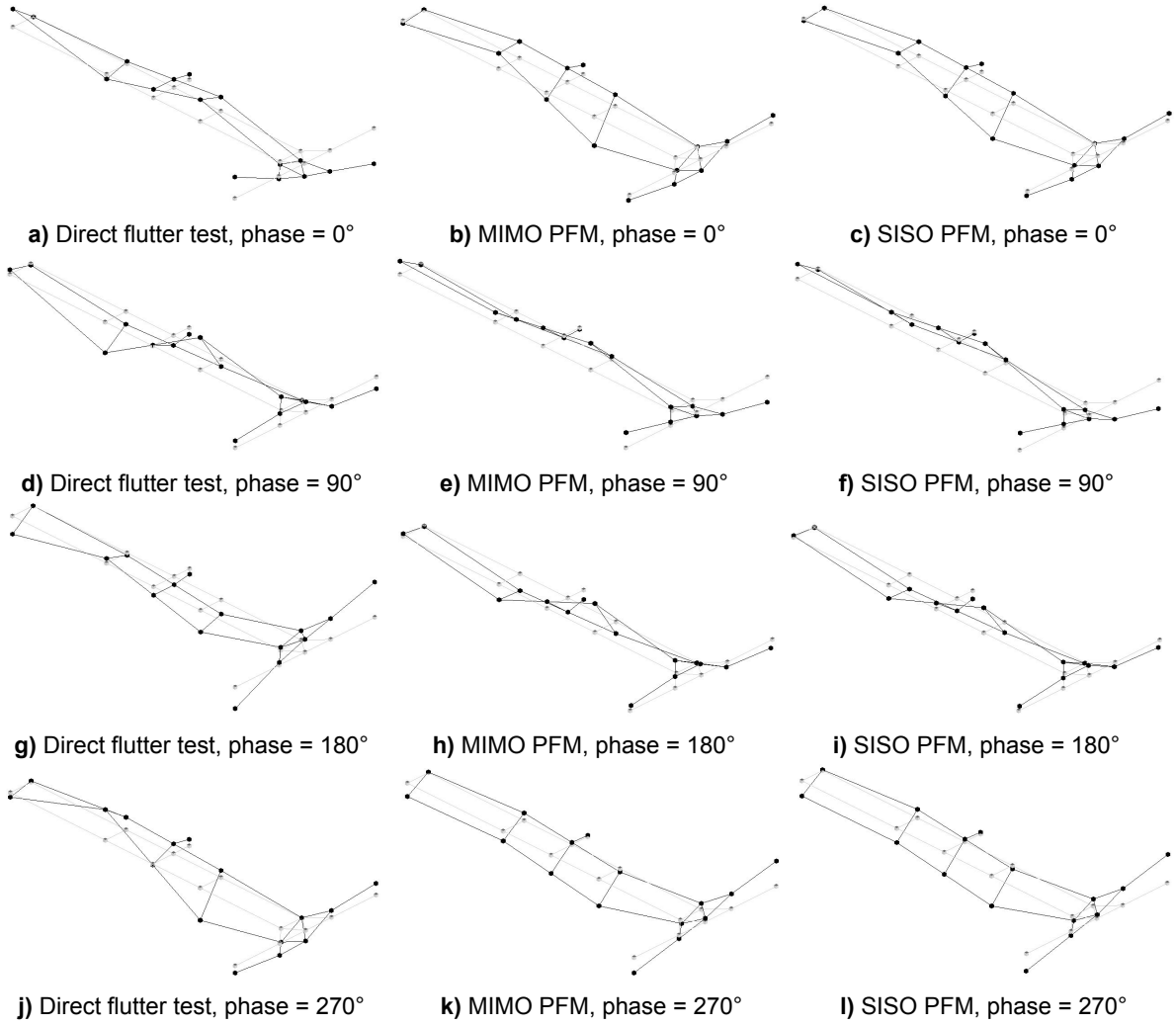

Figure 6.11: Dynamic flutter mode shape comparison, $\alpha = 0°$, looking upstream

coupling with increasing angle of attack at 20 m/s can be seen in Figure 6.15 for $\alpha = 0°$, 2° and 4° respectively. Looking at the eigenvector for $\alpha = 0°$ it can be seen that the x-component is not equal to zero, as would be expected in this limit case, but has a maximum value of 0.2, which might have been caused by the slight wing bending deformation caused in previous experiments, manufacturing imperfections or oscillating drag induced by the angle of attack oscillations.

Specifically looking at the coupling at or around the measured flutter boundary shown in Figure 6.16, it can be seen that the x-contribution for $\alpha = 0°$ remains around 0.2 independent of the velocity, which is as expected, as the wing is not deformed. Looking at the coupling for $\alpha = 2°$ and 4° a clear peak in the x-contribution can be seen and is found close to the LCO frequency of the nominal system. The peak in x-contribution can be explained because when the second bending – first torsion flutter mechanism is approached, the bending and torsion modes couple, resulting in an increased coupling in the z- and x-directions.

As stated previously in Section 2.2, the eigenvector found from the $[T(i\omega)]$ matrix and corresponding to λ_2 shows the flutter mode at the location of the stabilising parameter based on the measured response. Using the vertical lines in Figure 6.16, which indicate the MIMO PFM identified PCO frequency, the flutter mode can be determined by looking at the magnitudes of the x and z components. Furthermore, at the flutter velocity and frequency, the eigenvector shows the required response of the aeroelastic system to cancel the input, which indicates the flutter boundary of the nominal system.

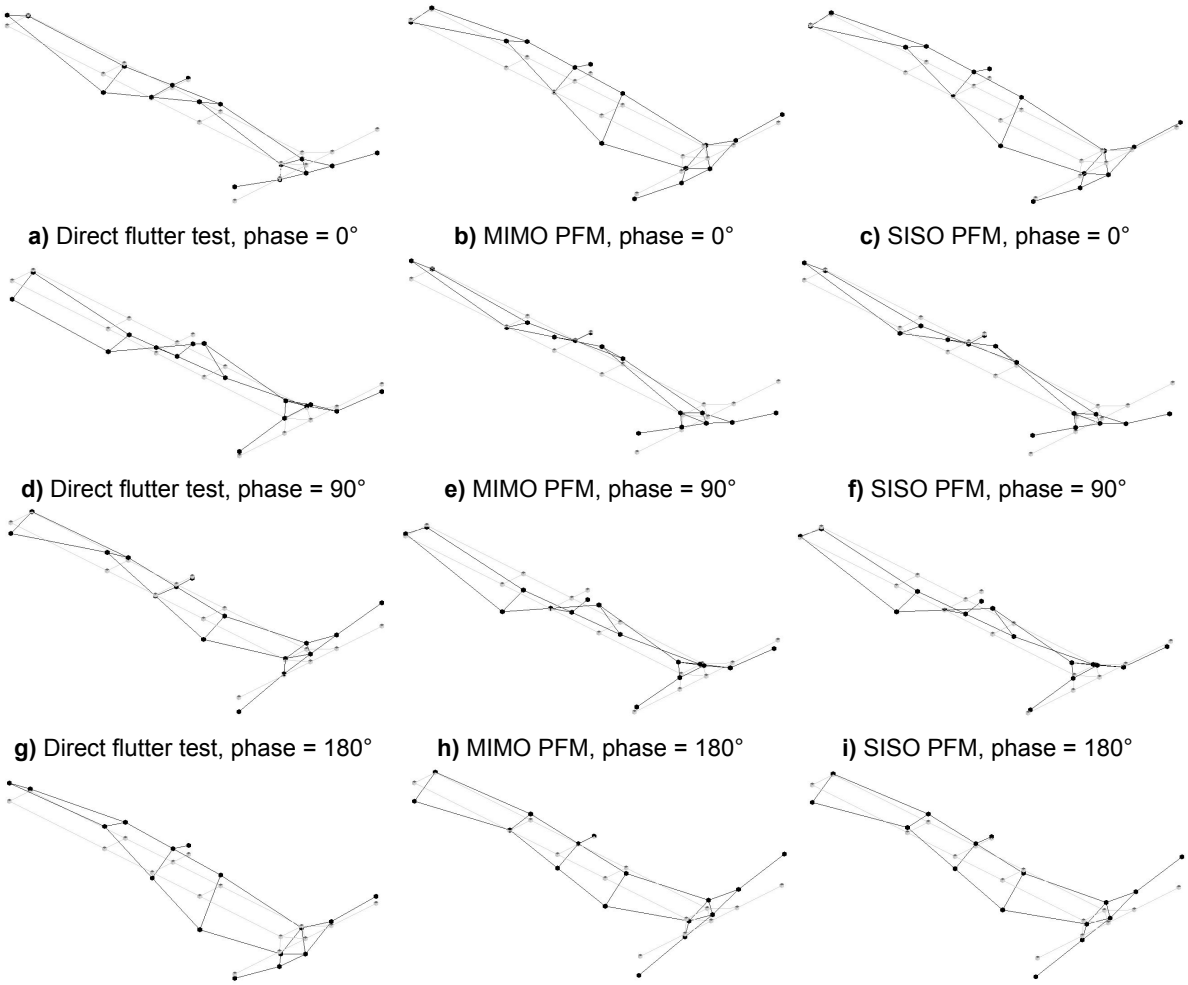

a) Direct flutter test, phase = 0° **b)** MIMO PFM, phase = 0° **c)** SISO PFM, phase = 0°

d) Direct flutter test, phase = 90° **e)** MIMO PFM, phase = 90° **f)** SISO PFM, phase = 90°

g) Direct flutter test, phase = 180° **h)** MIMO PFM, phase = 180° **i)** SISO PFM, phase = 180°

j) Direct flutter test, phase = 270° **k)** MIMO PFM, phase = 270° **l)** SISO PFM, phase = 270°

Figure 6.12: Dynamic flutter mode shape comparison, $\alpha = 2°$, looking upstream

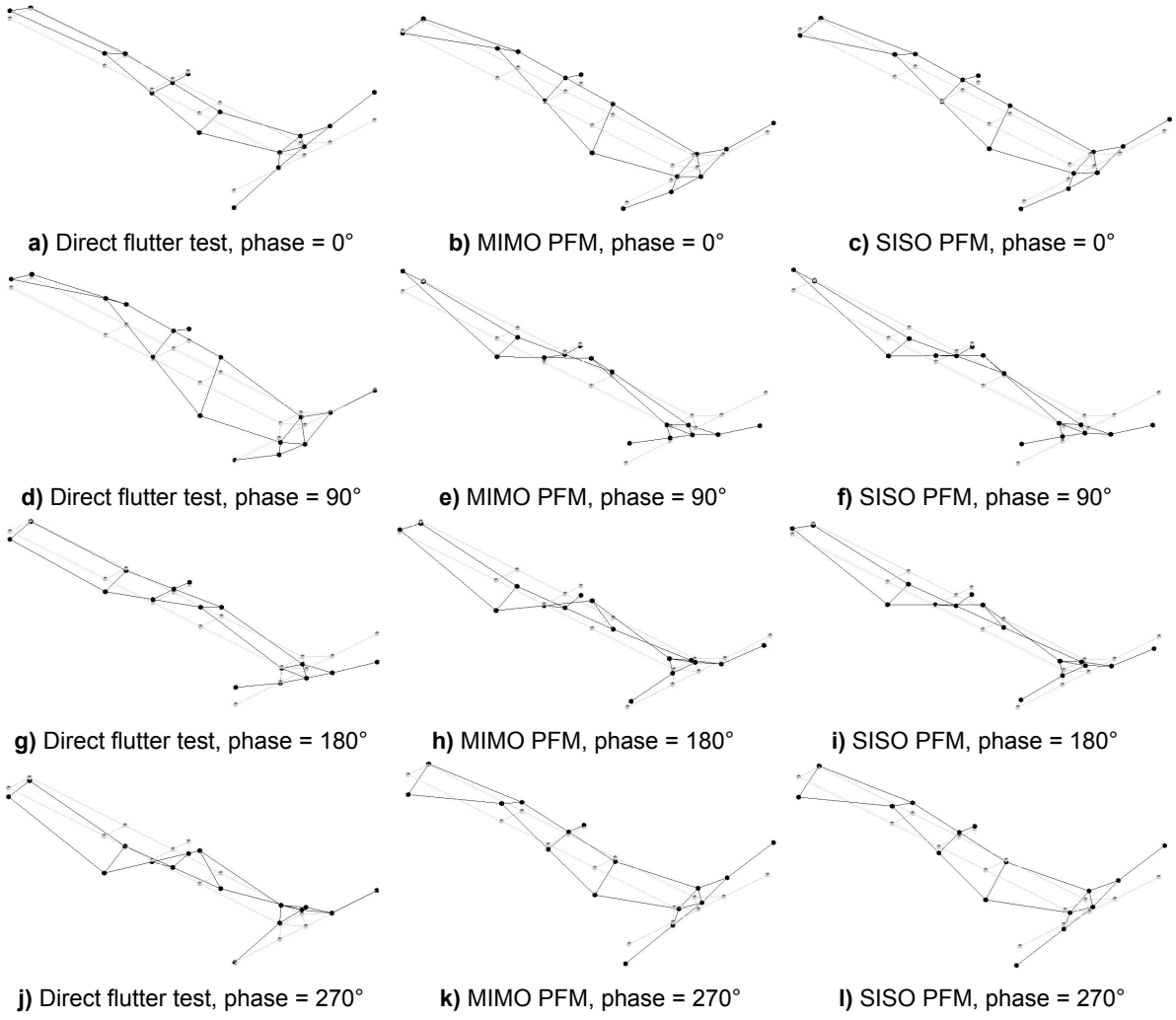

a) Direct flutter test, phase = 0° **b)** MIMO PFM, phase = 0° **c)** SISO PFM, phase = 0°

d) Direct flutter test, phase = 90° **e)** MIMO PFM, phase = 90° **f)** SISO PFM, phase = 90°

g) Direct flutter test, phase = 180° **h)** MIMO PFM, phase = 180° **i)** SISO PFM, phase = 180°

j) Direct flutter test, phase = 270° **k)** MIMO PFM, phase = 270° **l)** SISO PFM, phase = 270°

Figure 6.13: Dynamic flutter mode shape comparison, $\alpha = 4°$, looking upstream

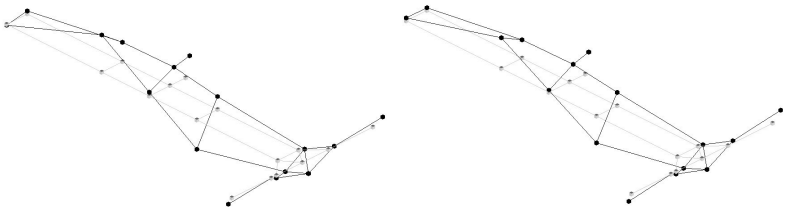

a) MIMO PFM, phase = 0°

b) SISO PFM, phase = 0°

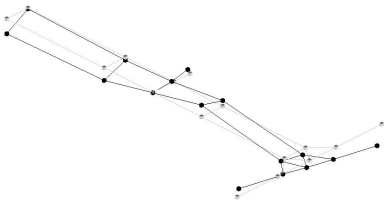

c) MIMO PFM, phase = 90°

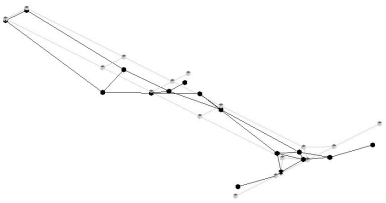

d) SISO PFM, phase = 90°

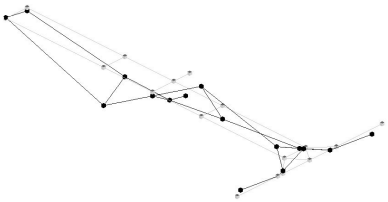

e) MIMO PFM, phase = 180°

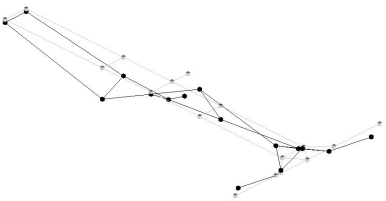

f) SISO PFM, phase = 180°

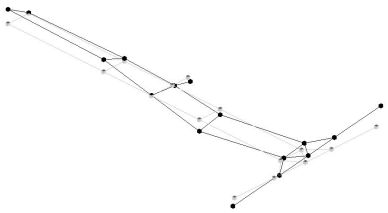

g) MIMO PFM, phase = 270°

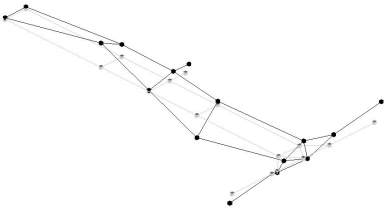

h) SISO PFM, phase = 270°

Figure 6.14: Dynamic flutter mode shape, $\alpha = 6°$, looking upstream

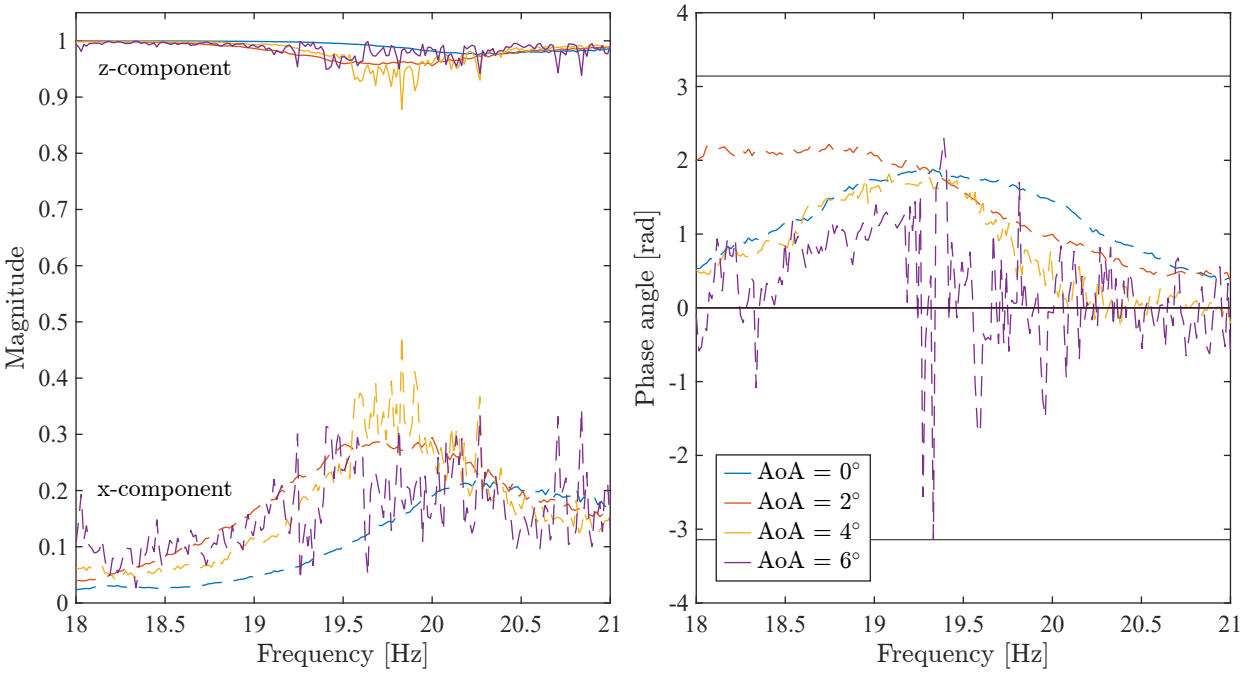

Figure 6.15: Eigenvector at 20 m/s

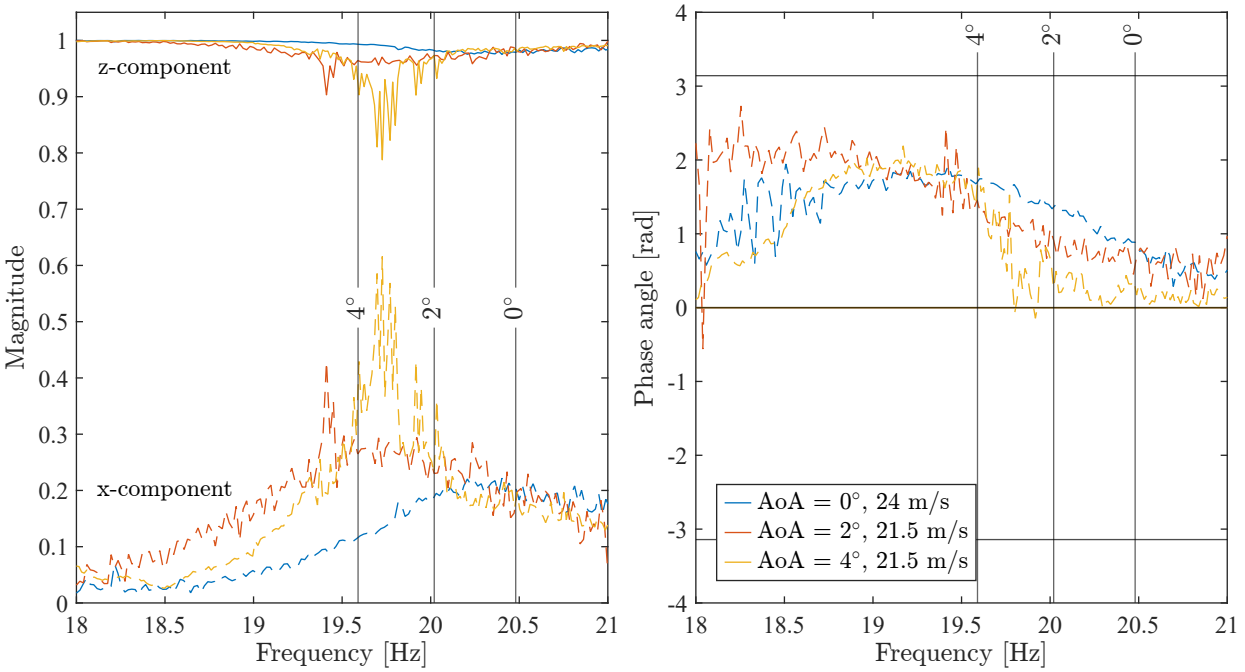

Figure 6.16: Eigenvector at flutter onset. Vertical lines indicate MIMO PFM PCO frequency

6.4. Comparison

Following the SISO and MIMO PFM results discussed above, a comparison between the SISO and MIMO PFM results, direct flutter results and numerical results can be presented. An overview of the different results is shown in Table 6.2, and it shows that the nominal flutter velocities of the MIMO and SISO PFM methods are up to 20 % lower than the direct flutter onset velocities, but only 4.8 % (MIMO) and 8.2 % lower than the direct flutter offset velocities. A visual presentation of the different velocities is shown in Figure 6.17, with the PFM results shown in this figure corresponding to the MIMO PFM results.

Looking at the PCO flutter frequencies, both the SISO and MIMO PFM results show differences of less than 0.9 % for $\alpha = 0°$, 3.2 % for $\alpha = 2°$ and 2 % for $\alpha = 4°$. Comparing the PCO flutter frequencies between the SISO and MIMO PFM results, a minimal difference is found for $\alpha = 0°$, which is increasing to 2 % for $\alpha = 6°$.

However, even with these differences, both the SISO and MIMO PFM exhibit a reduction in LCO frequency with increasing static deflections, which is in line with the results found by Tang and Dowell [11].

The difference between the MIMO and SISO PFM results shown in Table 6.2 are caused by the addition of the effects in the x-direction to the MIMO solution, with the SISO PFM method providing good results with considerably less effort. However, the MIMO PFM results give a result that is closer to the directly measured flutter velocities because of the inclusion of the effects of the stabilising mass in the x-direction.

Looking further at Figure 6.17, it can be seen that the FEM model tuned to the GVTs, shows good agreement with the expected flutter onset velocities but also some differences that cause the numerically predicted flutter velocities to be higher than the measured onset velocities.

Table 6.2: Comparison flutter velocity

	Numerical	Direct			SISO			MIMO		
α (°)	(m/s)	Onset (m/s)	Offset (m/s)	ω_f (Hz)	V_f (m/s)	ω_{pco} (Hz)	MAC_{ODS}	V_f (m/s)	ω_{pco} (Hz)	MAC_{ODS}
0	25	24.2	21.5	20.3	21.0	20.42	0.72	21.1	20.48	0.78
2	24	21.6	21	19.4	19.8	19.98	0.78	20.0	20.02	0.76
4	22	21	19.5	19.2	17.9	19.64	0.67	18.6	19.59	0.75
6	21	> 29	> 29	-	18.2	19.27	-	19.0	18.89	-

6.5. Effect of Shaker Excitation

Combing back to the under-identification of the flutter velocity, it is assumed that because of the large vibrations seen during the direct flutter tests, the wing experiences subcritical Hopf-bifurcation and the occurrence of a fold point that is similar to the behaviour observed by Tang and Dowell [11], [29], [30] on highly flexible wings. Hence, the shaker excitation level during the PFM tests can cause flutter to start at lower velocities.

To determine the effect of the shaker excitation force on the flutter margin, the input voltage was lowered from 0.4 V (Gain 1) to 0.2 V (Gain 2) and the FRFs were obtained for a range of velocities between 22 m/s and 24 m/s at $\alpha = 0°$. Looking at Figures 6.18 and 6.19 for 22 m/s and 23 m/s respectively, both the magnitude and phase are influenced by the excitation force. However, when the wing approaches the flutter onset velocity, as shown in Figure 6.20, the difference in FRF behaviour due to different excitation amplitudes becomes negligible.

The presented results suggest that a larger excitation force results in a higher gain amplitude at the cross-over frequency and a higher phase cross-over frequency. However, when the wing approaches

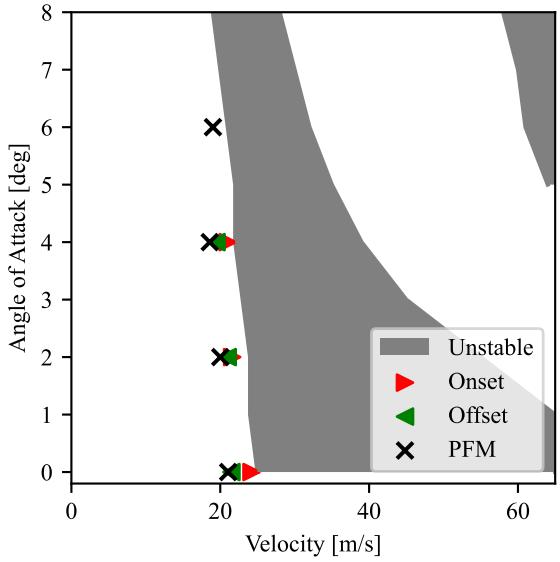

Figure 6.17: Comparison between numerical, direct flutter test and MIMO PFM results

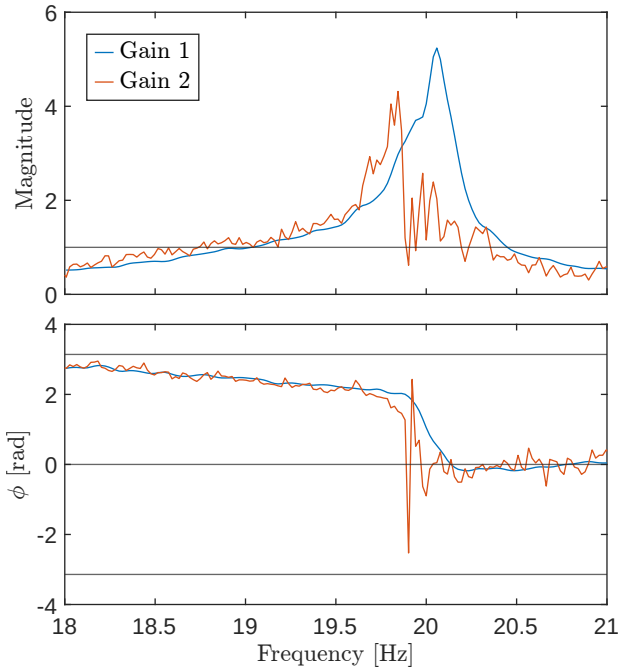

Figure 6.18: SISO z-response to z-excitation with lower shaker excitation V = 22 m/s

the linear flutter onset velocity, the effect of the excitation amplitude becomes small.

Because of the low number of sample points and the shaker design, several uncertainties with respect to the shaker excitation level exist. Therefore, to be able to fully understand the effect of excitation level on the predicted flutter velocity, further investigation into the property of the flutter pod is required. Due to the design of the shaker, its performance as a function of excitation levels should be investigated in more detail first. In addition, the measurements should be repeated at more free-stream velocities and angles of attack. The presented results suggest that a larger excitation force results in a higher gain amplitude at the cross-over frequency and a higher phase cross-over frequency. However, when the wing approaches the linear flutter onset velocity, the effect of the excitation amplitude becomes small.

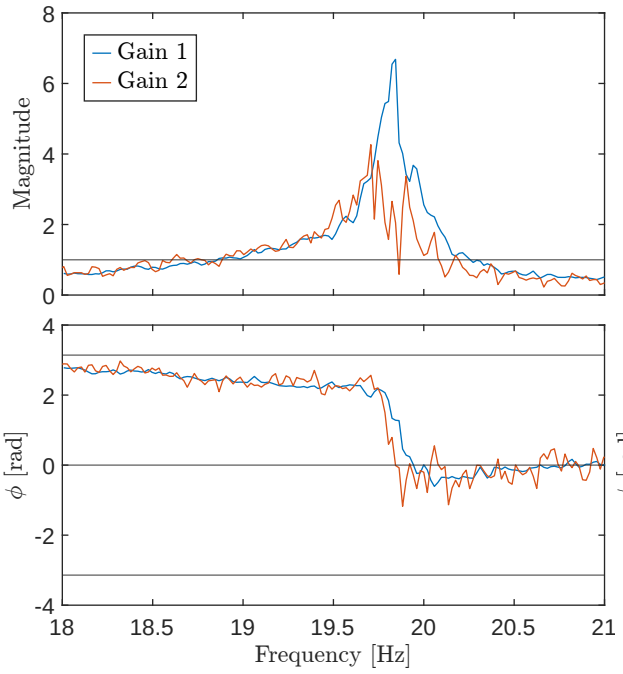

Figure 6.19: SISO z-response to z-excitation with lower shaker excitation V = 23 m/s

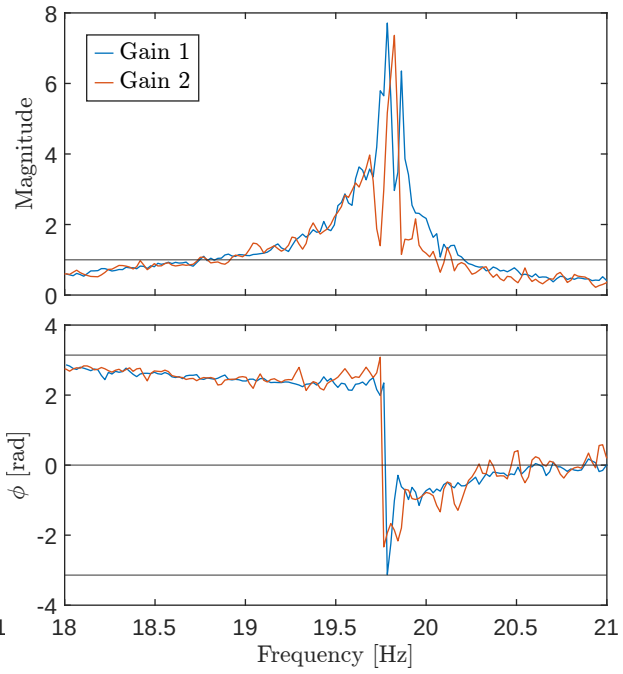

Figure 6.20: SISO z-response to z-excitation with lower shaker excitation V = 24 m/s

Because of the low number of sample points and the shaker design, several uncertainties with respect to the shaker excitation level exist. Therefore, to be able to fully understand the effect of excitation level on the predicted flutter velocity, further investigation into the property of the flutter pod is required. Due to the design of the shaker, its performance as a function of excitation levels should be investigated in more detail first. In addition, the measurements should be repeated at more free-stream velocities and angles of attack.

7

Conclusion and Future Work

The final chapter of this thesis summarises the contribution to the state-of-the-art of this thesis towards safe flutter determination. First, the conclusions based on the experimental results will be presented, which is followed by recommendations and future work.

7.1. Conclusion

The objective of this thesis was to

> *Safely determine the flutter boundary of a wing undergoing large static deflections by the use of the PFM method.*

With this objective, the PFM method was extended such that it could be applied during tests, with a wing experiencing large static deflections, with the flutter boundary parameters identified without actually experiencing flutter. To address this objective, a wind tunnel model based on the Delft Pazy Wing, stabilised by adding a small mass at the mid-span leading edge position, has been designed, manufactured and tested in the wind tunnel.

The presented work shows a successful application of the MIMO PFM method to a highly flexible wing under large initial deflections that positively identified the flutter boundary of the nominal aeroelastic system. For the identification of the flutter boundary no numerical model was used, which shows the potential of the PFM method for performing safer, shorter and consequently cheaper flight tests for the certification procedure of new aircraft configurations.

The experimental results provided three types of signals, from which the PCO frequency and corresponding gain were determined and used for obtaining the flutter frequency and flutter margin of the aeroelastic system.

Using the flutter margins, the SISO and MIMO PFM results were obtained, which identified the flutter velocity of the wing to be lower than the directly measured flutter onset velocity by a maximum of 20 %.

The under-identification with the directly measured offset flutter velocities was significantly lower, with a maximum of 8.2 % for SISO and 4.8 % for MIMO. The differences between the MIMO and SISO PFM results are increasing with angle of attack, α, with the maximum difference of 4.4 % reached at $\alpha = 6°$.

Comparing the PCO flutter frequencies, the difference between the SISO and MIMO PFM methods was also increasing with increasing angle of attack. A maximum difference of 2 % was found between SISO and MIMO PFM, with the difference between the PFM PCO flutter frequency and the flutter frequency determined using the direct tests, reaching a maximum value of 3.2 %.

Using the extracted flutter velocities and frequencies, the flutter shapes were also identified. The flutter shapes identified from MIMO PFM results showed good agreement with the directly measured flutter shape, with the MAC values being greater than 0.75 for all angles of attack.

Even though the MIMO and SISO PFM results showed some differences between their results, both methods identified the reducing flutter velocity and frequency with increasing angle of attack, which is in line with the direct flutter test performed during the wind tunnel campaign. However, within the range of deflections experienced during the test campaign, it can be concluded, that the SISO PFM method was able to identify the flutter offset velocity with larger errors than those of MIMO PFM, but with considerably less effort.

The MIMO and SISO PFM measurements were repeated using a lowered shaker excitation level to determine the effect of the shaker excitation on the identified flutter margin. This was done because it was suspected that the wing experienced subcritical Hopf-bifurcation and fold points similar to the behaviour seen on very flexible wings by Tang and Dowell [11], [29]. The reduced excitation level influenced the FRF behaviour at velocities below the flutter onset velocity, with the magnitude and PCO frequency being lower when far away from the onset velocity. However, the influenced FRF behaviour disappeared closer to the flutter velocity

7.2. Recomendations and Future Work

Within this section, several recommendations that have been determined based on the presented research are shown in subsection 7.2.1. Several steps that can be undertaken to take the presented research further are shown in subsection 7.2.2

7.2.1. Recommendations

Based on the experience gathered during both the design and testing phases, several recommendations can be made.

First of all, in the presented work, a single-axis accelerometer was placed on the moving mass to determine the force provided by the shaker. Due to the oscillation of the shaker, the cable connecting the sensor to the SCADAS acquisition equipment was damaged by fatigue due to the loads placed on the sensor cable. It was also found that due to the method used to limit the shaker's movement, a sensor overload could occur. Because of the complications seen with the current measurement method of the force provided by the moving mass, a recommendation would be to measure the acceleration of the moving mass through a different means than an accelerometer placed on it. This could be done through the use of a hall effect sensor that measures the instantaneous position of the moving mass from which the acceleration can be derived, or a laser could be used to determine the acceleration of the moving mass similar to the method used by a laser scanning vibrometer.

Changing the method in which the acceleration of the moving mass is measured will also allow for the design of a shaker that can provide a true continuous random excitation in all directions of interest simultaneously. A shaker design that can provide excitation to the stabilising parameter in a continuous random fashion in the x, y and z directions is desirable, as it allows for a shortening of the total required measurement time because the measurements in all directions can be performed simultaneously without requiring any change to the experimental setup. Such a shaker design will allow for the development of a full black box PFM testing method that can be applied directly to a wing. This would allow for the opening of the flight envelope to be performed in a small number of tests.

For the data analysis procedure, a recommendation that can be made is the implementation of an adaptive noise filter. Such a filter would allow for a changing smoothing factor within the frequency range, leading to all FRFs having their magnitude and phase behaviour captured in an equivalent way.

A final recommendation would be to use a larger wing. This is because a larger wing will have a higher mass, meaning that the effect of aspects such as the weight of the permanently attached cables becomes less important. The larger wing weight and the larger size will also allow for a more sophisticated shaker designed, based on the previous recommendations, to be embedded within the wing such that the aerodynamic effects of the flutter pod become minimal.

Furthermore, a larger wing could be designed such that the MIMO PFM method is applied to a more conventional first bending – first torsion flutter mechanism.

7.2.2. Future Work

Following on from the presented results, several aspects necessary to be able to expand the understanding and application of PFM further can be derived.

First of all, future work relating to the PFM method will be focused on signal processing and data analysis. Aspects that need to be investigated are the possible relaxation of the phase cross-over and the effect of the phase flip which causes the loss of the phase cross-over. Furthermore, the post-flutter effects on the eigenvalues and eigenvectors used during the analysis need to be investigated, with further investigation of the effects of different levels of excitation on the measured FRFs also needing to be performed.

To support the numerical investigation of the behaviour of the eigenvalues and eigenvectors in the post-flutter regime, the presented numerical model needs to be updated to allow for the modelling of the full dynamic behaviour of the wing, while simultaneously reducing the computational cost required by the numerical model by, for example, representing the wing using a beam model instead of using the full numerical model of the wing.

Furthermore, as was found when comparing the MIMO PFM and SISO PFM flutter velocities, the MIMO PFM results were closer to the directly measured flutter velocities, but not very significantly. This is most likely caused by the placement of the stabilising mass at a mid-span position, where the static deflections are much smaller than at the wing's tip. Therefore, further tests should be performed with masses at places where the different directions are similarly important, such as the wing's tip or under-wing external stores.

A

Ground Vibration Testing

To be able to represent the experimental model numerically, the dynamic properties of the numerical and physical models should be equivalent. Therefore, information on the dynamic behaviour of the wing needs to be obtained, as the different eigenmodes play a role in the flutter mechanism, which is second bending – first torsion. To be able to obtain the dynamic behaviour of the wing, a ground vibration test (GVT) is performed. The methodology behind a GVT is presented in section A.1. After which the procedure used to perform the GVT measurements is shown in section A.2

A.1. GVT Methodology

The ground vibration test is an experimental method which is used to determine the modal model of a structure through modal analysis, which is assumed to be a linear time-invariant (LTI) system [31]. Modal analysis determines the natural frequencies, mode shapes and damping factors of the structure, which form the mathematical modal model of the structure, and is based on the fact that the dynamics of an LTI system can be expressed as a linear combination of the natural frequencies [31]. Further details on the definition and application of Modal Analysis can be found in ”*Modal Analysis*” by He et al. [32]

With the goal of the GVT being the determination of the modal properties of a structure, the frequency response function (FRF) needs to be determined at several measurement points. The FRF is created by measuring the response of the structure due to external excitation. To be able to obtain the structural response, several different methods can be used. One method would be the application of accelerometers to the structure. However, when determining the modal response of a highly flexible structure, the addition of the accelerometers, which function as point masses, influence the eigenfrequencies. Another method that can be used to obtain the structural response is the use of a Laser Scanning Vibrometer (LSV). The LSV uses a laser to measure the structural response at each measurement position.

A.2. GVT Procedure

This section describes the procedure used to set up the GVT measurements and how to analyse the measurement data to obtain the frequencies and damping of each mode.

Set-up of LSV and Modal Hammer To be able to perform the GVT Test, the modal hammer and the LSV need to be set up. The first step in the setup of the LSV is to make sure that the laser is pointing straight towards the test object, and is lined up with the test object. After this, the outlines of the test object need to be set. Followed by setting the coordinate system, and calibrating the laser sensitivity and distance measurement. When all these steps have been performed, the measurement frequency and resolution (frequency steps) can be set. For the GVT measurements, a frequency range of up to 800 Hz has been used.

Using the LSV frequency range and resolution, the measurement time needed to measure a single point is determined. For the Modal Hammer set-up, the interval between hits needs to be greater than the measurement time required by the LSV. Another set-up step for the Modal Hammer is the position. The Position of the Modal Hammer needs to be set such that no double hit is present, and that the load cell in the tip is not overloaded when the wing is struck by the Modal Hammer.

Measurement Mesh Before the GVT measurement can be performed, the points where the measurements need to be taken need to be prescribed. For the out-of-plane GVT, the vibration data was acquired at 24 points. 9 Of these were placed at the leading edge, 9 at the trailing edge, and 6 were placed on the tip rod. When running the GVTs on the configuration with the shroud at the midspan position, an extra measurement point was added to the shroud. For the in-plane GVT, the vibration data was measured at 8 points along the leading edge.

GVT Test During the GVT measurement, the modal hammer hits the test wing at the same location at a fixed interval. The LSV measures the response of the wing at each measurement point. This process is repeated at each measurement point for the set number of measurements of which the average at each point is taken. The average response of the wing at each measurement point is saved as the FRF of the velocity of the wing caused by the force exerted by the modal hammer. FRFs of displacements and accelerations are derived from the velocity FRF.

Modal Analysis (Post Processing) After the GVTs have been performed, the FRFs measured by the LSV need to be exported to a .uff (universal) file such that they can be imported into Simcenter TestLab[7]. Using the FRFs obtained at all measurement points, the frequency range of interest is set after which the stable points (in both frequency and damping) can be selected in the stabilisation plot generated by Polymax. The stable points will coincide with the eigenfrequencies of the structure. Using the stable points, Using the selected stable points, Polymax can calculate the mode shapes, eigenfrequencies and damping corresponding to the stable points. To further refine the mode shapes, the Maximum Likelihood estimation of a Modal Model (MLMM) is used. MLMM allows for the automatic movement of the stable poles to better fit the measured system response. After the mode shapes and eigenfrequencies have been determined, the fitted FRF, which has been generated using the selected points in the stabilisation plot and the MLMM results, can be validated. The fit should be as good as possible, with the smallest error. To get the best fit, several iterations, with a different number of selected points, need to be performed. From the final fit, the required eigenfrequencies, mode shapes and modal damping can be obtained.

[7] Simcenter Testlab `https://www.plm.automation.siemens.com/global/en/products/simcenter/testlab.html` [accessed 18 October 2022]

B

LCO Response

During the direct flutter test, the response of all the accelerometers placed throughout the wing during the onset of the LCO was measured, with the results presented in this chapter. All the responses were measured using Single-Axis Accelerometers of the type PCB Piezotronics 352A24. Looking at the responses in Figures B.1 - B.8, it can be seen that the amplitude of the measured local z-acceleration is decreasing with increasing angle of attack.

Looking at the responses, the fact that the response of the accelerometers placed near the wing's leading edge was smaller than the accelerometers placed near the wing's trailing edge can be seen. This effect is most likely caused by the addition of masses close to the leading edge resulting in the elastic axis being closer to the leading edge.

Furthermore, based on the measured response of the different accelerometers, it can be seen that the larger accelerations occur towards single directions within the oscillation. The accelerometer placed near the leading edge shows a higher acceleration towards the positive acceleration direction, and the accelerometers placed near the trailing edge show a larger negative acceleration direction. This effect is most likely caused by the detaching and reattaching of the flow throughout the LCO movement.

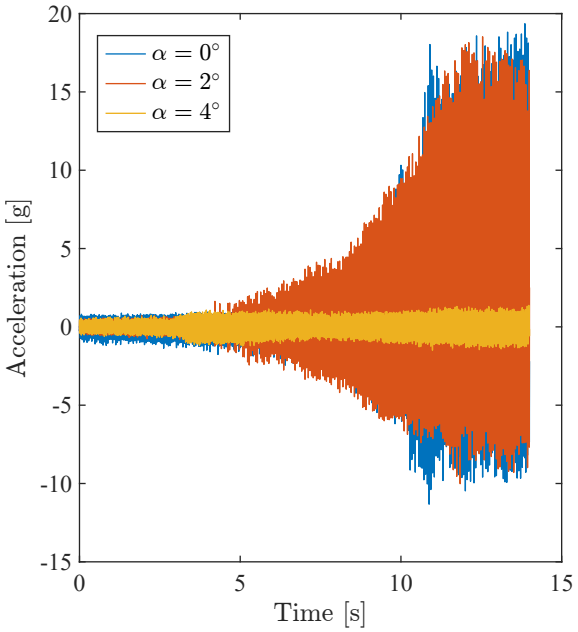

Figure B.1: Local z-acceleration at 0.95 span, 0.3 chord

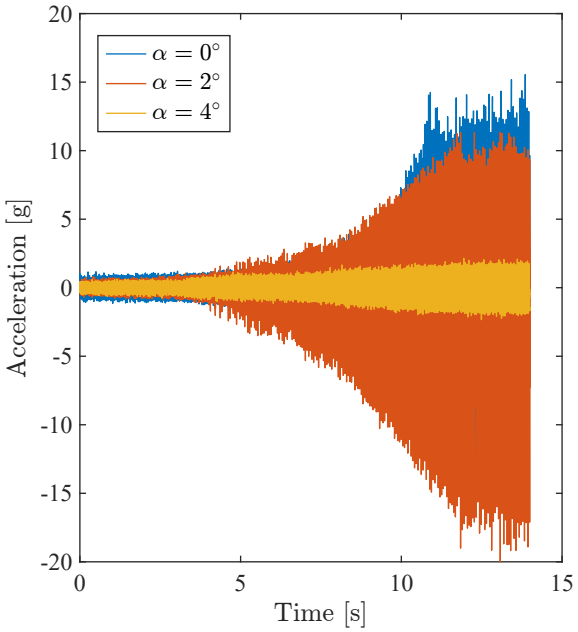

Figure B.2: Local z-acceleration at 0.95 span, 0.7 chord

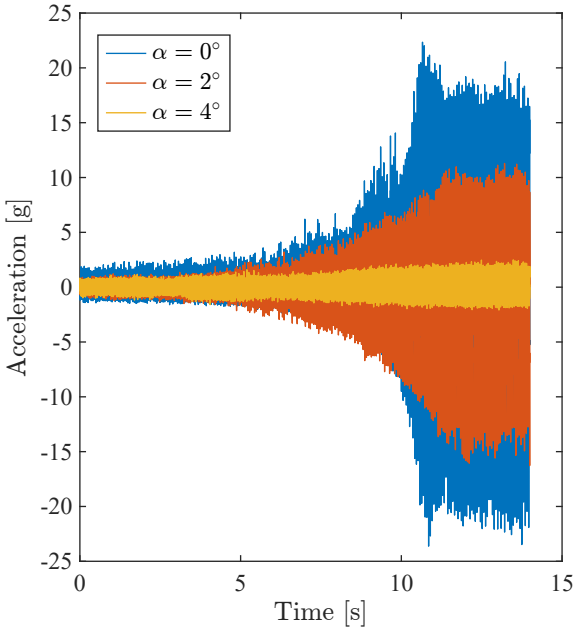

Figure B.3: Local z-acceleration at 2/3 span, 0.3 chord

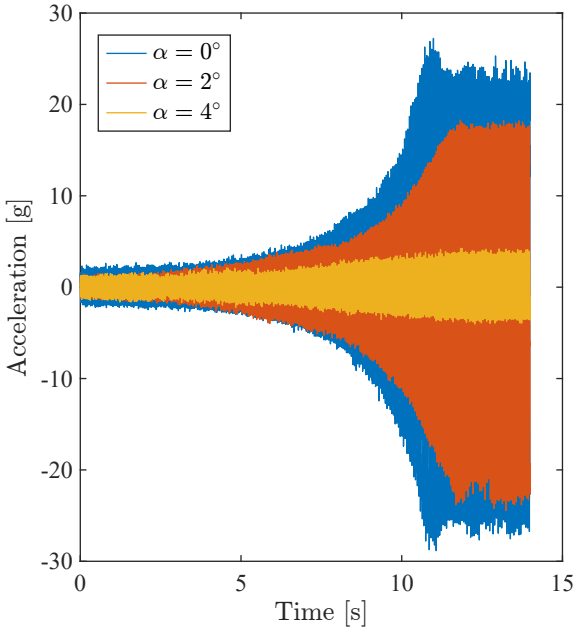

Figure B.4: Local z-acceleration at 2/3 span, 0.7 chord

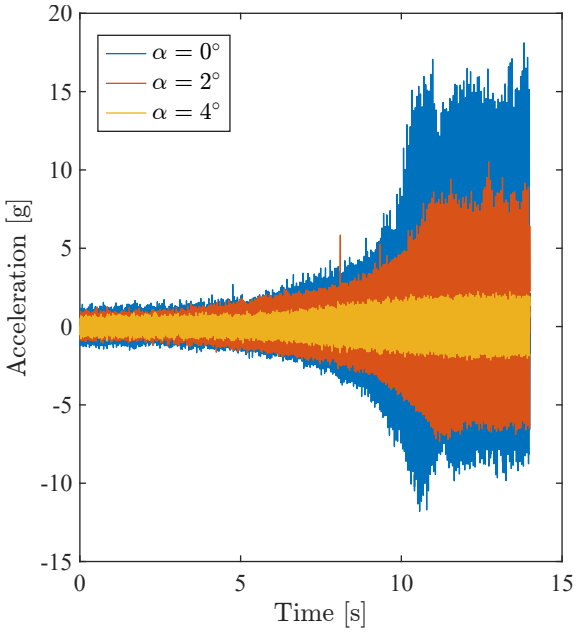

Figure B.5: Local z-acceleration at 1/3 span, 0.3 chord

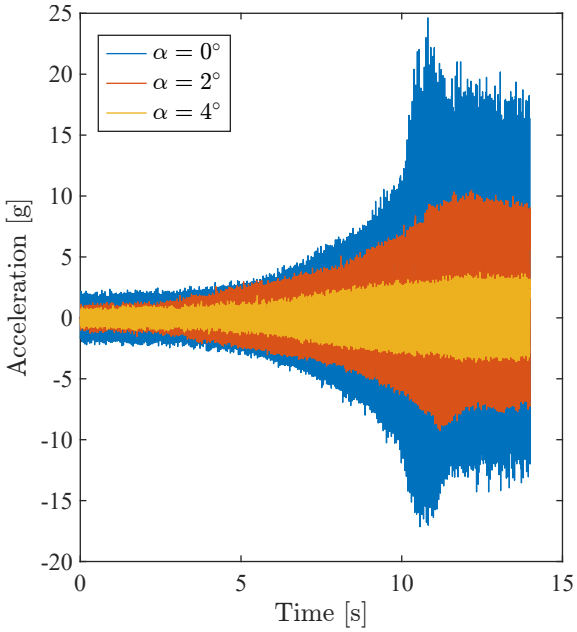

Figure B.6: Local z-acceleration at 1/3 span, 0.7 chord

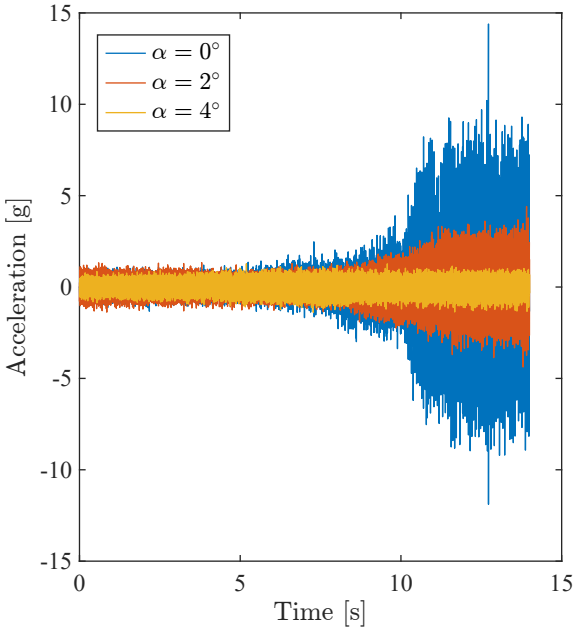

Figure B.7: Local z-acceleration at root LE

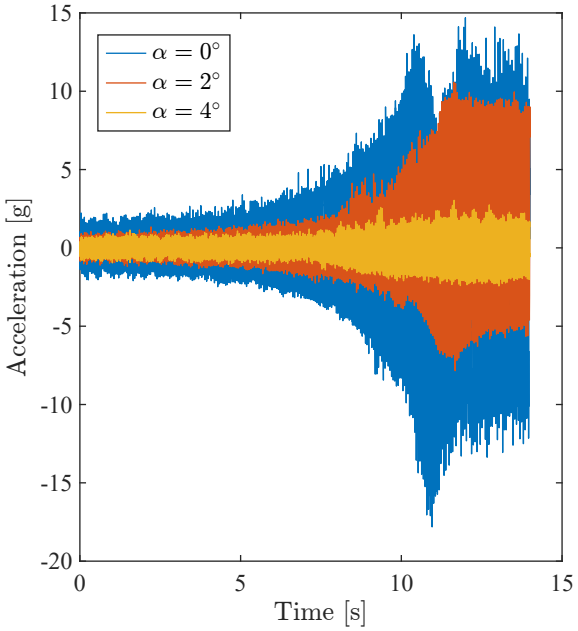

Figure B.8: Local z-acceleration at root TE

Bibliography

[1] European Union Aviation Safety Agency, *Certification Specifications and Acceptable Means of Compliance for Large Aeroplanes (CS-25) Amendment 27*, English, Nov. 2021.

[2] Federal Aviation Administration, *AC 23.629-1B - Means of Compliance with Title 14 CFR, Part 23, § 23.629, Flutter*, English, Sep. 2004.

[3] D. H. Hodges and G. A. Pierce, *Introduction to structural dynamics and aeroelasticity* (Cambridge aerospace series 15), English, 2nd ed. New York: Cambridge University Press, 2011, ISBN: 978-0-511-99711-2.

[4] A. R. Collar, "The Expanding Domain of Aeroelasticity," en, *The Journal of the Royal Aeronautical Society*, vol. 50, no. 428, pp. 613–636, Aug. 1946, ISSN: 0368-3931, 2398-4600. DOI: 10.1017/S0368393100120358.

[5] G. Dimitriadis, *Introduction to nonlinear aeroelasticity* (Aerospace series), English, 1 edition. Chichester, West Sussex, UK: Wiley, 2017, ISBN: 978-1-118-75646-1.

[6] E. H. Dowell, Ed., *A Modern Course in Aeroelasticity* (Solid Mechanics and Its Applications), en. Cham: Springer International Publishing, 2022, vol. 264, ISBN: 978-3-030-74235-5. DOI: 10.1007/978-3-030-74236-2.

[7] E. Dowell, J. Edwards, and T. Strganac, "Nonlinear Aeroelasticity," *Journal of Aircraft*, vol. 40, no. 5, pp. 857–874, Sep. 2003, Publisher: American Institute of Aeronautics and Astronautics. DOI: 10.2514/2.6876.

[8] A. C. L. M. van Rooij, "Aeroelastic Limit-Cycle Oscillations resulting from Aerodynamic Non-Linearities," en, Doctoral, TU Delft, Delft, 2017.

[9] X. Wei and J. E. Mottershead, "Aeroelastic Systems with Softening Nonlinearity," *AIAA Journal*, vol. 52, no. 9, pp. 1915–1927, 2014, Publisher: American Institute of Aeronautics and Astronautics _eprint: https://doi.org/10.2514/1.J052712, ISSN: 0001-1452. DOI: 10.2514/1.J052712.

[10] G. Dimitriadis, "Shooting-Based Complete Bifurcation Prediction for Aeroelastic Systems with Freeplay," *Journal of Aircraft*, vol. 48, no. 6, pp. 1864–1877, Nov. 2011, Publisher: American Institute of Aeronautics and Astronautics. DOI: 10.2514/1.C031139.

[11] D. M. Tang and E. H. Dowell, "Effects of geometric structural nonlinearity on flutter and limit cycle oscillations of high-aspect-ratio wings," en, *Journal of Fluids and Structures*, vol. 19, no. 3, pp. 291–306, Apr. 2004, ISSN: 0889-9746. DOI: 10.1016/j.jfluidstructs.2003.10.007.

[12] M. Patil, D. Hodges, and C. Cesnik, *Characterizing the Effects of Geometrical Nonlinearities on Aeroelastic Behavior of High-Aspect Ratio Wings*. Jan. 1999, Journal Abbreviation: NASA CONFERENCE PUBLICATION Pages: 510 Publication Title: NASA CONFERENCE PUBLICATION.

[13] M. J. Patil, D. H. Hodges, and C. E. S. Cesnik, "Nonlinear Aeroelasticity and Flight Dynamics of High-Altitude Long-Endurance Aircraft," *Journal of Aircraft*, vol. 38, no. 1, pp. 88–94, Jan. 2001, Publisher: American Institute of Aeronautics and Astronautics. DOI: 10.2514/2.2738.

[14] N. H. Zimmerman and J. T. Weissenburger, "Prediction of flutter onset speed based on flight testing at subcritical speeds," *Journal of Aircraft*, vol. 1, no. 4, pp. 190–202, Jul. 1964, Publisher: American Institute of Aeronautics and Astronautics. DOI: 10.2514/3.43581.

[15] G. Dimitriadis and J. E. Cooper, "Flutter Prediction from Flight Flutter Test Data," en, *Journal of Aircraft*, vol. 38, no. 2, pp. 355–367, Mar. 2001, ISSN: 0021-8669, 1533-3868. DOI: 10.2514/2.2770.

[16] J. E. Cooper, P. R. Emmett, J. R. Wright, and M. J. Schofield, "Envelope function - A tool for analyzing flutter data," en, *Journal of Aircraft*, vol. Vol. 30, no. No. 5, pp. 785–790, Sep. 1993. DOI: 10.2514/3.46412.

[17] D. E. Raveh, M. Iovnovich, and T. Nahom, “Wind-Tunnel Study of the ARMA Flutter Prediction Method,” en, in *2018 AIAA/ASCE/AHS/ASC Structures, Structural Dynamics, and Materials Conference*, Kissimmee, Florida: American Institute of Aeronautics and Astronautics, Jan. 2018, ISBN: 978-1-62410-532-6. DOI: 10.2514/6.2018-0702.

[18] J. Sodja, F. Roizner, R. De Breuker, and M. Karpel, “Experimental characterisation of flutter and divergence of 2D wing section with stabilised response,” en, *Aerospace Science and Technology*, vol. 78, pp. 542–552, Jul. 2018, ISSN: 1270-9638. DOI: 10.1016/j.ast.2018.05.014.

[19] F. Roizner and M. Karpel, “Linear and Nonlinear Flutter Analyses Using Dynamic Response Computations,” in *58th AIAA/ASCE/AHS/ASC Structures, Structural Dynamics, and Materials Conference*, ser. AIAA SciTech Forum, American Institute of Aeronautics and Astronautics, Jan. 2017. DOI: 10.2514/6.2017-1594.

[20] F. Roizner and M. Karpel, “Parametric Flutter Margin Method for Aeroservoelastic Stability Analysis,” en, *AIAA Journal*, vol. 56, no. 3, pp. 1011–1022, Mar. 2018, ISSN: 0001-1452, 1533-385X. DOI: 10.2514/1.J056514.

[21] F. Roizner and M. Karpel, “Sensitivity of Aeroservoelastic Stability Characteristics Using Parametric Flutter Margins,” en, *Journal of Aircraft*, vol. 56, no. 4, pp. 1387–1397, Jul. 2019, ISSN: 1533-3868. DOI: 10.2514/1.C035286.

[22] F. Roizner, D. E. Raveh, and M. Karpel, “Safe Flutter Tests Using Parametric Flutter Margins,” en, *Journal of Aircraft*, vol. 56, no. 1, pp. 228–238, Jan. 2019, ISSN: 0021-8669, 1533-3868. DOI: 10.2514/1.C035045.

[23] M. Karpel, M. McCrink, R. Heidersbach, and D. Seth, “Safe wind tunnel flutter test using a shaker and mass margins,” en, in *International Forum on Aeroelasticity and Structural Dynamics*, Madrid, Spain, Jun. 2022.

[24] M. Karpel, “Unified framework for aeroservoelastic response and stability analysis, design and testing,” en, in *International Forum on Aeroelasticity and Structural Dynamics*, Savannah, Georgia, USA, Jun. 2019.

[25] C. Howcroft, D. Calderon, L. Lambert, *et al.*, “Aeroelastic Modelling of Highly Flexible Wings,” in *15th Dynamics Specialists Conference*, ser. AIAA SciTech Forum, American Institute of Aeronautics and Astronautics, Jan. 2016. DOI: 10.2514/6.2016-1798.

[26] C. Mertens, J. Sodja, A. Sciacchitano, and B. van Oudheusden, “Experimental Aeroelastic Characterization of a Very Flexible Wing in Steady and Unsteady Inflow,” en, in *AIAA SCITECH 2022 Forum*, San Diego, CA & Virtual: American Institute of Aeronautics and Astronautics, Jan. 2022, ISBN: 978-1-62410-631-6. DOI: 10.2514/6.2022-1344.

[27] A. Drachinsky, O. Avin, D. E. Raveh, Y. Ben-Shmuel, and M. Tur, “Flutter Tests of the Pazy Wing,” *AIAA Journal*, vol. 60, no. 9, pp. 5414–5421, Sep. 2022, Publisher: American Institute of Aeronautics and Astronautics, ISSN: 0001-1452. DOI: 10.2514/1.J061717.

[28] O. Avin, D. E. Raveh, A. Drachinsky, Y. Ben-Shmuel, and M. Tur, “Experimental Aeroelastic Benchmark of a Very Flexible Wing,” *AIAA Journal*, vol. 60, no. 3, pp. 1745–1768, Mar. 2022, Publisher: American Institute of Aeronautics and Astronautics, ISSN: 0001-1452. DOI: 10.2514/1.J060621.

[29] D. Tang and E. H. Dowell, “Experimental and Theoretical Study on Aeroelastic Response of High-Aspect-Ratio Wings,” en, *AIAA Journal*, vol. 39, no. 8, pp. 1430–1441, Aug. 2001, ISSN: 0001-1452, 1533-385X. DOI: 10.2514/2.1484.

[30] D. Tang and E. H. Dowell, “Limit-Cycle Hysteresis Response for a High-Aspect-Ratio Wing Model,” en, *Journal of Aircraft*, vol. 39, no. 5, pp. 885–888, Sep. 2002, ISSN: 0021-8669, 1533-3868. DOI: 10.2514/2.3009.

[31] J. He and Z.-F. Fu, “1 - Overview of modal analysis,” en, in *Modal Analysis*, J. He and Z.-F. Fu, Eds., Oxford: Butterworth-Heinemann, Jan. 2001, pp. 1–11, ISBN: 978-0-7506-5079-3. DOI: 10.1016/B978-075065079-3/50001-2.

[32] J. He and Z.-F. Fu, Eds., *Modal Analysis*, en. Oxford: Butterworth-Heinemann, Jan. 2001, ISBN: 978-0-7506-5079-3. DOI: 10.1016/B978-075065079-3/50001-2.